A Computational and Experimental Investigation of Film Cooling Effectiveness

by

JIAN-MING ZHOU

B.Sc. (Applied Mechanics), Fudan University, Shanghai, China, 1984

M.Sc., The University of British Columbia, 1990

A THESIS SUBMITTED IN PARTIAL FULFILLMENT OF

THE REQUIREMENTS FOR THE DEGREE OF

DOCTOR OF PHILOSOPHY

in

THE FACULTY OF GRADUATE STUDIES

(Department of Mechanical Engineering)

We accept this thesis as conforming

to the required standard

THE UNIVERSITY OF BRITISH COLUMBIA

September 1994

In presenting this thesis in partial fulfilment of the requirements for an advanced degree at the University of British Columbia, I agree that the Library shall make it freely available for reference and study. I further agree that permission for extensive copying of this thesis for scholarly purposes may be granted by the head of my department or by his or her representatives. It is understood that copying or publication of this thesis for financial gain shall not be allowed without my written permission.

(Signature)

Department of __MECHANICAL ENGINEERING__

The University of British Columbia
Vancouver, Canada

Date ___Sept 2/94___

Abstract

Film cooling is a technique used to protect turbine blades or other surfaces from a high temperature gas stream. This thesis presents an experimental and computational study of film cooling effectiveness based on two film cooling models in which coolant is injected onto a flat plate from a uniform slot (2-D) and a row of discrete holes (3-D). The existing turbulence models and near-wall turbulence treatments are evaluated. The transport equations are solved by the control volume finite difference and multigrid formulation, and the flow and heat transfer near the injection orifices and the film cooled wall are resolved by grid refinement. To verify the numerical model, physical experiments based on the heat-mass transfer analogy were carried out. Film cooling effectiveness and flow fields were measured using a flame ionization detector and hot-wire anemometry.

For the 2-D model, the turbulence is modelled by the multiple-time-scale (M-T-S) turbulence model combined with the low-Re k turbulence model in the viscosity-affected near-wall region. Comparisons of the film cooling effectiveness and flow fields between computations and experiments for mass flow rate (R_M) of $0.2, 0.4, 0.6$ show that the M-T-S model provides better agreement than the k-ε model especially at high R_M. Also, the low-Re k turbulence model used in the near-wall region allows for grid refinement near the film cooled wall, giving better flow and heat transfer predictions downstream of injection than the wall function method.

For the 3-D model, a non-isotropic k-ε turbulence model is used in combination with the low-Re k turbulence model as the near-wall treatment. Comparison of the spanwise averaged film cooling effectiveness between computation and experiment shows good agreement for mass flow ratios of 0.2, 0.4; however, the numerical values are consistently lower than the measured results for $R_M = 0.8$. Comparison of the mean velocity and turbulence kinetic energy shows good agreement, especially near the injection. Further work to extend the M-T-S model to the 3-D model is suggested.

Parametric tests of film cooling by single and double-row injection were carried out computationally to investigate the effects of mass flow rate, injection direction, hole spacing and stagger on the film cooling effectiveness. The superior performance of the lateral injection at high mass flow ratio, mainly near the injection orifice, is demonstrated. For the double-row injection, consistently better performance of the arrangement with stagger factor *A/d=3* is found for the range of parameters investigated.

Table of Contents

List of Tables

List of Figures

Nomenclature

A_μ, A_ε	Near-wall turbulence damping function constants.
A	Stagger factor (see Figure 7.18).
C	Concentration.
C_μ, C_1, C_2	The k-ε turbulence model constants.
$C_{\mu f}, C_{p1}, C_{p2}, C_{p3},$ C_{t1}, C_{t2}, C_{t3}	The M-T-S turbulence model constants.
E	Voltage.
G	Generation rate of turbulent kinetic energy.
P	Mean static pressure.
R_M	Mass flow ratio or blowing rate ($R_M = \dfrac{\rho_j U_j}{\rho_\infty U_\infty}$).
R_S	Relative mass flow ratio ($R_S = \dfrac{R_M}{S/d}$).
R	Injection row spacing (see Figure 7.18).
S	Injection hole spacing (see Figure 7.18).
T	Temperature.
U, V, W	Mean velocity components.
U_τ	Friction velocity ($U_\tau = \sqrt{\dfrac{\tau_w}{\rho}}$).
X, Y, Z	Cartesian coordinates.
d	Injection hole diameter.
h	Film cooling heat transfer coefficient.
k	Turbulent kinetic energy.
k_p, k_t	Turbulent kinetic energy of large eddies and small eddies.
l_μ, l_ε	Length scales for turbulent eddy viscosity and dissipation rate.
p'	Fluctuating pressure.
q	Heat flux per unit time and area.

u', v', w'	Fluctuating velocity components.
x, y, z	Cartesian coordinates.
y^+	Dimensionless distance from the solid wall ($y^+ = \dfrac{yU_\tau}{\nu}$).
α, β	Lateral and streamwise components of injection angle (see Figure 7.18).
δ	Boundary layer thickness.
ε	Dissipation rate of turbulent kinetic energy.
$\varepsilon_p, \varepsilon_t$	Energy transfer rate, dissipation rate of turbulent kinetic energy.
η	Film cooling effectiveness.
κ	von Karman constant ($\kappa=0.41$).
μ	Dynamic viscosity.
μ_t	Turbulent eddy viscosity.
ν	Kinematic viscosity.
ρ	Fluid density.
$\sigma_k, \sigma_\varepsilon$	Turbulence model constants.
σ_t	Turbulent Prandtl number.
τ_w	Wall shear stress.
Φ, ϕ'	Mean and fluctuating values of scalar.

Subscripts

aw	Adiabatic wall.
j	Coolant injection.
t	Turbulent.
∞	main stream

Acknowledgment

I would like to express gratitude to my supervisors, Dr. M. Salcudean and Dr. I.S. Gartshore. Their guidance and encouragement have made this project an enjoyable experience and their financial assistance has allowed me to participate in this project.

I would express my appreciation to professors in the Department of Mechanical Engineering and the Institute of Applied Mathematics, especially to Dr. U. Asher and Dr. P. Hill.

Thanks are due to all members of the CFD group in the Department of Mechanical Engineering for their helpful suggestions and discussions. Thanks to Mr. M. Findlay for his proofreading of this thesis.

Finally, I wish to thank my wife, Lu, for her patience and support.

Chapter 1

Introduction

1.1. Background

For high efficiency operation of gas turbine engines, thermodynamic analysis shows that the temperature of the combustion gas at the inlet to the turbine should be as high as possible. The working temperature has now reached about *1800 K* for modern gas turbine engines. As the temperatures rise, the problem of protecting the surfaces from thermal damage becomes critical since a difference of 15°C in the average blade temperature can mean a factor of two in the blade service life. Reliable operation and prolonged useful life of turbine blades require an effective cooling system to maintain the blade temperature and to keep thermal stresses within allowable limits for the material.

Film cooling, often used in conjunction with internal convection cooling, is a promising thermal protection method available for the outer surface of blades at the first stages of gas turbine stators and rotors. In the film cooling process, the coolant is injected into the boundary layer through rows of holes to generate an insulation film on the blade surface downstream of the holes. There are many configurations of film cooling. For example, near the leading edge of turbine blades, full coverage cooling (or shower-head film cooling) is used to protect the critical leading edge region. Figure 1.1 shows a typical rotor blade cross-section with the cooling air flow.

Film cooling design aims at maximizing the thermal protection for the blades with the smallest amount of coolant injected, resulting in the smallest possible penalty to the engine cycle. The thermal protection by discrete hole film cooling depends crucially on adopting the correct spacing between holes, the right velocity of injection relative to that of the external stream, and the best injection hole orientation. Clearly, other practical

factors such as manufacturing methods, internal cooling, and structural integrity of the blade also play crucial roles. These are beyond the scope of the present work, however.

A large number of experimental studies have been undertaken to provide design data for the effects of various parameters on the film cooling. Current design is mostly empirical and relies heavily on the correlations of overall film cooling effects based upon a large experimental data base. In addition, experimental investigations are usually expensive and time-consuming under realistic conditions. Thus there is an urgent need to reduce the level of empiricism in the design practice and to develop a truly predictive capability for film cooling design.

Increasing efforts have been made to deduce film cooling performance through the computational modelling of transport phenomena in the film cooling process. With the advent of high speed and large capacity computers, numerical simulation has become a promising tool. However, successful application still depends heavily on an understanding of basic transport mechanisms in the film cooling process and the improvement of modelling and solution techniques.

1.2. Posing the Film Cooling Models

Basic film cooling research has been carried out to measure and predict the relationship between the wall temperature distribution and heat transfer for a given geometry and mainstream and secondary flows. Unfortunately, due to the presence of many parameters such as pressure gradient, Reynolds number, inlet geometry, etc., the prediction of the blade surface temperature contains significant uncertainties. This situation makes it necessary to study each parameter independently, with the hope of later establishing their mutual couplings. For simplicity, effects present in operating high temperature engines such as blade curvature, variable fluid properties, and fluid compressibility are left out of the present study.

In the present work, the film cooling process is idealized by considering the flow as steady, and the velocities and temperature variations as sufficiently small so that the fluid properties can be considered as constant. With this assumption, the velocity field is independent of the temperature field. By using the superposition method, the heat transfer between the mainstream and the film cooled wall can be described by the following equation (see Eckert, 1984 for details):

$$q = h(T_{aw} - T_w) \tag{1.1}$$

where q is the heat flux per unit time and area from the mainstream to the film cooled surface, h is the heat transfer coefficient, T_w is the wall temperature, and T_{aw} is the adiabatic wall temperature. T_{aw} and h are two important variables for the prediction of blade surface temperature. The present work studies only the adiabatic wall temperature which can be expressed in a dimensionless form, called the film cooling effectiveness:

$$\eta = \frac{T_{aw} - T_\infty}{T_c - T_\infty} \tag{1.2}$$

where T_∞ is the mainstream temperature and T_c is the coolant temperature. The significance of the film cooling effectiveness is that it can vary considerably and is harder to predict than the heat transfer coefficient.

One important feature of film cooling is the highly complex nature of the flow field created by the coolant jet interacting with a hot cross-stream. Most recent studies of film cooling effectiveness have been done on flat plates with the objective to identify and understand the thermal and aerodynamic behavior of the coolant film. Figure 1.2 shows the typical 2-D and 3-D flat plate film cooling models. These basic models include complex features involved in real turbine blade cooling; therefore, modelling experience based on these models could provide useful information for the prediction of film cooling in real situations.

Figure 1.3 shows the schematics of the typical structures appearing in 2-D and 3-D film cooling flows. In the 2-D film cooling case, both the external flow and the secondary

fluid are uniform across the span. A shear layer separates the injected turbulent jet flow and the free-stream turbulent boundary layer. The injected flow may separate at the rear of the slot and subsequently reattach. Downstream of the slot, the instability due to the shear layer causes the turbulent mixing of the free-stream and the injected film. The film cooling effectiveness is closely related to the enhanced mixing resulting from the coolant jet separation and reattachment, and also related to the interaction between the coolant jet and the free stream boundary layer. The effects of the mass flow rate and injection angle of the coolant on the cooling effectiveness have been widely studied in the 2-D model.

In the 3-D film cooling case, one or several rows of holes are used for the coolant injection instead of a continuous slot. A complicated flow pattern is found after the coolant is injected streamwise into the crossing boundary layer through a discrete hole. Due to the mutual deflection of the jet and cross flow, the mainstream moves upwards and along the sides of the jet. In the wake regions of the jets, the streamwise velocity increases and the conservation of mass requires fluid to move from the sides towards the plane of symmetry. Two vortices are formed in the kidney-shaped cross section of the jet. Very close to the wall a reverse-flow region forms. Cross-stream fluid enters this region and travels upstream where it is lifted by the jet fluid and is then carried downstream. Unlike the flow in 2-D situations, the flow does not recirculate and the reverse flow is restricted to a region very near the wall. The mixing between the external flow and jet flow is enhanced by the vortices along the jet. The discrete hole injection produces a 3-D spanwise, non-uniform flow and cooling effectiveness. A spanwise averaged film cooling effectiveness defined as:

$$\bar{\eta} = \frac{1}{S} \int_{-S/2}^{S/2} \eta \, dz \qquad (1.3)$$

where S denotes the hole spacing, is used to evaluate the film cooling performance. The film cooling performance is affected by factors such as the mass flow rate of the coolant, hole arrangement, and injection angle.

1.3. Objectives and Scope of the Thesis

A research collaboration between Pratt and Whitney Canada and the University of British Columbia has been developed to investigate the film cooling at the leading edge of turbine blades. Experimental investigations have been performed and a numerical tool for modelling the film cooling process has been developed. The numerical tool can be used not only to provide a detailed database but also to improve our understanding of the thermal and aerodynamic mechanisms involved.

Due to the complex flow structures involved, direct application of the existing numerical methods to film cooling prediction has raised two important problems: 1) Film cooling flow involves a wide range of length scales. Nevertheless the resolution of the flow and heat transfer near the regions of injection and film cooled wall surface is crucial for accurate predictions of film cooling effectiveness. To obtain such flow resolution, an efficient numerical method covering a wide range of scales is needed. 2) The adequacy of existing turbulence models for complex film cooling flows is not clear. These difficulties discourage further investigations of the heat transfer coefficient h, and the model with variable fluid properties until there is a clear evaluation of the numerical methods that are used to simulate simpler but related physical phenomena.

The main objective of this work is to develop a numerical modelling method suitable for the prediction of film cooling effectiveness. This objective is approached by four steps. The first is to adapt grid refinement to resolve flow and heat transfer near the wall and injection orifice regions, and to obtain numerical solutions with the efficient multi-grid iteration method. The second is to evaluate the standard k-ε turbulence model and the wall function treatment, and to explore additional turbulence models and near-wall turbulence treatments. The third is to verify the numerical model by conducting physical measurements of film cooling effectiveness and flow fields in wind tunnel experiments.

The fourth and final step is to apply the present numerical tool to study the double row film cooling on a flat plate, and to compare the results obtained with the experimental work of Gartshore et al. (1993). The work described in this thesis can be summarized as follows.

Two film cooling models have been investigated, representing film cooling on a flat plate from vertical injection of coolant firstly through a uniform slot and, secondly from a row of discrete square holes. The models have been simplified so that a Cartesian coordinate system can be used, and numerical errors arising from the analysis of general complex geometries can be avoided. Despite this simplification of the geometries and the assumption that the fluid is incompressible, steady-state, and has constant fluid properties, the numerical models retain the main features of flow and heat transfer which are present in the real situation of complex film cooling. The 2-D model represents the effect of the separation and the reattachment of injectant while the 3-D case represents more complicated effects, such as the formation of the kidney-shaped vortex along the trajectory of injectant as well as the complex detaching and reattaching flow downstream of injection.

The performance of standard high-Re k-ε turbulence models with the wall function has been evaluated for the film cooling geometries described above. In the present work, a low-Re k turbulence model was used in the region very close to the adiabatic wall in order to resolve the flow and heat transfer near the wall. The multiple-time-scale turbulence model was used in the 2-D computations to improve the prediction at high mass flow ratios. In the 3-D computations, a non-isotropic k-ε model was used to account for the anisotropy of turbulence near the wall.

The transport equations were solved on refined grids by using the multi-grid method with efficient reduction of the numerical errors. The increased accuracy of the computations makes it possible to evaluate the turbulence models.

Since there is no directly comparable experimental data in the literature for these simplified models, physical experiments were carried out to provide detailed flow field and cooling effectiveness for verification of the numerical model. Film cooling effectiveness measurements were made using a flame ionization detector, based on the heat-mass transfer analogy, and the mean flow and turbulence were measured using hot-wire anemometry. Comparisons between experiment and computation are presented in this thesis.

The numerical model was applied in parametric studies to show the effects of hole spacing, hole stagger, and coolant mass flow rate on the film cooling performance in single and double-row film cooling. The parameter values are the same as those used in the experimental work of Gartshore et al. (1993). The structure of vortices behind coolant injection locations and its effects on the film cooling performance were investigated numerically.

The main contributions of the present study can be summarized as follows.

- The present experimental measurements of film cooling effectiveness, mean flow and turbulence in the wind tunnel provide a systematic database for verification of turbulence models.

- The present numerical work applies and evaluates the low-Re k model and the use of a fine grid as a near-wall turbulence treatment to resolve the heat transfer in the region close to the film-cooled wall surface. It also applies the multiple-time-scale turbulence model to allow for non-equilibrium turbulence in the film cooling.

- The present work provides increased accuracy in the assessment of turbulence models by using the multi-grid method and grid refinement in the computations reducing discretization errors and improving iterative convergence.

- The parametric tests provides some insight into vortex formation downstream of the coolant injection and the consequent effect on the cooling performance.
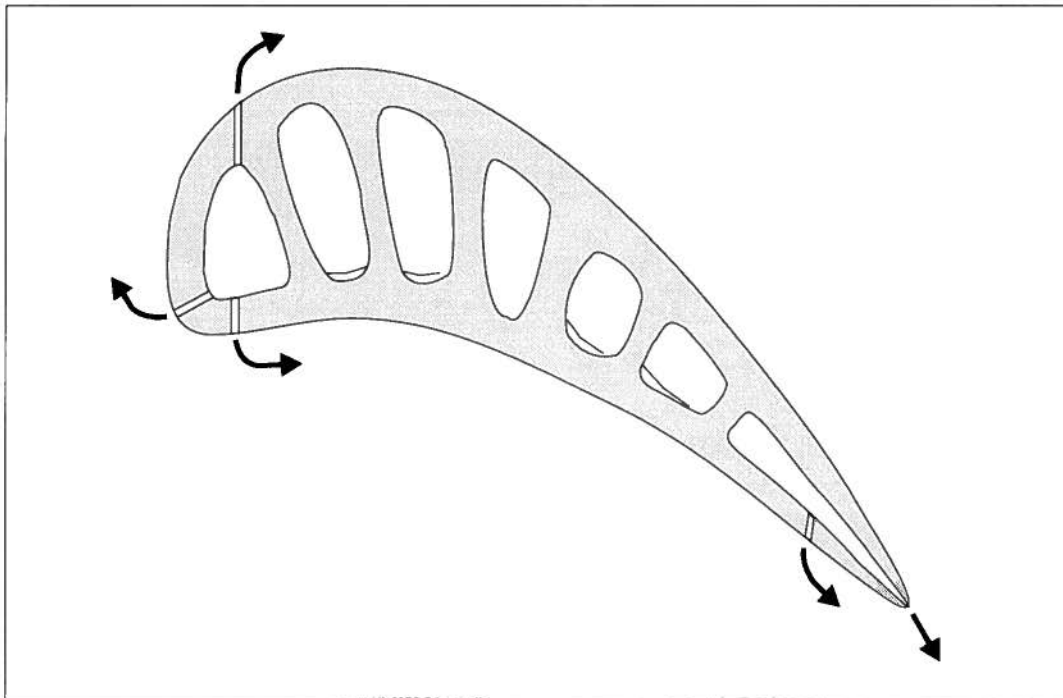
Figure 1.1: A typical turbine rotor blade cross section with cooling flow.
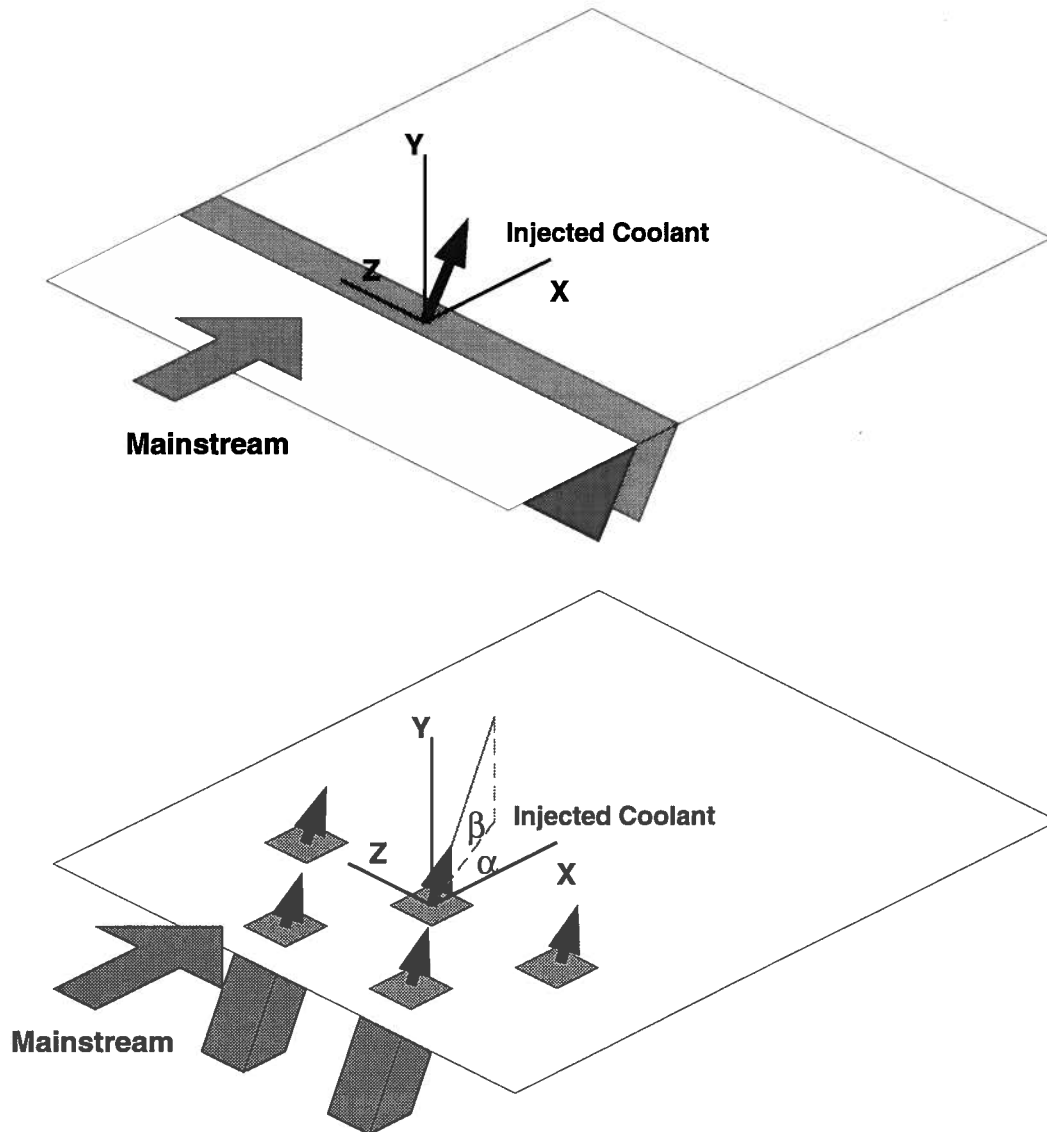
Figure 1.2: Flat plate film cooling models.
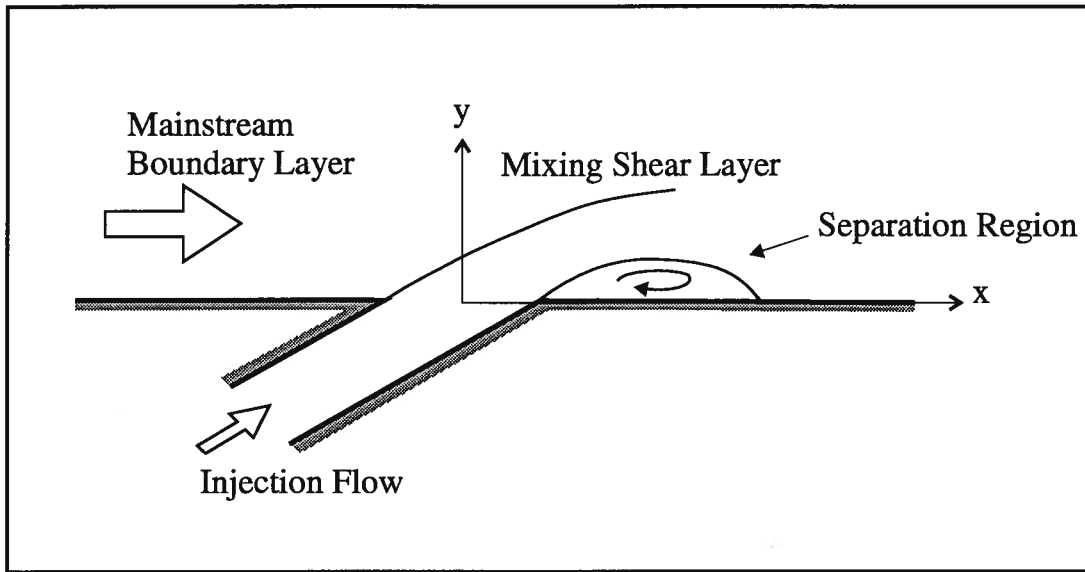
(a) 2D film cooling flow
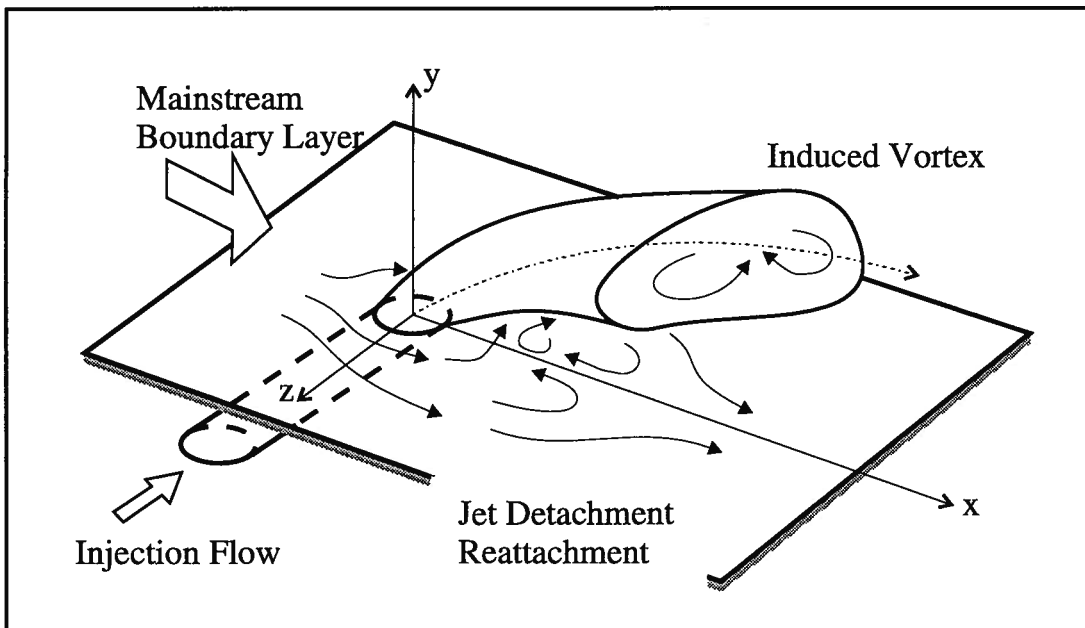
(b) 3D film cooling flow

Figure 1.3: Schematics of 2-D and 3-D film cooling flows.

Chapter 2
Literature Survey

Film cooling has been a subject of research for over forty years. The large body of film cooling papers in the open literature is divided here into broad categories of experiment and computation. General reviews have been undertaken by Goldstein (1971) for early work and Moffat (1986) for more recent developments. Experimental works include studies which generate data on adiabatic film cooling effectiveness and provide measurements of flow and heat transfer. Computational works consist of studies of the numerical solution techniques and turbulence modelling methods. In this chapter, previous experimental and computational papers are reviewed. Since there have been a large number of computational papers in the areas of turbulent heat transfer other than film cooling, review of those works are made at the same time. Finally, some remarks are addressed to the motivation of the present work.

2.1. Experimental Studies

There are many papers in the open literature reporting film cooling effectiveness measurement data for design use, especially for slot, transpiration, and single hole injection configurations. Recent work has been done on single- and double-row hole injection on either flat plate or curved leading edge surfaces. Most of the early discrete-jet experiments were conducted with the coolant jet-to-crossflow density ratio close to unity. Experiments were performed using either a thermal approach or the heat-mass transfer analogy. The measurements of cooling effectiveness and coolant distribution were mainly made using thermocouples, visualization on thermal-sensitive material, and foreign-gas detectors. The flow fields were measured using hot-wire anemometry or laser Doppler

velocimetry. A brief review of the most significant papers related to the present work is provided in the following discussion.

Goldstein et al. (1970), and Goldstein and Eckert (1974) investigated the angled injection of air through discrete holes into a turbulent boundary layer of air on a flat plate to determine the effect on the film cooling effectiveness. In their experiments, the injected air had a higher temperature ($\approx 25^\circ$C) than the mainstream, and the effectiveness was measured using the non-dimensional adiabatic wall temperature measured by wall thermocouples. They observed that the film cooling effectiveness downstream of the holes increases as the boundary layer thickness just upstream of the injection location is decreased. Comparison between secondary air injected by a single hole and a row of holes showed that data from single hole tests are similar to a row of holes for low blowing rates, but significant differences are observed at higher blowing rates. Also, they found that lateral injection spreads the protection of the cooling film over a wider area than when injection is normal to the flow or inclined downstream only. The interaction of the coolant jet with the mainstream was found to affect the development of cooling effectiveness. At surface locations near the injection holes, as mass flow ratio is increased, effectiveness first rises and then reaches a sustained maximum value. Further downstream, the effectiveness levels are generally lower but rise continuously as mass flow ratio increases.

Bergeles et al. (1976) studied experimentally the near-field character of a circular jet discharged normally to a main stream. In their work, the film cooling effectiveness was measured by adding a tracer of helium (one percent by volume) to the secondary stream. The concentration of helium on the surface of the test plate was obtained by withdrawing samples of air/helium mixture through static pressure taps and measuring the helium concentration with an on-line kathometer. For mass flow ratios between 0.046 and 0.5, a clearly identifiable reverse flow region was detected on the downstream side of the hole using flow visualization. The velocity distribution in the jet at discharge was found to be greatly affected by the presence of the external stream. Measurements of the local cooling

effectiveness showed the peak values of effectiveness immediately downstream of discharge occur off the centerline, which is consistent with the jet assuming a kidney shape as it is bent over by the external stream.

Foster and Lampard (1980) conducted detailed studies of effectiveness and flow downstream of a row of 15 holes on a flat plate. A heat-mass transfer analogy experiment was carried out in which the injected gas was a mixture of Freon and compressed air, and the effectiveness was measured by katharometer. They studied the effect of the streamwise injection angle on film cooling and showed that a small injection angle provides the best cooling effectiveness at low blowing rates while large injection angles are best at high blowing rates. At high blowing rates, the cross-streamwise distribution of the effectiveness downstream of injection is more uniform for 90° injection than 35° injection. It was also observed that an increase in the upstream boundary layer thickness produces a reduction in the effectiveness due to increased lateral mixing in the near-wall region. The use of a small spacing-to-diameter ratio gives improved lateral coverage at all blowing rates, and alleviates jet lift-off effects at high blowing rates.

Jubran and Brown (1985) measured the cooling effectiveness from two rows of holes inclined in the streamwise and spanwise directions. In their experiment, cold air was injected into the hot main stream and the adiabatic wall temperature was measured using thermocouples. Cholesteric liquid crystals were applied to the working surface for temperature-flow visualization as a backup to the thermocouple temperature measurements. They found that an increase in the distance between two rows of holes reduced both local and lateral averaged cooling effectiveness downstream of the second row of holes, especially in the region close to the second row of holes at higher mass flow ratios. The influence of free-stream turbulence intensity and velocity gradients on film cooling performance showed that the averaged effectiveness downstream of the second row of holes is reduced by increased turbulence intensity for all streamwise positions at

low blowing rates. The improved cooling of two rows of holes over one row was also shown in their study.

Honami et al. (1991) carried out an experimental study of film cooling using lateral injection. In their heat transfer experiment, the surface temperature was visualized by covering the test surface with a thin sheet of encapsulated temperature-sensitive liquid crystal. An image processing system based on the temperature and hue of the liquid crystal was used. A double-wire probe (with a constant temperature hot-wire anemometer and a constant current thermal resistance meter) was used for simultaneous velocity/temperature correlation field measurements. From their experiments on three types of hole arrangements: lateral, streamwise and inlined injection, and on three mass flow ratios: *0.5, 0.85,* and *1.2*, the highest spanwise-averaged film cooling effectiveness was observed for lateral injection for the same coolant flow per unit span. The lateral injection produced asymmetric structures with a large scale vortex motion promoted by the primary stream on one side of the jet, but suppressed on the other side. It was also found that this asymmetry increases as the mass flux ratio increased, resulting in low film cooling effectiveness.

Recently, Ligrani et al. (1992) presented a detailed systematic study on the development and structure of flow downstream of either one row or two staggered rows of film cooling holes with compound angle orientations. The effectiveness was measured by thermocouples and upstream boundary layer properties were measured using a five-hole pressure probe with a conical tip. They found that the spanwise-averaged values of effectiveness measured downstream (as far as 20 hole-diameters) of two staggered rows of holes were highest with a blowing ratio of 0.5, and decreased as the blowing ratio increased above 0.5 because of injection lift-off effects. However, as the boundary layer convected farther downstream, the effectiveness increased with blowing ratio. It was also found that with one row of holes the local effectiveness variations are spanwise periodic,

where higher values corresponded to locations where injectant is plentiful near the test surface.

Mehendale and Han (1992) studied the effects of injection hole geometry on the leading edge effectiveness and heat transfer under high mainstream turbulence conditions. It was found that, due to an increase in mainstream turbulence, the effect of secondary flow turbulence is considerably reduced. The effectiveness was found to decrease with increasing mainstream turbulence; however, this effect reduces with increasing blowing rate. In addition, it was found that larger spanwise distances for the case of spacing-to-diameter ratio of 4 cause larger spanwise variation as compared to the smaller spacing-to-diameter ratio of 3. The best effectiveness for the case of mass flow ratio $R_M = 0.8$ was found with spacing-to-diameter ratio of 4 while the best effectiveness for the case of $R_M = 0.4$ was found with spacing-to-diameter ratio of 3.

Recently, a systematic experimental investigation of film cooling effectiveness near the leading edge of a turbine blade has been carried out in the Department of Mechanical Engineering at the University of British Columbia. The measurements of film cooling effectiveness was made using a flame ionization technique based on the heat-mass transfer analogy. The turbine blade model has a semi-cylindrical leading edge bonded to a flat after-body. Both air and CO_2 were used as the secondary flow. The secondary flow was injected in the boundary layer through 4 rows of holes located at $\pm 15^o$ and $\pm 44^o$ about the stagnation line of the leading edge. These holes of diameter d had a 30° spanwise inclination and a *4d* spanwise spacing. Adjacent rows of holes were staggered by *2d*. A paper by Salcudean et al. (1994a) showed that the strong pressure gradient near the leading edge produces a strong non-uniform flow division between the first and the second row of holes at low overall mass flow ratios. Best effectiveness were obtained in a very narrow range of mass flux ratios near 0.4. The effectiveness values deteriorates abruptly with decreasing mass flow ratios, and substantially with increasing mass flow ratios. In the study of the effects of coolant density, it was found that air appears better close to the

first row of holes and CO_2 better at some distance downstream of both rows (Gartshore et al., 1993). Double row cooling with air as coolant showed that the relative stagger of the two rows is an important parameter (Salcudean et al., 1994b). Holes in line with each other in successive rows can provide improvements in spanwise-averaged film cooling effectiveness of as much as 100% over the common staggered arrangement.

2.2. Computational Studies

2.2.1. Numerical Solution Techniques

For many years, researchers have been using parabolic-type solution procedures for the prediction of heat, mass, and momentum transfer in film cooling. The parabolic-type procedure cannot be used for the simulation of recirculating flow in a plane parallel to the direction of the free stream, but it can be used to simulate vertical flows in the cross-stream plane.

Bergeles et al. (1976b) used a partially parabolic numerical scheme to predict the mean velocity and temperature for laminar flow for a single row of inclined holes and for a surface with multiple row of holes in a staggered array. Their calculation showed that the strong acceleration reduced the lateral rate of spreading. A counter rotating vortex pair is created downstream from the hole which shifts the minimum effectiveness away from the mid-plane between holes.

Bergeles et al. (1981) used a semi-elliptic procedure and a nonisotropic k-ε turbulence model for the prediction of film cooling from two rows of holes. Comparison with measurements obtained for an injection angle of 30° and mass flow ratios in the range of 0.2 to 0.5 showed good agreement in the majority of cases. Discrepancies were observed, however, with small boundary layer thicknesses or large injection rates. In their paper, they indicated that the cause of the discrepancies was the local equilibrium

assumption in the turbulence modelling and the inability of the semi-elliptic procedure to properly simulate the zone of flow recirculation downstream of the hole.

Demuren et al. (1986) used a locally-elliptic calculation to investigate the influence of different parameters on the cooling effectiveness. The predicted temperature fields agreed fairly well with available measurements. The film cooling effectiveness was not always in good quantitative agreement with the data. The agreement was satisfactory for the mass flow ratios up to 1 for small spacings. For high blowing rates and larger spacings, only the general trends of the measurements were predicted with the calculated cooling effectiveness lower than observed. It was suggested in their work that a more refined treatment of the region near injection would be necessary to represent the complex flow there.

With the aid of a locally-elliptic calculation, Schonung and Rodi (1987) developed a two-dimensional boundary-layer method for film cooling through discrete-hole injection. Due to the high computational cost of conventional elliptic methods, the elliptic reverse-flow region in the vicinity of the injection holes and the 3-D effects were taken into account by two added 'injection' and 'dispersion' models. Haas et al. (1991) extended this boundary-layer method to study the influence of density difference between hot mainstream and cool secondary gas from a row of holes.

By using a laterally periodic 3-D parabolic procedure, Sathyamurthy and Patankar (1990) investigated the effect on the film cooling effectiveness of variations in the lateral angle of injection, the spacing between the holes, and the blowing rates. The computed results were found to be in good agreement with the previous experimental measurements. From their study, it was found that lateral injection can operate at high blowing rates and can achieve better film coverage than streamwise injection. Increased blowing rates and reduced spacing between the injection holes increase the film cooling effectiveness when the jets are injected across the mainstream. It should be noted that due to the limitation of

their parabolic procedure, their computations could not properly represent the film cooling near the injection.

White (1981) solved the fully elliptic transport equations of a single jet injection into a cross-flow mainstream. The distortion of the flow within the injection hole was found to have a significant effect on the predicted flow field. The separation and reattachment of the non-uniform slot flow suggest that the prediction of cooling effectiveness is restricted to injection at low blowing rates unless a fully elliptic solver is used.

Several elliptic-type Navier-Stokes solvers have been developed in the past years. The "Semi-Implicit Method for Pressure-Linked Equations" (SIMPLE) algorithm (Patankar, 1980) and its revised versions have been widely used for numerical simulation of incompressible flows. The SIMPLE-type procedures employ a segregated solution approach in which the variables are solved separately. Based on a strategy different from the sequential update philosophy of SIMPLE, Vanka (1986) developed a block-implicit solution algorithm, in which the pressures and velocities are updated simultaneously but without the pressure correction equations. In Vanka's algorithm, the continuity equation is retained in its primitive form in terms of velocities and the discretized momentum and continuity equations are treated as one large set of non-linear algebraic equations to be solved. Rapid convergence was reported with a modest requirement for computer storage and time per iteration for the calculation of laminar square cavity flows, sudden expansion flows, and turbulent flows involving sudden, axisymmetric expansion geometries.

Recently, many commercial Computational Fluid Dynamics codes have been developed based on elliptic-type Navier-Stokes solvers. Jubran (1989) used the PHOENICS package to predict the film cooling effectiveness and the velocity field from two rows of holes inclined in the streamwise and spanwise directions. With the k-ε turbulence model, they reported successful predictions of cooling effectiveness at the centerlines of holes for low blowing rates. They also found that the elliptic procedure showed no significant

improvement over the semi-elliptic procedures and concluded that the main problem in poor predictions, especially at high blowing rates, is the inadequacies of turbulence models. Later, Amer et al. (1992) also used the PHOENICS package for an investigation of the performance of k-ε and k-ω models in a prediction of film cooling from two rows of holes (see Section 2.2.2).

Leylek and Zerkle (1993) carried out a large scale numerical analysis of discrete-jet film cooling with a fully-coupled and elliptic computation of flow in plenum, film hole, and cross-stream regions by using the PHOENICS system of codes. The standard k-ε model was employed with the generalized wall function treatment. Their computations were carried out for a single row of jets with film-hole length-to-diameter ratios of 1.75 and 3.5, blowing ratios from 0.2 up to 2, coolant-to-cross-flow density ratio of 2, streamwise injection angle of 35°, and pitch-to-diameter ratio of 3. Because of the use of the wall function, the nodes adjacent to the adiabatic wall surfaces were located at $y^+ = 50$. The computed flow within the film-hole showed that the strength of counter-rotating vortices and local jetting effects were controlled mainly by the film-hole length-to-diameter ratio, the blowing ratio, and the streamwise injection angle. Comparison with experimental data on film cooling effectiveness showed that the computation predicted the correct trends for overall streamwise variation of effectiveness but that the predicted values were consistently higher at the blowing ratio of 0.5, and much improved for the blowing ratio of 1.0. Comparison of the lateral variation of effectiveness showed that the lateral rate of spreading of film from the jets was lower in the computation than in the measured data and that the prediction missed the jet detachment-reattachment behavior.

Early work has indicated that in solving the transport equations, the numerical false diffusion error, which results mainly from the upwinding difference scheme for the convective terms, needs to be reduced. Demuren (1985) presented detailed computations of the steady flow of a row of turbulent jets issuing normally into a nearly uniform cross flow. His use of a three-dimensional QUICK scheme, which employs a higher-order

accuracy difference approximation, produced better results than the more widely employed hybrid (central/upwind) scheme.

Since false diffusion is proportional to the magnitudes of the velocity vector, the grid mesh sizes, and the angles between the velocity vector and any of the grid lines (Patankar, 1980), grid refinement is one of the techniques which can reduce the error and thus improve the accuracy of the numerical approximations. However, as the number of discrete variables and algebraic discretized equations increases, traditional iterative processes encounter a deterioration of convergence.

As a faster iterative technique, the multi-grid method has demonstrated its potential in the field of computational fluid dynamics. The multi-grid method efficiently eliminates most of the work related to the repetition of iterations and rapidly solves the algebraic system of equations with a convergence rate insensitive to the number of grid points. As a pioneer in this area, Brandt (1977) introduced a multi-level adaptive technique with a nonlinear Fast Approximation Scheme (FAS) and subsequently developed the Distributive Gauss-Seidel relaxation method as a smoother for solving the Navier-Stokes equations on a staggered grid (Brandt, 1980). Vanka (1986) used the multi-grid method for his Symmetrical Coupled Gauss-Seidel relaxation method for primitive variable solutions. The TEACH code, which was based on the SIMPLE algorithm, was modified to include the multi-grid formulation by Zhou (1990) for film cooling computations. Recently, a multi-grid segmentation numerical code for 3-D turbulent flow was developed at the University of British Columbia (Nowak, 1991), which permits the entire computational domain to be broken into several segments with different grid sizes and uses the multi-grid method to enhance the iterative convergence of computations over all segments in the domain.

A calculation of 3-D turbulent jets in crossflow was done by Demuren (1990) using a multigrid method. His computations obtained fairly rapid convergence using the k-ε turbulence model, but computations with a full Reynolds stress turbulence model were

not very efficient. His tests of grid independence showed that there were slight differences between results obtained on the two finest grid levels.

2.2.2. Turbulence Modelling

For the successful computation of film cooling, turbulence modelling problems have to be addressed. Recent studies have shown that the selection of the turbulence model is one of the serious problems affecting film cooling computations.

In previous studies, various k-ε models were most commonly used to describe the effects of turbulence for the prediction of film cooling. The k-ε turbulence models make use of both the eddy-viscosity concept introduced by Boussinesq (1877) and the Kolmogorov-Prandtl expression. The k-ε model of Jones and Launder (1972) has been particularly popular and has been applied successfully to a wide variety of 2-D flows that include wall boundary flows, recirculating flows, confined flows, shear flows, and jet flows (Launder and Spalding, 1974). In addition to the k-ε model there are other two-equation models which have been used to model turbulence. One such alternative is the k-ω model, where ω is another choice of the second dependent variable complementing the equation for k and is referred to as the rate of dissipation per unit turbulence kinetic energy ($\omega = k/\varepsilon$). Although various two-equation models are sometimes believed to differ merely in mathematical form and not in content (Launder and Spalding, 1974), different results may be obtained from different models due to the fact that the boundary condition for ε on a solid wall may not be identical to that for ω.

Amer et al. (1992) evaluated two two-equation turbulence models, namely the k-ε and k-ω models for the prediction of film cooling effectiveness from two rows of holes inclined in the streamwise direction. The comparison between the predicted results and previous experimental results indicates that the ability of the turbulence models to predict the experimental results depends heavily on the blowing rate as well as on the downstream distance from the injection holes. For some cases the k-ε model performs better than the

k-ω model and vice versa for other cases; however, it was concluded that the two-equation turbulence models do not work well for film cooling, especially in the vicinity of the holes and at high blowing rates. It should be noted that their computation used a coarse grid arrangement near the jet orifice and wall, so that their solution may depend heavily on the grid used.

The failure of the two-equation models with wall function treatment for film cooling can be attributed to: 1) increased turbulence generation at high mass flow ratios due to the fact that the flow near the holes is disturbed and unsteady, and cannot be represented by the equilibrium turbulence assumption in the model, 2) film jet spreading can not be represented by isotropic eddy-viscosity, 3) flow and heat transfer in the near-wall viscosity-affected sublayer need to be resolved.

For complex 3-D flows, the k-ε models may have to be replaced with higher-order turbulence models. The transport equations for the turbulence stresses $\overline{u_i'u_j'}$ and the turbulence scalar flux $\overline{u_i'\theta'}$ can be obtained by applying the Reynolds decomposition. The modelled Reynolds stress equations are, however, extremely difficult to solve for a 3-D flow. Several attempts have been made to simplify the Reynolds stress transport equations. The simplification of these transport equations results in the algebraic stress models which model $\overline{u_i'u_j'}$ and $\overline{u_i'\theta'}$ by algebraic transport equations at each point in the flow (Launder, 1988). The algebraic stress models have considerable appeal but there is still less experience with them than with the k-ε models (Ferziger,1987).

Bergeles et al. (1978) refined the k-ε model by introducing the algebraic stress model. For the computation of discrete hole film cooling the proposed model accounts for the anisotropic nature of the eddy viscosity and diffusivity. This formulation has been widely used in recent film cooling computations by Demuren et al. (1986) and Jubran (1989). However, their work indicated the need to allow for the nonequilibrium of turbulence in order to obtain satisfactory predictions of film cooling effectiveness at high blowing rates, especially in the region close to the injection.

Kim and Chen (1989) developed a multiple-time-scale (M-T-S) turbulence model to simulate non-equilibrium turbulence. The M-T-S model partitions the turbulent kinetic energy spectrum into the turbulent kinetic energy of large eddies and that of the fine-scale eddies instead of using a single time scale to describe both the turbulent transport and dissipation of the turbulent kinetic energy. In the M-T-S model the turbulent transport of mass and momentum is described using the time scale of the large eddies and the dissipation rate is described using the time scale of the small eddies. Therefore, the M-T-S model is more able to resolve non-equilibrium turbulence by considering the generation, cascade, and dissipation of the turbulent kinetic energy. The M-T-S model has been successfully applied to several complex flow situations, such as divergent channel flows, wall jet, and backward-facing step flow (Kim and Chen, 1989; and Kim, 1991). Recently, Kim and Benson (1993) have applied the M-T-S model to the flow of a row of jets in a confined crossflow and reported the inability of the k-ε model to predict the horseshoe vortex located along the circumference of the jet exit.

For flow close to a solid wall, a high-Re number turbulence model is no longer valid. A treatment is needed which takes into account the influence of the wall upon the development of near-wall turbulence. As the most popular approach, wall functions are used to account in an overall fashion for the effective convection, diffusion, sources, and sinks of the flow in the region between the near-wall node and the wall (Launder and Spalding, 1974). In more complex flows, however, difficulties are often encountered because fine grids are necessary to accurately compute near-wall flow characteristics such as the reattachment length following a flow separation.

An alternative is to solve the flow equations elliptically through a fine grid to the wall. Low-Re k-ε models for different flows have been studied by some researchers (Jones and Launder, 1972; and Nagano and Tagawa, 1990). One disadvantage of this approach is that many grid points (usually more than 30) are required within the viscous sublayer. For economy of nodal points, a two-layer approach was used in the recent work

done by Yap (1987) and Rodi (1991). In the two-layer approach, the flow far away from the wall is simulated with a high-Re turbulence model, such as the k-ε model, while the viscosity-affected near-wall region is resolved with a simpler low-Re k equation model employing a prescribed length-scale distribution. This near-wall treatment has found a wide range of applications in 2-D flow situations and the results have been encouraging. However, very few simulations have been done in 3-D flow situations.

2.3. Remarks Arising from Work Reviewed

A large experimental database of film cooling effectiveness measured by direct thermal methods and heat-mass transfer analogy methods is available in the open literature. So far, however, no detailed flow measurements, including upstream boundary layer thickness and turbulence level, have been reported together with the measurement of effectiveness. Most computational works have been compared with published effectiveness values using an assumed mainstream boundary layer. Therefore, the comparison between computational and experimental results is not reliable since it is known that the mainstream boundary layer thickness and turbulence level affect the mixing of the coolant jet with the mainstream and thus the effectiveness. Furthermore, detailed flow information downstream of the coolant injection and particularly close to the coolant holes is important for the verification of turbulence models. Therefore, extensive systematic measurements of the flow and heat transfer have to be made to achieve satisfactory flow and heat transfer code validations.

In real film cooling situations, the coolant is usually injected through circular holes. This geometry requires the numerical model to use a curvilinear body-fitted coordinate system rather than a Cartesian coordinate system. Although there are such commercial Computational Fluid Dynamics codes available, their accuracy and efficiency generally cannot provide good flow resolution near the wall. In an effort to reduce the numerical

errors involved, the Cartesian model is used in the present work, meeting our objective to evaluate various turbulence models.

In previous film cooling computations, the evaluations of the turbulence models are often based on rather coarse computational grids. In order to separate the numerical errors from the deficiencies of the turbulence model, it is important to ensure that computations reach grid independence and that numerical errors (e.g., the false diffusion) resulting from the discretization are properly evaluated. For film cooling, an elliptic Navier-Stokes solver which has the capability of handling local grid refinement near the wall and near the injection orifice region appears necessary, since the flow field has very nonuniform length scales. Convergence for a large number of computational grid nodes can be accelerated by applying the multi-grid method.

The failure of numerical computation for high mass flow ratios of coolant injection has been shown during the present study (Zhou et al., 1993a and 1993b). This failure is partly due to the fact that at high mass flow ratios, turbulence is neither in equilibrium nor is it isotropic. The algebraic Reynolds stress models may be required in 3-D flows. However, even the algebraic forms of these equations are not efficient and are not always numerically stable. Therefore, a simplified form of the algebraic Reynolds stress model which represents the non-isotropic turbulence is appropriate at this stage of computation.

Although successful predictions using two-equation models other than the k-ε model have been reported (e.g., the k-ω model of Wilcox, 1993), these models are all based on the equilibrium eddy-viscosity concept. In order to take some account of the non-equilibrium turbulence in film cooling flow, the multiple-time-scale turbulence model can be introduced into film cooling computations. However, the applicability of the multiple-time-scale turbulence model needs to be evaluated.

Grid refinement near the solid wall requires an adequate near-wall turbulence treatment in order to resolve the large gradients of velocity and temperature in the viscosity-affected sublayer. Most reports of film cooling computation use wall functions

as the near-wall treatment for turbulent flow and heat transfer. Two-layer modelling approaches that use the k-ε model and low-Re k model have been successfully applied to boundary layers and separated and attached flows. The two-layer near-wall treatment is not computationally expensive and does not cause severe iteration convergence problems. This treatment has not been used in previous film cooling computations. Its applicability to 3-D film cooling flow needs to be assessed.

In view of this survey of published literature on film cooling research, the objectives of the present work can be summarized as follows:

- Carry out measurements of film cooling effectiveness, mean flow, and turbulence in the wind tunnel to provide new experimental data for the validation of the present numerical predictions.

- Solve the governing equations using the multi-grid method on a refined grid to achieve an accurate prediction of film cooling effectiveness. The grid refinement is able to reduce the false diffusion and to resolve important flow structures.

- Use the low-Re k model and fine grid as a near-wall turbulence treatment in order to resolve the flow and heat transfer in the viscosity-affected region close to the film-cooled wall surface and thus to improve the prediction of film cooling effectiveness.

- Apply the multiple-time-scale turbulence model to the film cooling computation in order to allow for non-equilibrium turbulence.

- Study the formation of the vortices formed downstream of injection and their effect on the cooling performance using a highly refined mesh near the cooling orifices and the surface. The present flat plate tests can provide some insight into film cooling in real situations.

Chapter 3
Experimental Investigation

In this chapter, measurements of the film cooling effectiveness, mean flow, and turbulence are described for 2-D and 3-D film cooling studies. The physical experiments use the heat-mass transfer analogy which replaces the actual heat transfer process. The wind tunnel and injection system for the experiments, the measurement techniques, and the related calibration procedures are presented. The condition of the turbulent boundary layer and injection flow are investigated. The results of flow field and effectiveness measurements are presented in Chapters 6 and 7.

3.1. Heat and Mass Transfer Analogy

In order to obtain local film cooling effectiveness values, direct thermal experiments have to be performed using a thermally insulated wall. However, it is difficult to maintain an adiabatic wall during experiments especially near the coolant injection orifices. This difficulty can be avoided by employing the heat-mass transfer analogy. In the heat-mass transfer analogy, the small temperature difference between the mainstream and the injection flow can easily be created by the use of a tracer gas mixed with the injection flow. The impermeable wall then gives the analogous boundary condition of the adiabatic wall.

The mass transfer process is analogous to the heat transfer process if the equivalent dimensionless parameters of the flow are the same in the two cases and if the Lewis number is unity (Goldstein, 1971). The Lewis number of the gas mixture is fairly constant near unity. Available experimental evidence, as well as theoretical considerations, have pointed to the fact that the turbulent Lewis number, which is defined as the ratio of turbulent heat transfer diffusivity and the turbulent mass transfer diffusivity,

27

has the value unity (Eckert and Drake, 1987). It is found that for heat transfer in the environment of turbulent flow, i.e., away from the near-wall region, the turbulent contribution to the energy and to the heat flux is generally more important than the molecular contribution. Therefore, even though the laminar Lewis number may deviate from unity, the mass transfer process still represents the heat transfer process adequately.

In the present experiments, the injection gas consists of air with about 0.03 percent propane so that the density ratio between the mainstream and injection flow is essentially unity, thus representing results comparable to low temperature differences. The film cooling effectiveness can therefore be expressed by the relative concentration of propane to the plenum concentration

$$\eta = \frac{C_w - C_\infty}{C_c - C_\infty} \tag{3.1}$$

where C_w is the relative concentration on the wall and C_∞ and C_c are the relative concentration in the mainstream and injection, respectively. In the present experiments, the injected gas contains a single constituent not contained in the mainstream, thus $C_\infty = 0$, $C_c = 1$ and

$$\eta = C_w \tag{3.2}$$

3.2. Experimental Facility and Equipment

3.2.1. Wind Tunnel

The experiments were performed in a low speed, blower-type, boundary layer wind tunnel with a test section measuring 406 mm wide, 267 mm high, and 800 mm long (See Figure 3.1). The tunnel had a turbulence intensity of less than 0.5 percent at a free stream velocity of 10 m/s. The side walls and the tunnel floor in the test section were constructed of plexiglass. The top wood roof was adjusted to have zero pressure gradient on the flow when no secondary flow is injected. In order to ensure that the boundary layer formed by

the free stream is fully turbulent, a trip wire was used at the inlet of the test section to ensure transition. The boundary layer thickness upstream of the holes was about 1.5 cm.

3.2.2. Injection System

The test section was augmented for the experiments by the addition of a plenum module. The plenum beneath the test section (shown in Figure 3.2) is 908 mm long and 406 mm in diameter. The plenum module facilities controlled the injection of the secondary stream into the mainstream. The plenum floor was designed to accommodate a wide variety of slot and orifice geometries. The plenum air was supplied from the building's main air compressor which has a rated capacity of 250 scfm at 150 psi. Before reaching the plenum, the compressor air travels a long distance through piping, a condensing filter, two pressure regulators, and a rotameter. The condensing filter removes water and oil from the compressed air. The two pressure regulators were used in series to reduce pressure fluctuations in the supply line. The propane injection tap was connected to the piping upstream of the rotameter. The propane and the compressed air were well mixed by a fan mixer. The flow rate fluctuation was less than ± 0.25 scfm in the present experiments. The rotameter was used to measure the mass flow rate of air into the plenum and therefore into the mainstream.

3.2.3. Traverse Mechanism

Above the wind tunnel roof are two rails which support the hot wire anemometer traverse mechanism. These rails run the full length of the test section. The traverse mechanism is capable of movement in the longitudinal, lateral, and vertical directions. Good quality bearings were used in the traverse mechanism to allow accurate positioning (with accuracy of about 0.0127 mm in these three directions). Movement of the traverse mechanism was done by hand with the aid of one dial gauge which is accurate to 0.254 mm. The wind

tunnel roof had several slots, allowing two-dimensionality checks of the boundary layer at the locations of interest.

3.2.4. Data Acquisition System

In order to obtain and process data, a computer data acquisition system was developed with a Lab-PC A/D board of National Instruments (see National Instruments Lab-PC manual, 1991). A schematic of the data acquisition system is shown in Figure 3.3. The board has a 12-bit successive approximation analog-to-digital converter with eight analog inputs, and two 12-bit digital-to-analog converters with voltage outputs. The board converts the voltage signals from the hot-wire anemometer and the flame ionization detector to a personal computer, and delivers analog signals to control the scanning valve for the sampling of each tube. The data acquisition program written in the C language communicates with the board and also processes the data. The sampling parameters are shown in Table 3.1. The A/D board is accurate to within 0.01%, so the error can be ignored.

Table 3.1: Sampling parameters of the data acquisition system.

Source of the Voltage Signals	Sampling Frequency	Sampling Numbers	Sampling Gain
Hot-Wire Anemometer	3 kHz	25,000	1
FID	150 Hz	2,500	1

3.3. Measurement Techniques

The quantities measured in this study include concentration of propane, mean flow velocity, and turbulence intensity. A general outline of the techniques and equipment used follows.

3.3.1. Measurement of Concentration

The concentration of propane was measured by the flame ionization detector (FID) which provides continuous measurements of fluctuating concentration in turbulent flows. Figure 3.4 illustrates the FID system (See Fackrell, 1980 for the details of this instrument). The sample gas, i.e. the mixture of air and propane, is sucked directly into the FID along a short length of tubing. The FID consists of a hydrogen-in-air flame burning in an insulated flame chamber across which a voltage is applied. The introduction of a hydrocarbon gas into the flame leads to the production of ions and hence a current. An electrometer amplifier is used to convert this small current to a suitable voltage output. The voltage output is assumed to be linear with the concentration of sampled gas

$$E - E_0 = \alpha C \qquad\qquad (3.3)$$

where E is the voltage output, E_0 is the voltage output when sample gas is absent, C is the concentration of sample gas, and α is a constant. The linearity of the FID system over the range of our experiments is shown in Figure 3.5.

In the experiments, concentrations were measured with a rake of eleven very fine sample tubes (0.3 mm outside diameter) at locations of interest. (see fig 3.2) Gas mixture was sampled through these tubes and sent, through a scanning valve, to the FID, which accurately measures mean propane concentration. Since the response was found to be linear with concentration (at least in the range 1 to 10,000 ppmv propane), only one calibration constant and a zero reading need be obtained. Before beginning the test, each tube was calibrated individually from two known concentrations of propane, i.e. C_∞ and C_c. This calibration was then recorded in the computer. By sampling alternately from the plenum to check C_c and then from a tube to find C, before switching to a new sampling tube, errors were minimized to within 2.5%. Random spikes observed on the output signal at the high sensitivity setting, caused by small particles in the sampled air, were reduced by

electronically low-pass filtering the signal at a low frequency of 300 Hz. The overall error of cooling effectiveness measurements was estimated to be ±0.05 as shown in Table 3.2.

3.3.2. Measurement of Fluid Velocity

The mean and fluctuating velocities were measured using a DISA constant temperature anemometer system. The hot-wire probe is standard DISA single wire probe, with a 5 μm diameter, 1.25 mm length platinum-coated tungsten wire. The hot-wire anemometer bridge was operated at a 1.6 overheat ratio. This ratio is 20 percent lower than the ratio recommended by DISA; however, the lower ratio allows a longer useful life of the wire. The voltage signal, produced by the anemometer bridge, is passed through a 10 kHz low pass filter before reaching the AD converter. The 10 kHz frequency was chosen to eliminate high frequency noise without affecting the lower frequency signal components. The hot-wire probe was calibrated, using King's law with an exponent of 0.45, against a Pitot static probe in low turbulence conditions (with the turbulence intensity $\sqrt{\overline{u'^2}}/U < 0.5\%$). A typical calibration is shown in Figure 3.6. A lookup table was obtained based on the calibration and to be used for the measurements. A digital sampling rate of 3 kHz was used for all measurements. The uncertainty in the measurements was usually within ±0.02 m/s for the mean velocities and within ±0.04 m/s for the fluctuating velocities given in Table 3.2. The hot-wire probe was mounted to a dial gauge which was used to measure the position normal to the plate surface with accuracy of $\pm 1.3 \times 10^{-2}$ mm.

3.3.3. Determination of 2-D Injection Flow Reattachment

In two-dimensional tests, the size of the separation bubble downstream of the injection orifice was estimated using a simple flow visualization technique. Tufts were arranged on the wall surface and the point of reattachment was determined by the direction change of the tufts on the surface. The error involved was estimated at less than ±1/2 slot width.

3.3.4. Measurement Uncertainties

The measurement uncertainties were estimated by taking into account the flow meters, Pitot tubes, gauges, rulers, and other control parameters used in the experiments. Table 3.2 summarizes the uncertainties involved in the measurements.

Table 3.2: Summary of the measurement uncertainties.

Measured Quantity	Estimated Uncertainty
U (Hot wire)	± 0.02 m/s (for $\sqrt{\overline{u'^2}}/U < 0.5\%$)
$\sqrt{\overline{u'^2}}$ (Hot wire)	± 0.04 m/s (for $\sqrt{\overline{u'^2}}/U < 0.5\%$)
η (FID)	± 0.05
x	1 mm (for η)
y	0.254 mm (for velocities)
y	1 mm (for η)
z	1 mm (for η)

3.4. Experimental Measurements

3.4.1. 2-D and 3-D Wind Tunnel Models

The 2-D model was built to carry out measurements of film cooling effectiveness and velocity fields. The model and the corresponding coordinate system are shown in Figure 3.7a. The 2-D model consists of a vertical slot made in the plexiglass floor of the test section. The slot has a width of $d=6.35$ mm and a height of about $5d$.

Figure 3.7b shows the 3-D film cooling model and the corresponding coordinate system. The 3-D model consists of a row of six square holes made in the plexiglass floor of the test section. Each injection slot has a cross section width of $d=12.7$ mm, a height of about $5d$, and a spanwise spacing of $S=3d$.

3.4.2. Upstream Boundary Layer

Tests were carried out to investigate the two-dimensionality of the upstream boundary layer. The mean velocity and turbulence intensity within the boundary layer were measured upstream of the injection orifices at three different spanwise locations, as shown in Figures 3.8 and 3.9. The two-dimensionality of the upstream boundary layer is reached with maximum deviations of ±0.3 m/s in the mean velocity and ±0.6 m/s in the fluctuating velocity. Figure 3.11 shows the mean velocity profile with respect to the logarithmic coordinate y^+ ($y^+ = \frac{yU_\tau}{v}$, $U_\tau = \sqrt{\tau_w / \rho}$). A clear logarithmic region is observed showing that the upstream boundary layer is fully turbulent. The turbulent shear stress τ_w, is calculated by fitting the velocity profile to the logarithmic law

$$\frac{U}{U_\tau} = \frac{1}{\kappa}\ln(Ey^+)$$

(3.4)

where κ is the von Karman constant ($\kappa = 0.41$), and E is a constant of integration ($E = 9.0$). It is estimated that $\tau_w = 0.32$ kg/ms^2. Near the viscosity-affected region, the velocity profiles do not fit the linear profile as expected. This discrepancy is due to the fact that mean velocity cannot be measured accurately very close to the wall using the present hot-wire anemometer. Since the upstream boundary layer has a significant influence on the effectiveness downstream, the measured flow fields were used as the inlet boundary conditions for the computations (Details will be given in Chapter 6).

3.4.3. Preliminary Tests for the 2-D Model

Preliminary tests were carried out to investigate the two-dimensionality of the coolant injected from the slot and conservation of the injected gas. The vertical distributions of concentration at three different locations three slot-widths downstream of injection (*X/d=3*) are shown in Figure 3.11. The two-dimensionality of the injection flow is reached with a maximum deviation in the cooling effectiveness of ±0.08. The amount of injected gas mixture at the slot must be the same as that observed downstream of the

injection. Since the propane was well mixed with the air before the injection, the conservation of the injected gas can be examined by integrating the velocity and concentration profiles along a cross-section at locations downstream of injection

$$M = \int_0^\infty CU dy \qquad (3.4)$$

where M is mass flux of injected gas, C is the concentration of the injected gas and U is the local mean velocity. Table 3.3 shows the flux balances between the injected mixture and the measured mixture at a location downstream of the injection for two mass flow ratios. The error in the flux balances observed are less than 10% which is consistent with the errors involved in both the velocities and concentration measurements. This check provides confidence in the techniques involved and also in the two-dimensionality of the injection system.

Table 3.3: Flux balance of 2-D injectant, $(M_{measured} - M_{injected})/M_{injected}$.

X/d	$R_M = 0.2$	$R_M = 0.4$
3	-1.58%	+7.67%

3.4.4. Preliminary Tests for the 3-D Model

The uniformity of the injection jets from each hole is examined by measuring the surface concentration and the concentration along the center line of each hole downstream of injection at $X/d=3$. These results are shown in Figures 3.12 and 3.13. The variation in the measured cooling effectiveness from all the holes is within ±0.10. While larger deviations were found only in the two side holes, i.e. Holes 1 and 6, the uniformity can be considered adequate. The measurement used here were taken from downstream of Hole 3.

3.4.5. Measurement Procedure

In the 2-D measurements, the concentration of the injection flow was measured along the streamwise vertical plane downstream of the injection slot and the measurements were carried out for three mass flow ratios, $R_M = 0.2, 0.4, 0.6$ with the main stream velocity, $U_\infty = 10m/s$. Both mean velocity and turbulence intensity were measured downstream of the injection but only for mass flow ratios of $R_M = 0.2, 0.4$. The reattachment lengths of injected fluid were observed from the simple flow visualization (see Section 3.3.3). The measured effectiveness distribution and flow fields are described in Chapter 6 where they are compared with computed results.

In the 3-D measurements, the concentration of the injection flow was measured on the wall surface and the measurements were carried out for three mass flow ratios, $R_M = 0.2, 0.4, 0.8$ with the main stream velocity, $U_\infty = 10m/s$. For mass flow ratios of $R_M = 0.4, 0.8$, both mean velocity and turbulence intensity were measured downstream along the central line of the injection holes. Because of the symmetry of the flow field, the velocity measured along the central line of injection holes by the normal single wire represents the local streamwise mean velocity and turbulence intensity. The experimental measurement data are presented in Chapter 7 where they are compared to numerical predictions.
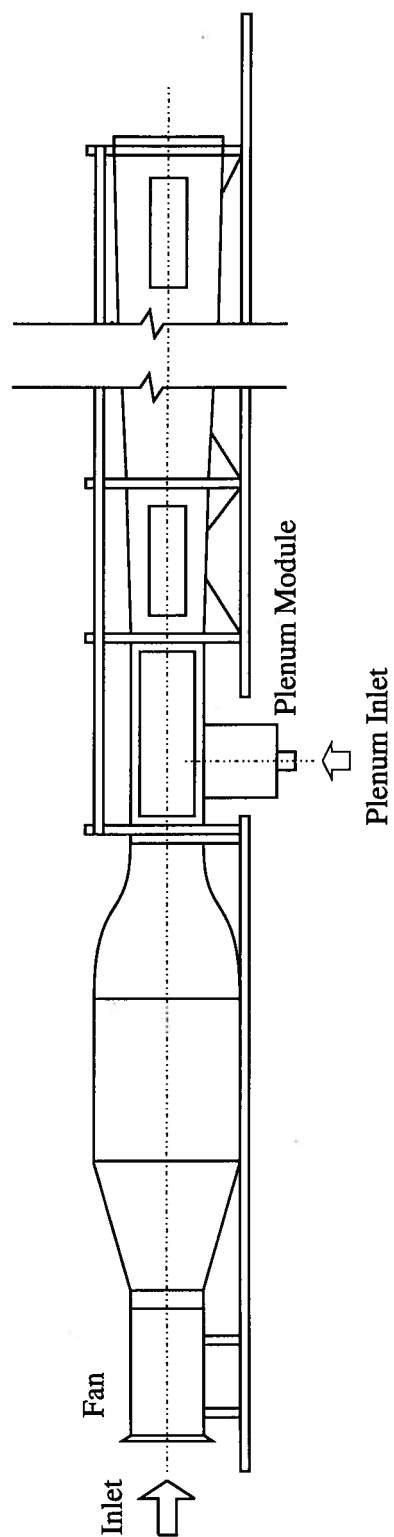
Figure 3.1: Schematic of wind tunnel.

Wind Tunnel Test Section
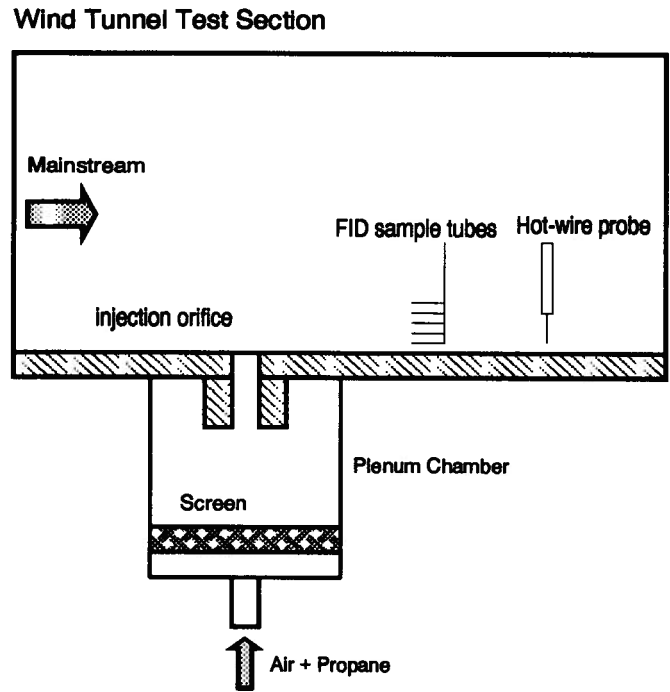
Figure 3.2: Schematic of test section.
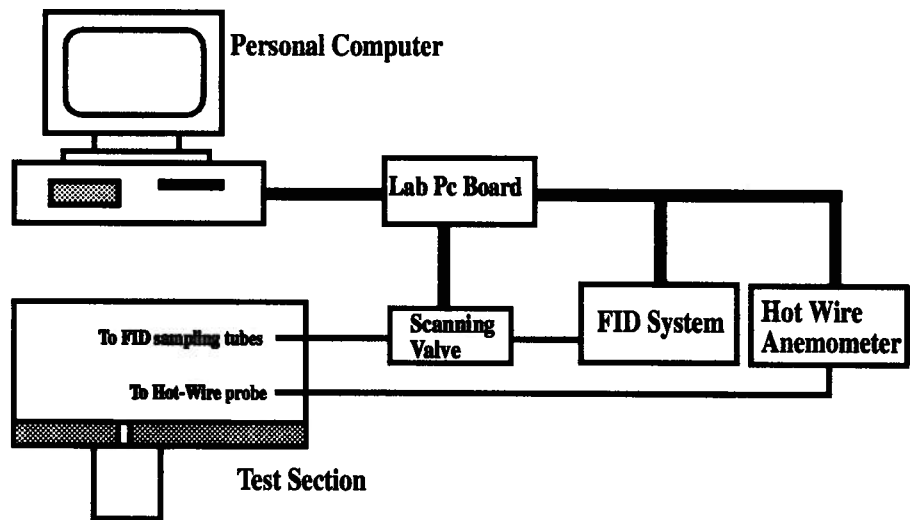
Figure 3.3: Schematic of data acquisition system
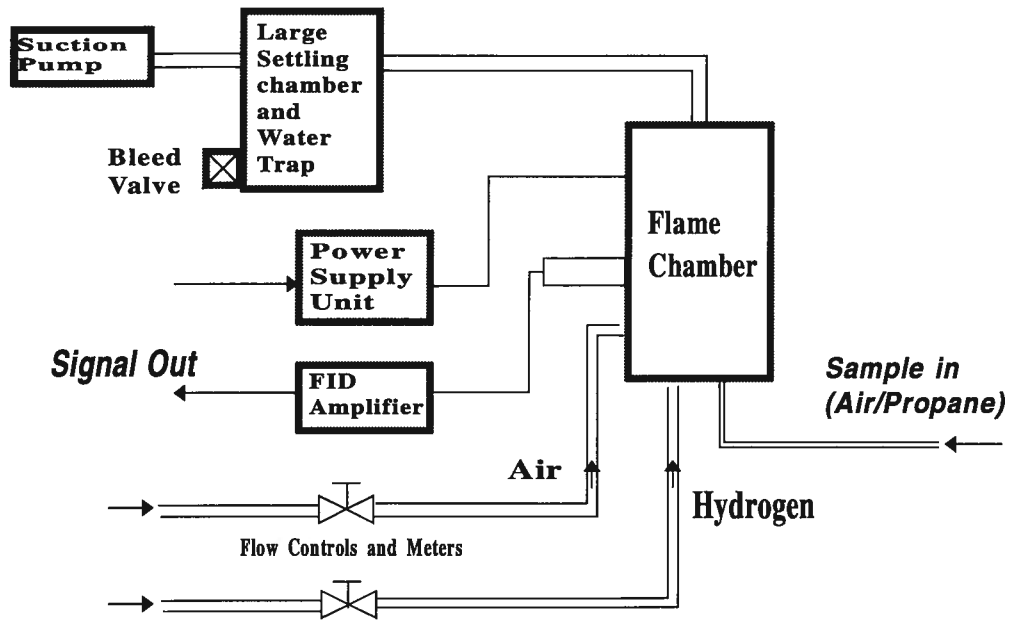
Figure 3.4: Schematic of FID system.
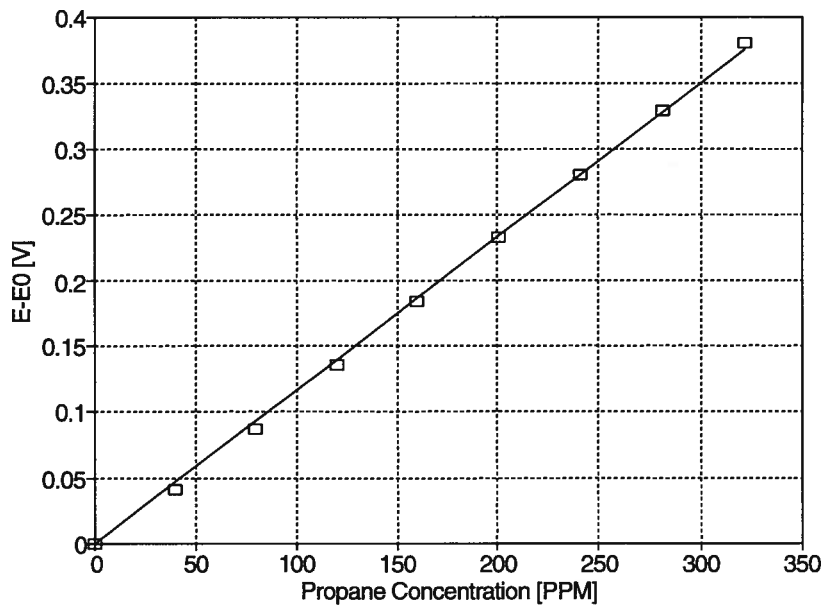
Figure 3.5: Calibration of FID system.
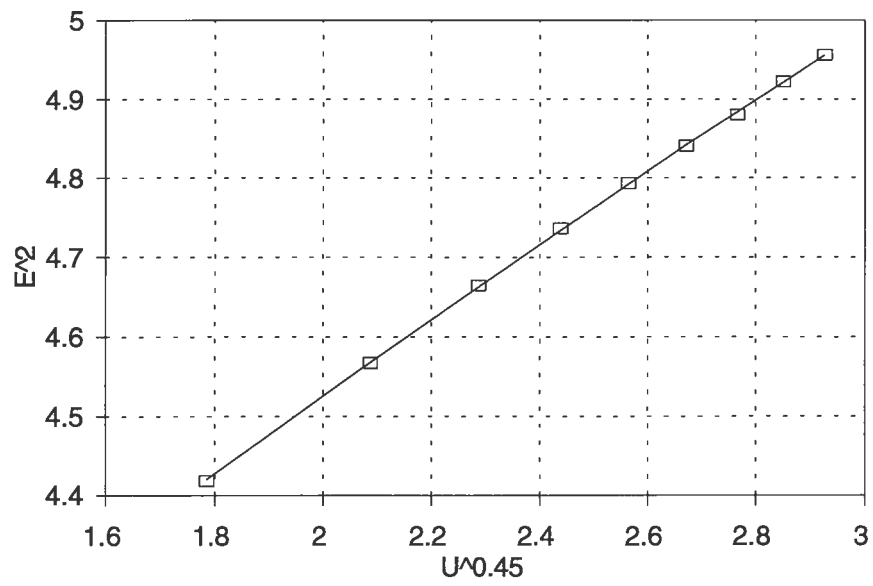
Figure 3.6: Calibration of the hot wire probe (E in volts, U in m/s).
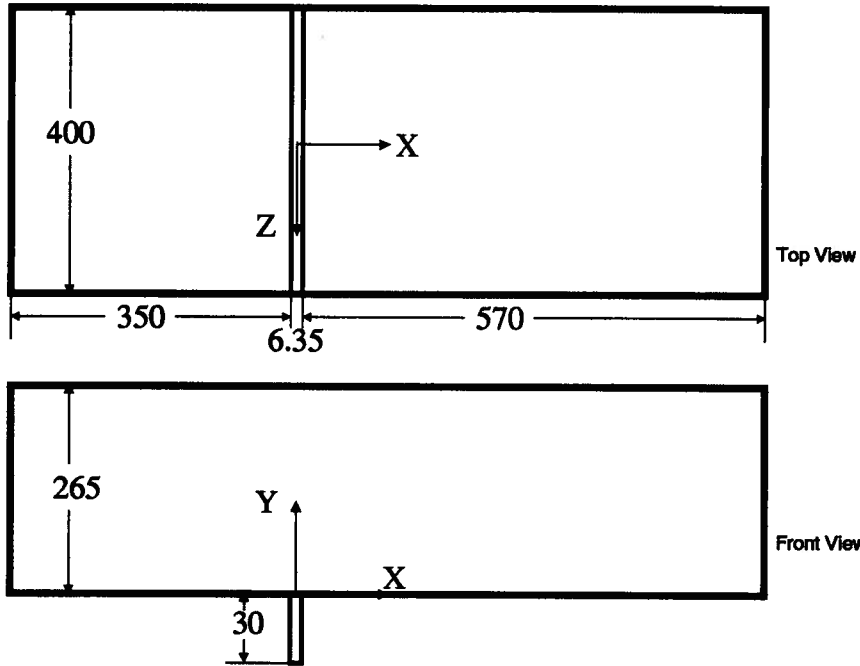
(a) 2D Model
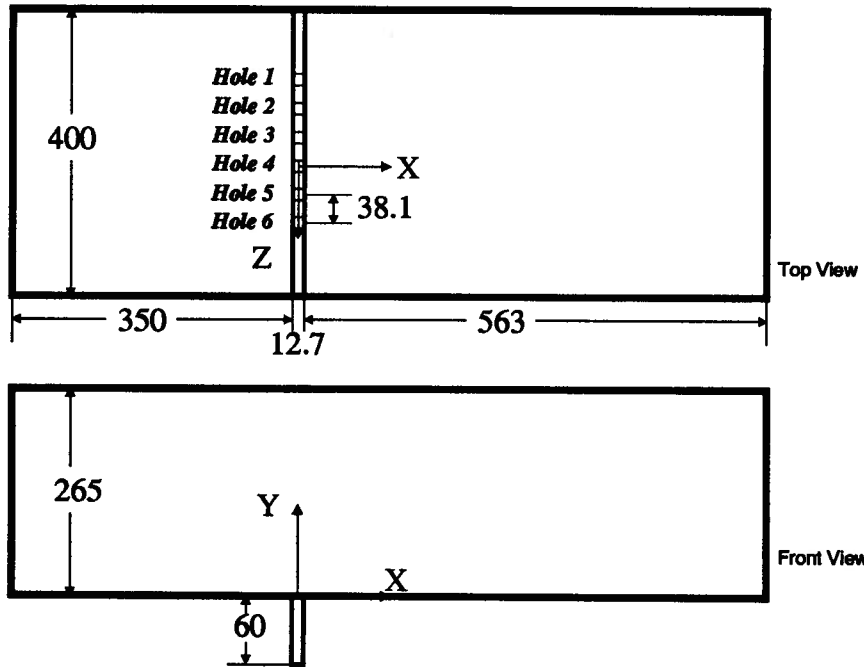
Figure 3.7: Geometric description of the 2-D and 3-D Models.

(b) 3D Model
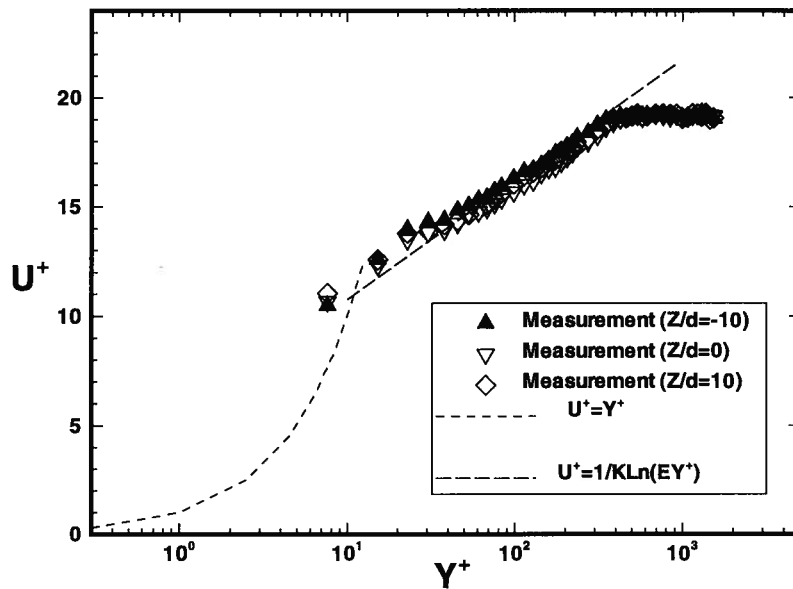
Figure 3.8: Measured mean velocity of the upstream boundary layer on the logarithmic coordinate ($X = -120mm$).
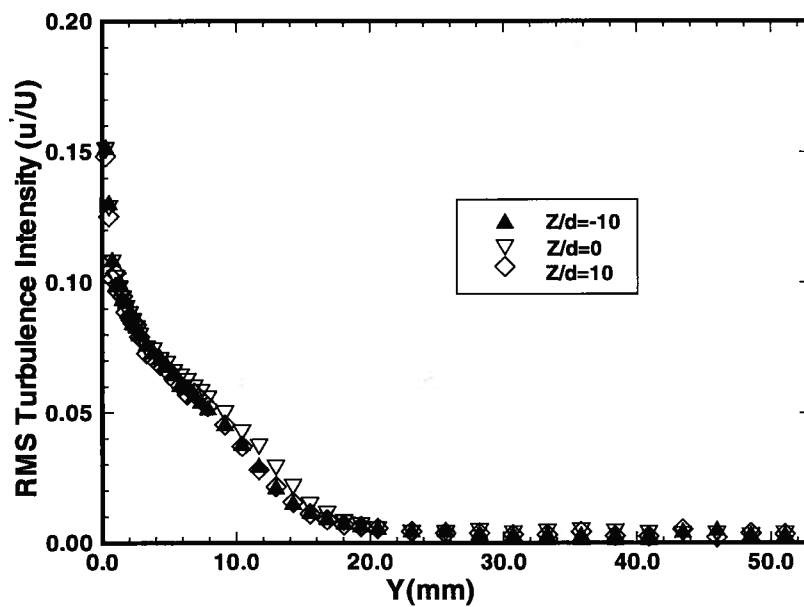
Figure 3.9:   Measured turbulence intensity of the upstream boundary layer ($X = -120mm$)
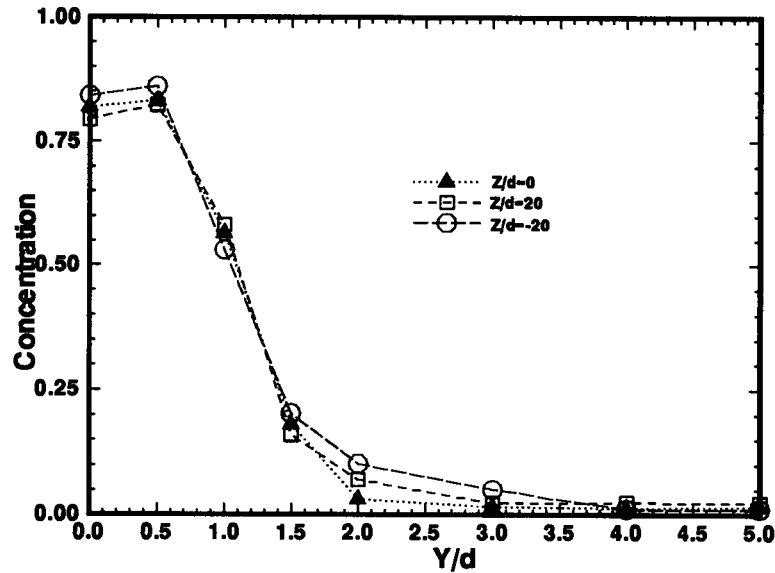
Figure 3.10: Measured concentration along the streamwise vertical lines downstream of the injection slot ($X/d = 3$, $d = 6.35$mm, 2-D model).
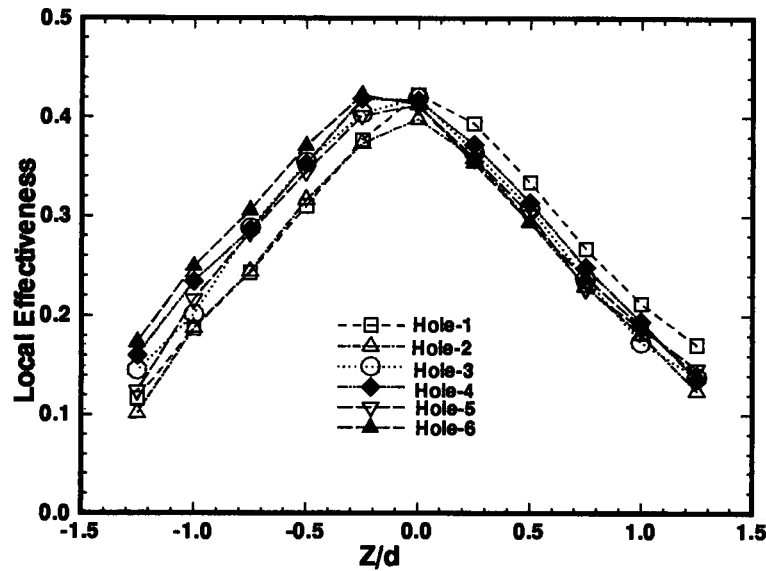
Figure 3.11: Measured surface concentration downstream of the injection holes on the transplated coordinate ($X/d = 3$, $d = 12.7$mm, 3-D model).
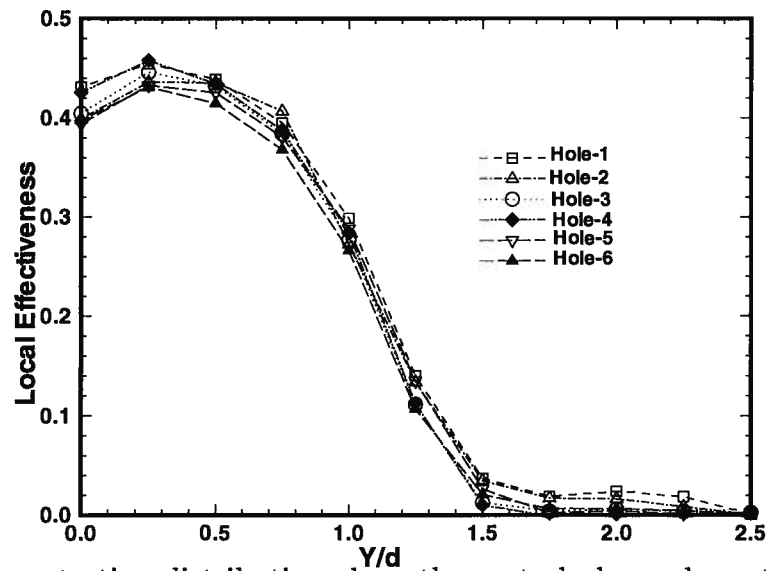
Figure 3.12: Concentration distribution along the central planes downstream of the injection hole ($X/d = 3$, $d = 12.7$mm, 3-D model).

Chapter 4

Mathematical Formulation

In the present computations of film cooling effectiveness, the flow and heat transfer is assumed as steady state and incompressible. From the principles of conservation of mass, momentum and energy and by using the Reynolds ensemble-averaging procedure, the equations for the ensemble-averaged properties of turbulent flows and the associated heat transfer in Cartesian tensor co-ordinates are (see Rodi, 1984 for details):

Mass conservation equation:

$$\frac{\partial \rho U_i}{\partial x_i} = 0 \tag{4.1}$$

Momentum conservation equation:

$$\frac{\partial (\rho U_k U_i)}{\partial x_k} = -\frac{\partial P}{\partial x_i} + \frac{\partial}{\partial x_k}\left[\mu\left(\frac{\partial U_i}{\partial x_k} + \frac{\partial U_k}{\partial x_i}\right) - \rho \overline{u_i' u_k'}\right] \tag{4.2}$$

Scalar transport equation:

$$\frac{\partial (\rho U_k \Phi)}{\partial x_k} = \frac{\partial}{\partial x_k}\left(\gamma \frac{\partial \Phi}{\partial x_k} - \overline{u_k' \phi'}\right) \tag{4.3}$$

where U_i ($i=1,2,3$) and P represent the mean velocities and static pressure, respectively, Φ denotes a scalar variable, and μ and γ are the fluid dynamic viscosity and the scalar molecular diffusivity. This system of equations contains unknown variables, the Reynolds stresses $\overline{u_i' u_j'}$ and turbulent scalar flux $\overline{u_i' \phi'}$. In order to obtain a closed set of equations, some assumptions must be made to relate the Reynolds stresses and the turbulent scalar flux to other existing variables through the procedure called turbulence modelling.

In the following sections, two turbulence models used in the present study are described, i.e., the k-ε model and the multiple-time-scale model (M-T-S). A simplified algebraic stress model is introduced for the 3-D film cooling flow. Two near-wall turbulence treatments, i.e., the wall function (WF) and the low-Re k model (LK) with a near-wall fine grid are also discussed.

45

4.1. Turbulence Models

The essence of turbulence modelling is to represent the unknown Reynolds stresses and turbulent scalar flux in terms of known parameters. There are two main categories of modelling approaches. One category, called turbulent-viscosity modelling, is based on the suggestion of Boussinesq (1877) that Reynolds stresses can be represented in terms of mean strain-rates (by analogy with laminar Newtonian flows). The second category, called turbulent-stress modelling, is based on the development of differential equations describing the transport of individual stresses (Launder and Spalding, 1972).

4.1.1. Eddy Viscosity and Diffusivity Concepts

The eddy-viscosity concept can be represented by the following equation:

$$-\rho \overline{u_i' u_j'} = -\frac{2}{3} k \delta_{ij} + \mu_t \left(\frac{\partial U_i}{\partial x_j} + \frac{\partial U_j}{\partial x_i} \right) \tag{4.4}$$

where μ_t is the turbulent eddy viscosity, k is the kinetic energy of the turbulent motion

$$k = \frac{1}{2} \overline{u_i' u_i'} \tag{4.5}$$

and δ_{ij} is Kronecker delta. By direct analogy to turbulent momentum transport, turbulent scalar transport is often assumed to be related to the gradient of the transport quantity

$$-\overline{u_i' \phi_j'} = \Gamma_t \frac{\partial \Phi}{\partial x_j}_t \tag{4.6}$$

where Γ_t is the turbulent diffusivity of the scalar. The Reynolds analogy between scalar transport and momentum transport suggests that Γ_t is closely related to μ_t , i.e.

$$\Gamma_t = \frac{\mu_t}{\sigma_t} \tag{4.7}$$

where σ_t is the turbulent Prandtl number or the turbulent Schmidt number.

Experiments have shown that unlike the turbulent diffusivities for momentum and scalar quantities, σ_t varies only slightly across any flow or from flow to flow (Rodi, 1984). Many turbulence models make use of Equation 4.7 with the turbulent

Prandtl/Schmidt number as a constant (e.g., $\sigma_t = 0.9$ for wall bounded flow). The relation given by Equation 4.6 has proved useful in many practical calculations.

The major drawbacks associated with the standard turbulent-viscosity models are their assumptions of isotropic and equilibrium turbulence and that turbulent scalar flux must be zero at zero gradient points. An alternative approach is the use of the Reynolds stress model which calculates the individual Reynolds stresses from their respective transport equations that are obtained directly from the instantaneous momentum equations. However, these transport equations contain further unknown, higher-order statistical correlations which have to be modelled in terms of known, mean parameters. Previous work has shown that there is still much work to be done to attain a complete and accurate (or even useful) representation of the correlations.

The turbulence model incorporated in the present study is based on the turbulent-viscosity approach. The concept of anisotropic turbulence is introduced through the implementation of the turbulent eddy-viscosity and eddy-diffusivity plus a simplified formulation of the Reynolds stress model. Non-equilibrium turbulence is introduced through the multiple-time-scale model, which takes into account the time scales of both large and small eddies.

4.1.2. The k-ε Turbulence Model

The two-equation k-ε turbulence model uses the eddy-viscosity concept and the Kolmogorov-Prandtl expression in which the eddy viscosity can be considered proportional to a velocity characterizing the fluctuating motion proportional to $\sqrt{k}$ and to a typical length of this motion,

$$\mu_t \propto \rho \sqrt{k} l \tag{4.8}$$

where l is the mixing length. The quantities k and l are related to the dissipation rate of turbulent kinetic energy, ε, by dimensional analysis (Rodi, 1984)

$$\varepsilon \propto \frac{k^{3/2}}{l} \qquad (4.9)$$

Combining these two expressions, we obtain

$$\mu_t = \rho C_\mu k^2 / \varepsilon \qquad (4.10)$$

where C_μ is an empirical constant.

For high turbulent Reynolds number flow ($\mathrm{Re}_t = k^2/\nu\varepsilon > 100$), the distribution of k can be determined by solving the transport equation which can be expressed as

$$\frac{\partial \rho U_i k}{\partial x_i} - \frac{\partial}{\partial x_i}\left(\frac{\mu_t}{\sigma_k}\frac{\partial k}{\partial x_i}\right) = \rho G - \rho\varepsilon \qquad (4.11)$$

where σ_k is assumed to be a constant and G is the generation rate of turbulent kinetic energy

$$G = \overline{u_i u_j}\left(\frac{\partial U_i}{\partial x_j}\right) \qquad (4.12)$$

The equation for ε contains complex correlations whose behavior is not well known and is usually presented in the following form:

$$\frac{\partial \rho U_i \varepsilon}{\partial x_i} - \frac{\partial}{\partial x_i}\left(\frac{\mu_t}{\sigma_\varepsilon}\frac{\partial \varepsilon}{\partial x_i}\right) = C_1 \rho \frac{\varepsilon}{k} G - C_2 \rho \frac{\varepsilon^2}{k} \qquad (4.13)$$

where σ_k, C_1, C_2 are the modelling constants. These constants have been obtained based on the experimental observations of grid-generated turbulence and near-wall turbulent flows (Launder and Spalding, 1974). The commonly accepted values of these constants for incompressible flows are shown in Table 4.1 and are used here. Solutions of the two transport equations for k and ε completely define the turbulent parameters which can subsequently be used to close the Reynolds-averaged Navier-Stokes equations.

Table 4.1: k-ε turbulence model constants.

C_μ	C_1	C_2	σ_k	σ_ε
0.09	1.44	1.92	1.0	1.3

4.1.3. Nonisotropic Eddy-Viscosity Relation

In film cooling flow with discrete injection, the pressure field created by the injection is sufficiently strong so that the Reynolds stress terms in the momentum equation (Equation 4.2) have little direct effect on the mean velocity field in the immediate vicinity of the injection orifice. Downstream of injection, however, it is the turbulent stress field that causes the flow field to approach a two-dimensional form. In the film cooling flow, the existence of nonisotropic turbulence near the adiabatic wall results in the underprediction of the lateral near wall spreading by computations which use the isotropic k-ε turbulence model.

A nonisotropic eddy-viscosity relation was proposed by Bergeles et al. (1981), based on the algebraic Reynolds stress model of Launder et al. (1975)

$$\overline{u_i u_j} = \frac{2}{3}\delta_{ij}k + C_s \frac{k}{\varepsilon}\left(G_{ij} - \frac{2}{3}\delta_{ij}G_{kk}\right) \tag{4.14}$$

where C_s is a constant ($C_s = 0.27$) and the local generation rates of $\overline{u_i u_j}$ are:

$$G_{ij} = -\left(\overline{u_i u_k}\frac{\partial U_j}{\partial x_k} + \overline{u_j u_k}\frac{\partial U_i}{\partial x_k}\right) \tag{4.15}$$

By assuming that the flow is in local equilibrium and fully developed, the primary turbulence stresses can be simplified by (not tensor form):

$$-\rho\overline{u'v'} = \mu_y \frac{\partial U}{\partial y} \qquad -\rho\overline{u'w'} = \mu_z \frac{\partial U}{\partial z} \tag{4.16}$$

where y is the direction perpendicular to the wall, and x and z represent the streamwise and the cross-streamwise directions of the flow, respectively. The turbulent viscosity is related to the turbulence intensity (detailed derivation is given by Bergeles et al., 1981)

$$\mu_i = 0.27k\overline{u_i'^2}/\varepsilon \qquad i = x, y, z \tag{4.17}$$

By using the measured data of fully developed pipe flow, the following curve fit was used to represent a linear decay of the turbulence anisotropy from the wall to the outer edge of the boundary layer

$$\frac{\overline{(w')^2}}{\overline{(v')^2}} = 1.0 + 3.5\left(1 - \frac{y}{\delta}\right) \qquad y < \delta \tag{4.18}$$

$$\frac{\overline{(w')^2}}{\overline{(v')^2}} = 1.0 \qquad y \geq \delta \qquad (4.19)$$

where δ is the local boundary layer thickness defined in a suitable way.

Within the boundary layer, the lateral component of Reynolds stresses and scalar flux can then be written as

$$-\rho\overline{u'w'} = \mu_{t,z}\left(\frac{\partial U}{\partial z} + \frac{\partial W}{\partial x}\right) \qquad -\rho\overline{u'v'} = \mu_{t,y}\left(\frac{\partial U}{\partial y} + \frac{\partial V}{\partial x}\right) \qquad (4.20)$$

$$-\rho\overline{w'\theta'} = \frac{\mu_{t,z}}{\text{Pr}_t}\left(\frac{\partial \Phi}{\partial z}\right) \qquad -\rho\overline{v'\theta'} = \frac{\mu_{t,y}}{\text{Pr}_t}\left(\frac{\partial \Phi}{\partial y}\right) \qquad (4.21)$$

where

$$
\begin{aligned}
\mu_{t,z} &= \mu_t[1 + 3.5(1 - y/\delta)] & y < \delta \\
\mu_{t,y} &= \mu_t & y < \delta \\
\mu_{t,z} &= \mu_t & y \geq \delta \\
\mu_{t,y} &= \mu_t & y \geq \delta
\end{aligned}
\qquad (4.22)
$$

This replacement provides increased eddy viscosity and diffusivity in the lateral direction over that in the normal direction in the boundary layer region.

4.1.4. The Multiple-Time-Scale Turbulence Model

For film cooling at high mass flow rates, the turbulence exhibits more nonequilibrium behaviour: The production of turbulent kinetic energy and the dissipation rate vary widely in space. Such nonequilibrium turbulence cannot be resolved by the equilibrium eddy-viscosity concept (discussed in Section 4.2.2), which uses a single time scale to describe both the turbulent transport and the dissipation of the turbulent kinetic energy.

The multiple-time-scale (M-T-S) turbulence model developed by Kim and Chen (1989) considers separate time scales for large eddies and for fine-scale, small eddies. The turbulent kinetic energy spectrum is partitioned into the turbulent kinetic energy of large eddies k_p, and that of small eddies k_t. The turbulent kinetic energy k_p and k_t are governed by a system modelling equation. Instead of only considering the generation and dissipation of turbulent kinetic energy as in the k-ε model, the M-T-S model considers the

generation of turbulent kinetic energy from large eddies, the energy transfer rate from large eddies to small eddies, and the dissipation of small eddies. The turbulent kinetic energy and the energy transfer rate equations for large eddies are:

$$\frac{\partial \rho U_i k_p}{\partial x_i} - \frac{\partial}{\partial x_i}\left[\left(\frac{\mu + \mu_t}{\sigma_k}\right)\frac{\partial k_p}{\partial x_i}\right] = \rho G - \rho \varepsilon_p \qquad (4.23)$$

and

$$\frac{\partial \rho U_i \varepsilon_p}{\partial x_i} - \frac{\partial}{\partial x_i}\left[\left(\frac{\mu + \mu_t}{\sigma_\varepsilon}\right)\frac{\partial \varepsilon_p}{\partial x_i}\right] = C_{p1}\frac{\rho G^2}{k_p} + C_{p2}\frac{\rho G \varepsilon_p}{k_p} - C_{p3}\frac{\rho \varepsilon_p^2}{k_p} \qquad (4.24)$$

respectively. The turbulent kinetic energy and the dissipation rate equations for small eddies are:

$$\frac{\partial \rho U_i k_t}{\partial x_i} - \frac{\partial}{\partial x_i}\left[\left(\frac{\mu + \mu_t}{\sigma_k}\right)\frac{\partial k_t}{\partial x_i}\right] = \rho \varepsilon_p - \rho \varepsilon_t \qquad (4.25)$$

and

$$\frac{\partial \rho U_i \varepsilon_t}{\partial x_i} - \frac{\partial}{\partial x_i}\left[\left(\frac{\mu + \mu_t}{\sigma_\varepsilon}\right)\frac{\partial \varepsilon_t}{\partial x_i}\right] = C_{t1}\frac{\rho \varepsilon_p^2}{k_t} + C_{t2}\frac{\rho \varepsilon_p \varepsilon_t}{k_t} - C_{t3}\frac{\rho \varepsilon_t^2}{k_t} \qquad (4.26)$$

respectively, where the ε_p and ε_t equations were obtained from a physical dimensional analysis and the model constants were determined from the assumptions that the turbulence field of a uniformly-sheared flow can approach an asymptotic state in which G/ε_t becomes a constant and that the ratio of $\varepsilon_t/\varepsilon_p$ depends on the ratio of G/ε_t (details are given by Kim and Chen, 1989). The values of the modelling constants are as follows:

Table 4.2: M-T-S turbulence model constants.

$C_{\mu f}$	C_{p1}	C_{p2}	C_{p3}	C_{t1}	C_{t2}	C_{t3}	σ_k	σ_ε
0.09	0.21	1.24	1.84	0.29	1.28	1.66	0.75	1.15

The influence of nonequilibrium turbulence on turbulence transport is introduced through the eddy-viscosity equation, in which

$$\mu_t = C_{\mu f} k / \varepsilon_p \qquad (4.27)$$

where $C_{\mu f} = 0.09$ and $k = k_p + k_t$. The use of the energy transfer rate ε_p, instead of the dissipation rate ε_t indicates that the turbulence transport of mass and momentum is governed by the time scale of the energy containing large eddies rather than small eddies. The resulting eddy-viscosity coefficient C_μ (which is defined by $\mu_t = C_\mu k / \varepsilon_t$) is equal to $\varepsilon_t/\varepsilon_p$ which is a function of the ratio of the production of turbulent kinetic energy k and its dissipation rate G/ε_t as observed in experiments, instead of a constant as used in the k-ε turbulence model. Thus, the development of the mean fluid flow and the turbulence field is influenced by the spatially-varying turbulent viscosity, and the spatially-varying turbulent viscosity depends not only on the turbulence intensity but also on the degree of nonequilibrium turbulence.

4.2. Near-Wall Turbulence Treatments

The k-ε turbulence model is generally restricted to high Reynolds number conditions, where the effects of laminar viscosity can be neglected. Very close to the wall surface, in the laminar sublayer region, this assumption is no longer valid. The turbulence models should then incorporate the effects of laminar viscosity. In this thesis, two near-wall turbulence treatments are used: 1) wall function and 2) low-Re k model with near-wall refined grid. The use of the low-Re k model with fine near-wall grid allows for an improvement in the prediction of the flow and heat transfer near the wall surface, and hence an improved prediction of the film cooling effectiveness. The influence of these treatments is examined for both the flow field and heat transfer in film cooling.

4.2.1. Wall Function Approach

Since the velocity gradients are steep near the wall, an accurate representation of flow fields would require substantial numbers of grid points near the surface. For economy of computational cost, one common approach is to avoid the calculation of the flow within

the viscous sublayer by using wall functions. Wall functions bridge the laminar sub-layer region by matching the dependent variables appearing in the turbulence models to universal values at some point beyond the viscosity-affected region.

The standard wall function (Launder and Spalding, 1974) provides the boundary conditions, such as wall shear stress τ_w, the mean dissipation rate in the k equation and the dissipation rate, for a solid wall by locating the first computational grid point at a location sufficiently remote from the wall (say, y^+=30~300) where the flow is fully turbulent. The wall function method is based on two assumptions: first, the flow in the vicinity of a solid wall behaves locally as a one-dimensional Couette flow; second, the near wall turbulence characteristics are the same as those within the fully turbulent region.

In the fully turbulent region, the following assumptions were made in deriving the near-wall equations: 1) the turbulent shear stress is approximately constant and equal to the wall shear stress, 2) the pressure gradient is negligible, 3) the turbulent effect is dominant (i.e. $\mu_t >> \mu_l$), and 4) the flow is assumed to be in local equilibrium (i.e. the production and the dissipation rate of turbulent kinetic energy are locally in balance). Based on this assumption, the wall shear stresses can be determined from

$$\tau_w = \rho \kappa C_\mu^{1/4} k^{1/2} U / \ln(Ey^+) \tag{4.28}$$

The boundary conditions used for the kinetic energy and dissipation equations are:

$$k = C_\mu^{-1/2} \frac{\tau_w}{\rho} \tag{4.29}$$

$$\varepsilon = C_\mu^{3/4} \frac{k^{3/2}}{\kappa y} \tag{4.30}$$

Detailed descriptions can be found in Launder and Spalding (1974).

For the M-T-S model, the following boundary conditions can be used based on the local equilibrium assumption in the near-wall, fully turbulent region:

$$\frac{k_t}{k_p} = \frac{\kappa^2}{\sigma_{\varepsilon_p} C_\mu^{1/2} (C_{p3} - C_{p1} - C_{p2})} - 1 \tag{4.31}$$

$$\frac{\varepsilon_t}{\varepsilon_p} = 1 \tag{4.32}$$

4.2.2. Low-Re k Model with Fine Grid Treatment

In film cooling flow, very steep gradients of velocity, turbulent, and scalar quantities exist in the near-wall viscosity affected region and their modelling can have a significant impact on the prediction of film cooling effectiveness. The wall function treatment, however, limits the grid refinement near solid walls since it requires that the first grid point be located in the fully turbulent region. In order to achieve better numerical resolution, proper near-wall turbulence treatment is required.

The two-layer modelling approach has been introduced as a practical near-wall turbulence treatment. The approach summarized by Rodi (1991) uses the k-ε model away from the wall and resolves the viscosity-affected near-wall layer with a low-Reynolds number k model and a near-wall refined grid. In the model, the use of prescribed length scales in the viscosity-affected layer avoids the computation of the ε equation in this region where the gradient of ε is steep and higher numerical resolution is needed. Since a rather stiff differential equation for ε is omitted from the near-wall computational region, the level of computational difficulty is reduced. Only six or more grid points are required in the viscosity-affected layer for the two-layer approach.

The calculation procedure can be described as follows:

- The turbulence eddy-viscosity μ_t near the wall is obtained using the turbulence length scale l_μ with the aid of the van Driest damping function.

$$\mu_t = \rho C_\mu k^{1/2} l_\mu \tag{4.33}$$

$$l_\mu = \kappa C_\mu^{-3/4} \left[1 - \overset{3}{\exp}\left(\mathrm{Re}_t / A_\mu \right) \right] \tag{4.34}$$

where A_μ is a constant.

- The turbulent kinetic energy is calculated based on a prescribed length scale for the dissipation rate

$$\frac{\partial \rho U_i k}{\partial x_i} - \frac{\partial}{\partial x_i}\left(\frac{\mu_t}{\sigma_k} \frac{\partial k}{\partial x_i} \right) = \rho G - \rho \frac{k^{3/2}}{l_\varepsilon} \tag{4.35}$$

$$\varepsilon = \frac{k^{3/2}}{l_\varepsilon} \tag{4.36}$$

where a damping function similar to that used for the length scale l_μ is assumed as follows:

$$l_\varepsilon = \kappa C_\mu^{-3/4}\left[1 - \exp(\text{Re}_t/A_\varepsilon)\right] \tag{4.37}$$

and A_ε is a constant. The boundary condition for the k equation on the wall is simply $k=0$.

- The wall shear stress (τ_w) is determined from the velocity at the first node adjacent to the wall by assuming that this node is within the viscous sublayer so that:

$$\tau_w = \mu \frac{\partial U}{\partial y} \tag{4.38}$$

- The matching point for the standard k-ε model and the low-Re number k model is located at $y^+ = 50$. Usually, a sufficient number of grid nodes in the sublayer are about six or more.

The constants recommended by Rodi (1991) are:

$$A_\mu = 50.5, A_\varepsilon = 2\kappa C_\mu^{-3/4} \tag{4.39}$$

For the M-T-S model, the energy transfer rate and the dissipation rate inside the near-wall layer are given by Kim and Benson (1993) based on the local equilibrium assumption:

$$\varepsilon_p = \varepsilon_t = \frac{k^{3/2}}{l_\varepsilon} \tag{4.40}$$

and the values at the wall for k_p and k_t are assumed to be zero.

Chapter 5

Computational Procedure

In the present computations, two CFD codes: 2D-MGFD developed by Zhou (1990) and 3D-MGFD by Nowak (1991) were used for the 2-D and 3-D models, respectively. 2D-MGFD uses the traditional multi-grid FAS (Full Approximation Scheme) algorithm for the flow equations. In the present work, an improved SIMPLER solution algorithm for the flow equations and the M-T-S turbulence model are introduced into the code. This code was used as a testing tool for achieving efficient and stable solutions when a new turbulence model was introduced and also provided useful information for the improvement of the 3D-MGFD code. 3D-MGFD uses a new multi-grid correction scheme and Vanka's solution algorithm for the flow equations. In the present work, the LK near-wall turbulence treatment and the simplified algebraic Reynolds stress turbulence model were introduced into the code.

In this chapter, the finite volume formulation of the transport equations based on the hybrid difference scheme is described. A formulation is introduced to determine the numerical false diffusion resulting from the use of the upwinding scheme. The improved SIMPLER solution algorithm and the Vanka's scheme for the flow equations are presented. The multi-grid procedures used in 2D-MGFD and 3D-MGFD codes are also presented.

5.1. Finite Volume Formulation

The transport equations described in the previous chapter can be represented by the general transport equation

$$\frac{\partial(\rho U_j \phi)}{\partial x_j} = \frac{\partial}{\partial x_j}\left(\Gamma \frac{\partial \phi}{\partial x_j}\right) + S_\phi \tag{5.1}$$

where ϕ can be replaced for different equations ($\phi = U$ for the U-momentum equation for example), Γ is a general diffusivity coefficient, and S_ϕ a general source term. The discretized system of transport equations is formed on a staggered grid. The calculation domain is divided into a number of nonoverlapping control volumes and the staggered grid is arranged such that the velocity components are calculated on the faces of the control volumes. The locations for the velocity components and scalars (such as pressure, turbulence variables, and concentration/temperature) are shown in Figure 5.1. Due to the staggered grid arrangement, three different control volumes are required for the three velocity components, U, V, W.

The finite volume form of the general equation is obtained by integrating over the control volume. Figure 5.2 shows a typical control volume for any variable. Using Gauss' divergence theorem, the volume integrals can be transformed into surface integrals for the convective and diffusive fluxes across the control volume faces:

$$\underbrace{\int_{y_s}^{y_n}\int_{z_b}^{z_t}\left[\rho U\phi - \Gamma\frac{\partial\phi}{\partial x}\right]_{x_e} dydz}_{F_e} - \underbrace{\int_{y_s}^{y_n}\int_{z_b}^{z_t}\left[\rho U\phi - \Gamma\frac{\partial\phi}{\partial x}\right]_{x_w} dydz}_{F_w}$$

$$+\underbrace{\int_{x_w}^{x_e}\int_{z_b}^{z_t}\left[\rho V\phi - \Gamma\frac{\partial\phi}{\partial y}\right]_{y_n} dxdz}_{F_n} - \underbrace{\int_{x_w}^{x_e}\int_{z_b}^{z_t}\left[\rho V\phi - \Gamma\frac{\partial\phi}{\partial y}\right]_{y_s} dxdz}_{F_s}$$

$$+\underbrace{\int_{x_w}^{x_e}\int_{y_s}^{y_n}\left[\rho W\phi - \Gamma\frac{\partial\phi}{\partial z}\right]_{z_t} dxdy}_{F_t} - \underbrace{\int_{x_w}^{x_e}\int_{y_s}^{y_n}\left[\rho W\phi - \Gamma\frac{\partial\phi}{\partial z}\right]_{z_b} dxdy}_{F_b}$$

$$= \iiint_{cv} S_\phi dxdydz$$

where $F_e, ..., F_b$ represent the sum of the convective and diffusive fluxes across the faces e, ... ,b, respectively. For example, $F_e = C_e + D_e$ with

$$C_e = \int_{y_s}^{y_n}\int_{z_b}^{z_t}[\rho U\phi]_{x_e} dydz \qquad \text{and} \qquad D_e = \int_{y_s}^{y_n}\int_{z_b}^{z_t}-\left[\Gamma\frac{\partial\phi}{\partial x}\right]_{x_e} dydz \qquad (5.3)$$

The convective and diffusive fluxes across the control volume boundaries are expressed in terms of the nodal values of the dependent variable by using finite difference

approximations. The value of the dependent variable has to be determined at the control volume faces. The convective and diffusive flux terms (C_e, D_e, etc.) can be approximated using a power-law difference scheme (Patankar, 1980). The power-law scheme smoothly blends central differencing when the cell Reynolds number (based on the control volume width and the velocity of flow through the control volume face) is low, and upwind differencing when the cell Reynolds number is high. For problems where diffusion is dominant, central differencing is most appropriate and is second-order accurate. The use of central differencing leads to numerical instabilities, however, when the cell Reynolds number is larger than 2. Upwind differencing is used to counteract this instability, where the value of the dependent variable at the upstream node is assumed to prevail at the control volume face. This leads to an approximation which is unconditionally stable, but only first order accurate.

By using the power-law scheme for the surface integral, the general algebraic equation is obtained for each node P:

$$a_P \phi_P = a_E \phi_E + a_W \phi_W + a_N \phi_N + a_S \phi_S + a_T \phi_T + a_B \phi_B + b_P \qquad (5.4)$$

with

$$a_P = \sum_i a_i - S_P^\phi \qquad (i = E, W, N, S, T, B) \qquad (5.5)$$

and

$$a_e = D_e A(|P_e|) + \max(-F_e, 0) \quad \text{and} \quad a_w = D_w A(|P_w|) + \max(F_w, 0) \qquad (5.6)$$

where $A(|P|) = \max[0, (1 - 0.1|P|)^5]$, $P_e = F_e / D_e$, and $P_w = F_w / D_w$. The variable b_P represents the constant part of the linearized source term for each control volume. The source term S_ϕ is linearized as follows:

$$\iiint\limits_{cv} S_\phi \, dx \, dy \, dz = S_P^\phi \phi_P + S_U^\phi \qquad (5.7)$$

where S_P^ϕ and S_U^ϕ are derived using central differencing approximations. The modification of the discretization near the boundaries is described in detail by Djilali(1990).

Figure 5.1: Relative location of velocity and scalar variables in the staggered grid.
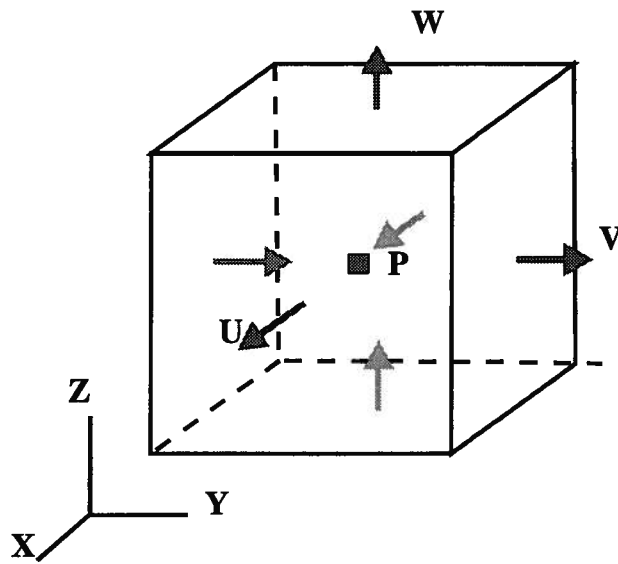
Figure 5.2: A typical control volume.
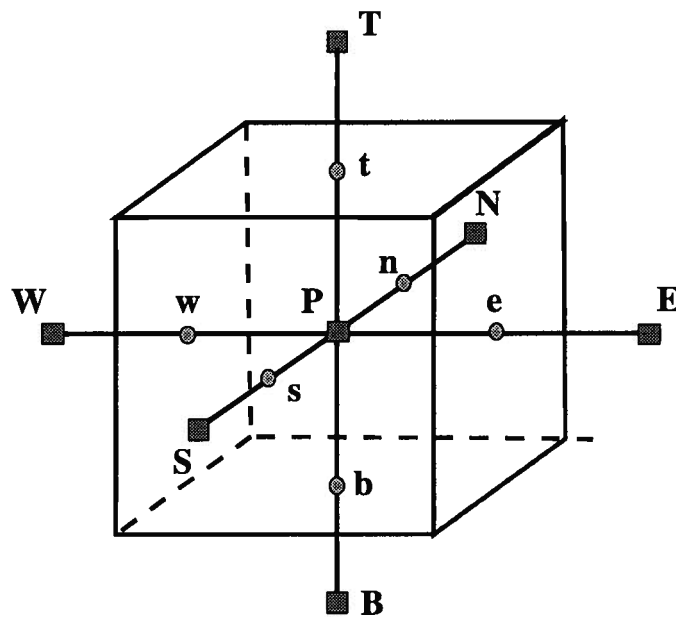
5.2. False Diffusion

The upwind differencing approximation of convective terms in the conservation equation which is employed for stability when the cell Reynolds number is larger than 2 is a first-order approximation. For the conservation equation, the first-order approximation of the convection term $C_e = \int_{y_s}^{y_n} \int_{z_b}^{z_t} [\rho U \phi]_{x_e} dy dz$ results in false diffusion which can be demonstrated in the following 1-D example as shown Figure 5.3.

Figure 5.3: Finite difference grid.
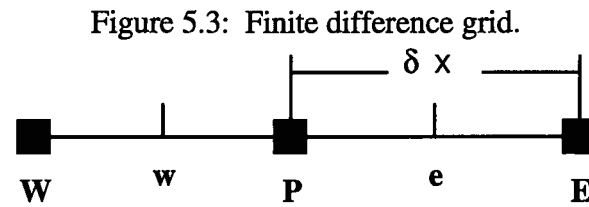
$$\phi_P = \phi_e - \frac{\delta x}{2} \left[\frac{\partial \phi}{\partial x} \right]_e + \frac{1}{2!} \left(-\frac{\delta x}{2} \right)^2 \left[\frac{\partial^2 \phi}{\partial x^2} \right]_e + \dots \tag{5.8}$$

where ϕ_P is the solution at node P and ϕ_e is the approximate solution at the node e. According to the upwind differencing scheme, $\phi_e = \phi_P$ when the cell Reynolds number at e is greater than 2. The error in the estimate of the convection flux due to this approximation is

$$-\rho_e U_e \left(\frac{\delta x}{2} \right) \left[\frac{\partial \phi}{\partial x} \right]_e \tag{5.9}$$

This has the form of a flux of ϕ by false diffusion with a diffusion coefficient $\Gamma_{False} = \rho_e U_e \frac{\delta x}{2}$. In 3-D flow, the false diffusion in directions normal and coincident with the velocity vector can be expressed by (see Demuren, 1985)

$$\Gamma_{f,\xi} = \frac{UV(U\Delta x + V\Delta y)}{2(U^2 + V^2)} \tag{5.10}$$

$$\Gamma_{f,\eta} = \frac{W \left[U^3 W\Delta x + V^3 W\Delta y + (U^2 + V^2)^2 \Delta z \right]}{2(U^2 + V^2 + W^2)(U^2 + V^2)} \tag{5.11}$$

$$\Gamma_{f,\zeta} = \frac{(U^3 \Delta x + V^3 \Delta y + W^3 \Delta z)}{2(U^2 + V^2 + W^2)} \tag{5.12}$$

where U, V, W are the velocity components in the Cartesian coordinates and (ξ, η, ζ) is a new Cartesian coordinate system which is chosen such that the ζ-axis is tangential to the velocity vector, and the ξ and η axes are normal to the velocity vector with the ξ-axis in the x-y plane. It can be shown that the false diffusion in 3-D computations is related to the inclination of the grid line to the mainstream and the gradient across the streamline. These expressions are useful in evaluating the false diffusion, and thus, estimating the numerical uncertainty involved in the computations.

Excessive false diffusion in the numerical scheme prohibits accurate representation of turbulent flow and the associated heat transfer. Most turbulence models (such as k-ε and M-T-S models) use the eddy-viscosity concept and the effective viscosity term varies with different turbulence models. The necessity of separating the numerical errors from the turbulence models becomes obvious when it is considered that one of the objectives of the present work is to evaluate the turbulence modelling methods for film cooling. In film cooling computations, the false diffusion coefficients in directions normal to the velocity vector can be significant sources of numerical errors, since convection often dominates and the gradient of physical variables along the streamline is relatively small.

Methods which can be used to reduce the false diffusion in computations include: 1) reducing the grid size, 2) altering the grid to follow the streamlines, 3) using a higher-order approximation scheme. A number of upstream-weighted differencing schemes of higher-order accuracy and satisfactory numerical stability have been proposed (Raithby, 1976 and Sidilkova and Ascher, 1994), but these methods suffer from complexity and lack of boundedness. In general, the higher-order approximation methods developed in the past tend to produce spurious overshoots and undershoots. Also, general coordinate systems were used to align the grid with the streamlines. However, the computational costs of these approaches are relatively high. In practice, grid refinement has been found to be an effective approach especially since the resulting large memory from the grid

refinement can be solved by faster and larger computers and multi-grid solution techniques which provides enhanced iteration convergence.

5.3. Solution Algorithms

For the nonlinear Navier-Stokes equations, a solution algorithm is needed to solve the coupled continuity and momentum equations. A modified SIMPLER algorithm and Vanka's algorithm are used in the 2D-MGFD and 3D-MGFD codes, respectively and are described in the following sections.

5.3.1. Modified SIMPLER Algorithm

The SIMPLE pressure-correction scheme of Patankar (1980) is a widely used algorithm for fluid flow and heat transfer. In the SIMPLE algorithm, the momentum and continuity equations are solved in a decoupled manner. The momentum equations are solved based on an approximate pressure field and a pressure-correction equation is used to correct the flow and pressure field to satisfy the continuity equation. Although SIMPLE and its revised version SIMPLER have been found satisfactory in most simple calculations, improvements are still needed. First, the pressure-correction equation in SIMPLE is not strictly derived; some bold approximations are made. Second, the coefficients of the pressure-correction equation are very complicated, especially when applied to a general coordinate system.

To overcome these difficulties, a new correction scheme is developed in the present work based on the projection method proposed by Ascher et al. (1994) for higher index differential-algebraic equations (DAEs). At each iteration, the velocities on the control volume surface (see Figure 5.4), which are calculated based upon the pressure field from the previous iteration step, are corrected through a new function ψ

$$\rho U_i^{(new)} = \rho U_i^{(old)} + \left(\frac{\partial \psi}{\partial x} \right)_i, \qquad i = e, w \tag{5.13}$$

$$\rho V_j^{(new)} = \rho V_j^{(old)} + \left(\frac{\partial \psi}{\partial y}\right)_j, \qquad j = n, s \qquad (5.14)$$

so that the new velocity field satisfies the approximate continuity equation.

$$\left[\rho U_e^{(new)} - \rho U_w^{(new)}\right]\Delta y - \left[\rho V_n^{(new)} - \rho V_s^{(new)}\right]\Delta x$$

$$= \rho\left[U_e^{(old)} - U_w^{(old)}\right]\Delta y - \rho\left[V_n^{(old)} - V_s^{(old)}\right]\Delta x + \left[\left(\frac{\partial \psi}{\partial x}\right)_e - \left(\frac{\partial \psi}{\partial x}\right)_w\right]\Delta y + \left[\left(\frac{\partial \psi}{\partial y}\right)_n - \left(\frac{\partial \psi}{\partial y}\right)_s\right]\Delta x$$

$$= 0$$

$$(5.15)$$
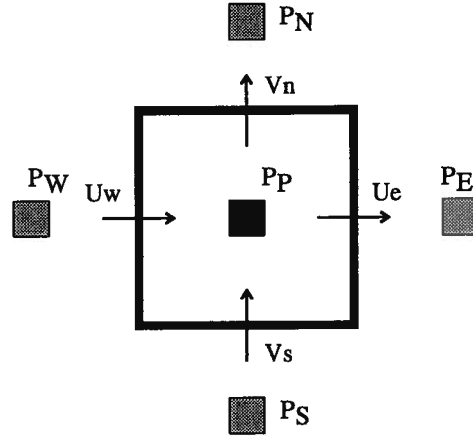
Figure 5.4: Control volume for the continuity equation.

By using the central difference scheme for the derivative term of ψ, an algebraic equation for ψ can be obtained. In the present computations, velocity components normal to all the boundaries (inlet, solid wall, no flux surface, and exit) are imposed, thus no correction is needed. Therefore, there is no need to impose boundary conditions for ψ on the boundaries. After obtaining the solution of ψ, the velocity field can be updated by Equations 5.13 and 5.14.

The correction equation ensures that the flow fields satisfy the constraint of the continuity equation after each iteration. The advantage here is that the coefficients of the difference equation for the correction equation (5.15) only depend on the geometry of the

grid; not on the flow field. Therefore, a simpler formulation and better stability for the correction are obtained.

5.3.2. Vanka's Algorithm

Vanka's algorithm solves the flow field by coupling the velocity and pressure. A brief description of Vanka's solution procedure is presented by considering a single control volume in two space dimensions as shown in Figure 5.4 (details are given by Vanka, 1986):

An equation for the variable U_e can be obtained from the momentum equation in the form of Equation 5.4:

$$a_e U_e = \sum a_{nb}^e U_{nb}^e + b_e + (P_P - P_E)\frac{\Delta y}{\Delta x} \tag{5.16}$$

where U_{nb}^e are the neighbor values for U_e, a_{nb}^e are their coefficients, and $\Delta y, \Delta x$ are the appropriate mesh sizes. Equation (5.16) can be rewritten as:

$$U_e = B_e + (P_P - P_E)C_e \tag{5.17}$$

where $B_e = \left(\sum_{nb} a_{nb}^e U_{nb}^e + b_e\right)\Big/ a_e$ and $C_e = \frac{\Delta y}{\Delta x}\Big/ a_e$. Similarly

$$U_w = B_w + (P_W - P_P)C_w \tag{5.18}$$

$$V_n = B_n + (P_P - P_N)C_n \tag{5.19}$$

Equation (5.19) can be put in the form

$$V_n = \hat{B}_n + C_n P_P \tag{5.20}$$

where $\hat{B}_n = B_n - P_N C_n$. Similarly

$$V_s = \hat{B}_s + C_s P_P \tag{5.21}$$

The continuity equation for the control volume surrounding P_P takes the form

$$D_e U_e - D_w U_w + D_n V_n - D_s V_s = 0 \tag{5.22}$$

with $D = \rho A$ for each control volume face where ρ is the fluid density and A the area of the face. Substituting Equations 5.18-19 and 5.20-21 into Equation 5.22 gives

$$D_e\left[B_e + (P_P - P_E)C_e\right] - D_w\left[B_w + (P_W - P_P)C_w\right]$$
$$+ D_n\left[B_n + (P_P - P_N)C_n\right] - D_s\left[B_s + (P_S - P_P)C_s\right] = 0 \qquad (5.23)$$

which is the same as

$$\alpha P_W + \beta P_P + \gamma P_E = \delta \qquad (5.24)$$

where P_N, P_S are incorporated into δ.

For the i-th cell in a row, Equation (5.24) can be written as

$$\alpha_{i-1} P_{i-1} + \beta_i P_i + \gamma_{i+1} P_{i+1} = \delta_i \qquad \text{for} \qquad i = 1, 2, \ldots, n \qquad (5.25)$$

where $\alpha_i, \beta_i, \gamma_i, \delta_i$ are calculated using the latest values of the flow parameters. This system of equations can be solved with appropriate boundary conditions (details are given by Salcudean et al., 1992 and Nowak, 1991). Then, the velocity components are found from the explicit formulas given by Equations 5.17-5.21. This 'line Vanka' procedure is repeated for all the lines parallel to the three coordinate directions, usually in the 'zebra' fashion: odd-numbered rows of cells go first, followed by the even-numbered rows.

In contrast with the decoupled solution technique used in the simple algorithm, the Vanka scheme solves the momentum and continuity equations with an implicit pressure-velocity coupling and therefore eliminates the need for the pressure-correction equation. The velocities and pressures are simultaneously updated and iterations are made to remove the nonlinearities. It was found that with the Vanka scheme calculations of complex turbulent recirculating and reacting flows have been made in computational times a factor of ten smaller than those required by SIMPLE (Vanka, 1986).

5.4. Multi-Grid Computational Procedure

The iteration method used to solve the discretized nonlinear equations faces slow convergence as an increased number of grid points is used to achieve high flow resolution. The slow convergence of the solution algorithm is generally due to the persistence of low frequency errors that are not effectively removed on a grid which is small relative to the

wave lengths of the errors. In order to remove these low frequency components, a multigrid solution algorithm is used. In this method, relaxation techniques are applied on a hierarchy of grids, so that error components corresponding to a wide range of frequencies are effectively removed (Brandt, 1977).

The basic full multi-grid FAS procedure used in 2D-MGFD can be described by a two-grid system: a coarse grid Ω^H and a fine grid Ω^h (detailed description and the performance of 2D-MGFD are given by Zhou, 1990). The fine grid is obtained by dividing the cells of the coarse grid along each direction by two. Therefore, for a three dimensional domain, the fine grid has eight times the number of cells of the coarse grid. Assuming the discretized system of flow equations on a given grid Ω^h has a form

$$L^h Q^h = F^h \qquad (5.26)$$

the multi-grid procedure is given by

- Step 1. Coarse grid pre-iteration, $L^H Q^H = F^H$:

  The solution q_C^H is obtained by performing $N_{H,1}$ iteration sweeps on Ω^H. It is usually not necessary to obtain a 'fully converged' solution on the coarse grid, as this is used to provide an initial guess for the fine grid computations.

- Step 2. Prolongation from Ω^H to Ω^h, I_H^h:

  The solution q_C^H obtained on Ω^H is prolongated to Ω^h. The prolongation is done by interpolating the solution to the new grid points which lie between the coarse grid points.

- Step 3. Fine-grid iteration, $L^h Q^h = F^h$:

  The solution q^h is obtained by performing $N_{h,1}$ relaxation sweeps on Ω^h with the prologated solution. This relaxation process removes the high frequency components of the error from the solution on Ω^h. $N_{h,1}$ is not a large number since the relaxation on Ω^h can reduce the high frequency components of the error quickly. The residuals $r^h = F^h - L^h q^h$ are calculated on Ω^h. The

residuals r^h contain the low frequency component of the error in the solution. If the solution is fully converged, these residuals are close to zero.

- Step 4. Restriction from Ω^h to Ω^H, I_h^H:

  The residuals are restricted to the coarse grid. The restriction process is also an interpolation, such that the residuals are represented on the coarse grid. At the same time, the solution q^h is also restricted to the coarse grid by the same restriction process.

- Step 5. Coarse-grid correction, $L^H Q^H = I_h^H r^h + L^H \left(I_h^H q^h \right)$:

  The solution q^H to the correction equations is obtained by performing $N_{H,2}$ iteration sweeps on Ω^H. This solution is not expensive to obtain because it is obtained on the coarse grid. The multigrid correction is obtained by subtracting the solution to the correction problem from the restricted solution $v^H = q^H - I_h^H q^h$.

- Step 6. Prolongation of the correction v^H to Ω^h, I_H^h:

  The multigrid correction v^H is prolongated to Ω^h, and then used to correct the fine grid solution $q_{(new)}^h = I_H^h v^H + q^h$. Since the multigrid correction specifically targets the low frequency errors, the residuals are reduced effectively.

- Step 7. Fine-grid post iteration $L^h Q^h = F^h$:

  With the corrected solution $q_{(new)}^h$, $N_{h,2}$ iteration sweeps is performed on Ω^h.

  The multigrid cycle from Step 3 is then repeated.

The multigrid procedure in 3D-MGFD uses a different approach in the coarse-grid correction (Step 5): $L^H Q^H = I_h^H r^h + L^H \left(q_C^H \right)$, where q_C^H is the coarse-grid solution (Nowak, 1991). The coarse-grid solution q_C^H instead of the restricted solution $I_h^H q^h$ used on the right hand side of the correction equation simplifies the programming. It is important to note that for some problems (although not in the present computations) in which the solutions on Ω^h and Ω^H have significant different characteristics, such a multi-grid correction scheme may not improve iteration convergence. This is because unlike the

restricted solution $I_h^H q^h$, the coarse-grid solution q_C^H does not contain flow information on the fine grid.

In the present computations, the convergence criterion which measures the degree to which a computed solution satisfies the finite difference equations (Equation 5.4) on the fine grid Ω^h is based on the normalized absolute residual errors of the equations being solved. These residuals are defined as follows

$$E = \frac{\sum_{i,j,k} \left| (a_P - S_P)\phi_P - \sum a_{nb}\phi_{nb} - S_U^\phi \right|}{F_{in,\phi}}$$

where, for the mass equation, $F_{in,\phi}$ is the total inflow of mass; for the momentum equation, $F_{in,\phi}$ is the total inflow of momentum; and for the scalar equations, $F_{in,\phi}$ is the product of total volumetric inflow and the inlet scalar quantity. The solution is regarded as converged when these normalized absolute residuals become less than a prescribed small value. In this work, the value of $E \le 10^{-5}$ was considered to be acceptable for the flow equations and scalar equations while $E \le 10^{-3}$ for the turbulence equations. A reduction of these values by a factor of 10 did not result in any appreciable change in the computed film cooling effectiveness and flow fields.

Chapter 6

Results I: Two-Dimensional Case

This chapter presents both the experimental and computational results for the 2-D film cooling model. Two alternative turbulence models, the multiple-time-scale k-ε model (MTS) and the standard k-ε model (KE), were used combined with two near-wall treatments, the low-Re k model (KE&LK in short) and the standard wall function (KE&WF in short). Comparison between experiments and computations are described by distributions of 1) film cooling effectiveness, 2) mean flow velocity and turbulent kinetic energy, and 3) coolant distribution on the vertical streamwise plane downstream of injection. These quantities indicate the shear in the mean flow, turbulent mixing of the mainstream and coolant, and also film cooling performance. Although the 2-D computation is not our primary objective, it is necessary to investigate the proposed turbulence modelling methods in the 2-D case since most of the turbulence models were developed for 2-D flows. Further improvement towards more general turbulence modelling is suggested as a result of the present work.

In the following sections, the computational domain and boundary condition treatments are described. The grid independence of the present computation and the false diffusion involved in the numerical discretization are discussed.

6.1. Computational Domain and Boundary Conditions

The computational domain for the 2-D model is shown in Figure 6.1. The treatment of boundary conditions on each side can be described as follows:

- Mainstream:

  The upstream boundary was located at a distance $X/d=10$ from the injection orifice, where the experimental values of mean velocity and turbulence intensity were

measured. The mean velocity and turbulent kinetic energy k profiles were tuned to match the measurements closely. It has been found that the downstream effectiveness values are sensitive to the upstream conditions. Proper comparisons with the experimental results must include these well-defined inlet conditions.

Within the boundary layer, the streamwise mean velocity distribution was obtained from the logarithmic law (Equation 3.4) in the fully turbulent region and the linear law

$$\frac{U}{U_\tau} = y^+ \tag{6.1}$$

in the laminar sublayer region. The turbulent kinetic energy was linearly interpolated from the measured fluctuating velocity based on the isotropic assumption

$$k = \frac{3}{2}\overline{u'^2} \tag{6.2}$$

The other mean velocity components were assumed as

$$V = 0; \qquad W = 0 \tag{6.3}$$

The inlet condition for the dissipation rate of ε was prescribed based on the formulations described by Yap (1988):

$$\varepsilon = C_\mu k^2 \left(l^2 \frac{dU}{dy} \right)^{-1} \tag{6.3}$$

where $l = \min(\kappa y, 0.09\delta)$, y is the distance from the wall and the von Karman constant $\kappa = 0.4$.

In the mainstream flow at the inlet, the following expressions were used

$$U = U_\infty; \qquad V = 0; \qquad W = 0 \tag{6.4}$$

$$k = 1.5(iU_\infty)^2 \tag{6.5}$$

$$\varepsilon = C_\mu^{3/4} k^{3/2} / L \tag{6.6}$$

where $i = \sqrt{\overline{u'^2}} / U_\infty$ is the mainstream turbulence intensity which is 0.5% as measured in the experiment. The length scale was given as the height of inlet domain, *L=30d.*

In the calculation with M-T-S, an arbitrary ratio of $k_t / k_p = 4$ was used as an inlet boundary condition. A change of this ratio from *1* to *20* did not have a noticable effect on the turbulence field downstream.

- Injection:

Uniform injection velocity, turbulent kinetic energy and energy dissipation were imposed at the inlet of the injection slot.

$$k_J = 1.5 i_J^2 V_J^2, \qquad \varepsilon_J = C_\mu^{3/4} k_J^{3/2} / d \qquad (6.7)$$

where V_J is the mean injection flow velocity, the injection jet turbulence intensity $i_J = (v' / V)_J$ is specified as 5%, and *d* is the slot width.

- Outlet Condition:

The zero gradient condition was applied at the outlet boundary, which is located downstream at *X/d=40*. It was sufficiently far downstream to ensure that the flow in the upstream region was not affected by downstream conditions.

- Axis of Symmetry:

The top boundary was treated as a no-flux boundary, where a zero gradient across the boundary was imposed on all variables. No effect was found for any further extension.

- Adiabatic Wall:

At the bottom wall, zero normal and tangential velocities as well as zero heat flux were imposed. Two alternate treatments of the turbulence were used near the wall: the wall function and the low-Re k model.

6.2. Numerical Grid and Effect of Grid Refinement

Preliminary runs were made to determine the effect of grid refinement and to monitor the numerical false diffusion involved in the computations. Four progressively refined grids

were used for computations at $R_M = 0.4$. The computations were carried out using a combination of the standard k-ε model with the low-Re k model (KE&LK).

To refine the grid near the slot and the solid walls, a uniform grid was used in the X-direction across the slot and exponential expanding grids were used to avoid unnecessary use of fine grids in the region away from the injection. The grid expansion ratios used in the X-direction upstream and downstream of the slot were 1.12 and 1.06 respectively. The grid expansion ratio used in the y-direction above the adiabatic wall was 1.06. The grid expansion ratio used in the y-direction under the wall in the slot was 1.2. Table 6.1 shows the four progressively refined grids with the grid size within the slot and that of the first node next to the wall, as well as the overall number of grid points. A typical numerical grid (Grid 3) is shown in Figure 6.2.

Table 6.1: Arrangement of four progressively refined grids.

	Grid 1	Grid 2	Grid 3	Grid 4
Δx within the slot	d/4	d/8	d/12	d/16
Δy next to the wall	d/16	d/32	d/48	d/64
Grid Points	58×66	74×78	90×86	106×94

Figure 6.3 shows the predicted mean velocity distributions at the exit of the slot using the four progressively refined grids. The nonuniformity of the injected slot flow is clearly presented, which shows that the injection jet is compressed by the upstream boundary layer and is concentrated near the downstream exit. The finer grid tends to give sharper variation and higher maximum velocity values. Very little difference is found between Grids 3 and 4.

Figure 6.4 gives the predicted mean velocity and turbulent kinetic energy at the location *X/d=3* downstream of the slot. Identical mean velocity distributions are achieved

in the cases of Grid 3 and Grid 4, and the overall discrepancy among the four grids is relatively small. For the turbulent kinetic energy, the finer grid tends to give higher values. This indicates that the coarse grid generally 'smears out' the turbulence generation, thus underpredicting the resulting turbulent kinetic energy. No further difference is found beyond Grid 3. Figure 6.5 gives the film cooling effectiveness distributions by the four grids. Again, the grid independence of effectiveness is achieved by Grid 3.

Figure 6.6 shows the distribution of the false diffusion coefficient by Grid 3, which is estimated by Equation 5.10. The coefficients have values greater than unity near the slot orifices. From this preliminary test, it is shown that Grid 3 is a reasonable grid for later computations.

For the computations with wall function (WF) treatment, the first node next to the wall was located at $Y\!/_{\!d} = \dfrac{1}{10}$, which corresponds to $y^+ = 20 - 40$ for the present computations in the range $R_M = 0.2 - 0.8$. The use of the coarse grid near the wall resulted in high false diffusion, especially near the injection location.

A three-level multi-grid iteration was used in the computations. The iteration parameters used in the 2D-MGFD code are listed in Table 6.2. Typical convergence performance for the computations at $R_M = 0.4$ with all the turbulence model options is shown in Figure 6.7. Numerical instability was observed in the computations using the M-T-S model, so 5 iteration sweeps were added for the turbulence equations in each smoothing cycle. Computations using the k-ε model and WF treatment (KE&WF) have the best iteration performance. The multi-grid convergence rate deteriorated for computations using the fine grid low-Re k model (LK) since more nodal points were used than in the computations using the WF treatment. These results apply in general for 2-D for various R_M. For the present nonlinear system of governing equations, reasonable iteration convergence was obtained although the convergence rate was sensitive to the number of grid points.

Table 6.2: Multi-grid parameters in the 2D-MGFD code.

Description	Number of Smoothings	Under-relaxation Factor
Solution on the coarsest grid	10	0.8
Correction on coarse grid	5	0.8
Pre-Solution on the finest grid	5	0.8
Post-Solution on the finest grid	5	0.8
Multi-grid steps for solution on the finer grid	30 ~ 40	N/A

6.3. Predictions and Comparison with Experimental Data

Computations were carried out using the standard k-ε model and the M-T-S model with two near-wall turbulence treatments: the standard wall function (WF) and the low-Re k model with refined grid (LK). The computed film cooling effectiveness and velocity profiles are compared with the experiments.

6.3.1. Mean Velocity

Figures 6.8 and 6.9 show a comparison between the computed mean velocity distributions and the measured data at mass flow ratios of $R_M = 0.2$ and 0.4, respectively. The mean velocity is normalized by the mainstream velocity, which is $U_m = 10\,\text{m/s}$ in the present case.

Generally, all the options provide fairly good predictions of the mean velocity for the upstream boundary layer flow ($X/d=-3$). After the injection, the coolant separates and a recirculation zone is formed immediately downstream of the slot orifice. Typical predicted vector fields using the M-T-S model with the LK treatment are shown in Figure 6.10. The computed reattachment lengths are compared with those observed as shown in

Table 6.3. Recognizing the uncertainties involved in the experimental observations, this comparison gives a rough indication of the accuracy of the prediction of the wall shear stress. The computations using the WF treatment did not find a separation bubble for $R_M = 0.2$ since a coarse grid had to be used near the wall while the refined-grid computations using the LK treatment gave satisfactory agreement. By examining the reattachment length, it is found that the WF computations tend to over predict the reattachment length at $R_M = 0.4, 0.6$. Apparently, this is because the coarse grid cannot give a good representation of the separation bubble.

Table 6.3: Comparison of reattachment lengths.

	$R_M = 0.2$	$R_M = 0.4$	$R_M = 0.6$
Experiment	0.5 - 1.0	2.0 - 3.0	4.5 - 5.5
MTS with LK	1.56	2.56	4.81
MTS with WF	< grid cell size	5.98	9.01
k-ε with LK	1.69	2.81	5.3
k-ε with WF	< grid cell size	10.9	16.0

After the injection at $X/d=3$, all the options underestimate the velocity gradient near the wall, although the LK treatment gives relatively larger velocity gradients than the WF treatment. However, better agreement is found further downstream. At $X/d=10$ the prediction using the LK treatment recovers and agrees reasonably well with experiments, but the prediction using the WF treatment is not good. At $X/d=20$ fair agreement is found in all options and the best agreement is found using the M-T-S model with the LK treatment.

6.3.2. Turbulent Kinetic Energy

Figures 6.11 and 6.12 compare the computed turbulent kinetic energy with the experimental measurements at $R_M = 0.2, 0.4$ respectively. The turbulent kinetic energy k in the experiment is calculated from the measured turbulence intensity $\sqrt{\overline{(u')^2}}$. In considering the nonisotropic turbulence near the wall, an expression for k ($k = 1.1\overline{(u')^2}$) is used in the present work, which best fits Equation 4.18. The turbulent kinetic energy is normalized by the mainstream velocity $U_m = 10 \, \text{m/s}$.

Reasonable agreement with experiments is found for all treatments upstream of the slot at *X/d=-3*. Downstream of the slot, both turbulence models with the WF treatment show consistent underprediction of turbulent kinetic energy and this underestimation is significant for $R_M = 0.4$. With the LK treatment, the turbulent kinetic energy predicted by both turbulence models agree reasonably well with measured values in magnitude. However, they fail to predict the high peak of turbulent kinetic energy near the wall. This failure could be caused by inadequate treatment of the turbulence in the separation bubble as well as unsteady phenomena which are not captured by the steady-state model. Further downstream at *X/d=10*, agreement between the LK treatment and observations is excellent whereas the WF treatment severely underestimates the turbulent kinetic energy. Within the boundary layer, the M-T-S model generally gives higher turbulence than the k-ε model. At *X/d=20*, reasonable agreement is obtained with all options except the k-ε model with the WF treatment. The best agreement is found using the M-T-S model with LK treatment. Turbulent kinetic energy is underpredicted by k-ε/LK. The improvement with the M-T-S model is significant at the higher mass flow rate $R_M = 0.4$, which indicates the necessity of the non-equilibrium turbulence assumption.

6.3.3. Film Cooling Effectiveness

Figure 6.13 shows a comparison of the measured and computed film cooling effectiveness at $R_M = 0.2, 0.4, 0.6$. Detailed concentration distributions on the streamwise vertical plane at $R_M = 0.2, 0.4$ are also shown in Figures 6.14 and 6.15.

At the low mass flow ratio $R_M = 0.2$, the WF treatment underpredicts the effectiveness just after the injection because of the poor resolution and the false diffusion, as demonstrated by the fact that the effectiveness never reaches unity. Downstream of injection, both turbulence models with the LK treatment give good agreement with the experiments. In the recovery region, the best agreement is obtained by M-T-S/LK. However, both turbulence models with the WF treatment consistently overpredict the effectiveness because of the poor representation of the separation region and the underpredicted turbulence. Hence the mixing is overpredicted due to the coarse grid.

As the mass flow ratio increases to $R_M = 0.4$, M-T-S/LK gives the best overall agreement with the measured effectiveness; however, the agreement deteriorates downstream and only the rate of change of effectiveness with downstream distance is predicted well in the recovery region. As the mass flow rate is further increased to $R_M = 0.6$, the slope of effectiveness shows that M-T-S/LK predicts the measured values very well in the recovery region. However, it is clear that the mixing near the slot is underpredicted because of the inadequate representation of the turbulence in the separation region. The representation of the turbulence length scale near the slot, the unsteadiness of reattachment, and the existence of secondary flow are poorly captured by the present turbulence models. It is expected that the agreement between computations and experiments will deteriorate further with increasing mass flow ratio.

An attempt was made in the 2D-MGFD code to use the algebraic Reynolds stress model of Launder et al. (1975) together with the k-ε model. However, the direct iterative method used in the present work for solving the algebraic equations for the Reynolds

stresses failed to provide a converged solution (see Appendix D for details). The performance of the algebraic Reynolds stress model needs to be investigated.

It is interesting to note that the WF treatment predicts a sudden drop in effectiveness near the slot, which is observed at $R_M = 0.4$ and which is more pronounced at $R_M = 0.6$. This is probably due to the overprediction of the separation bubble and jet penetration resulting from the underpredicted turbulence mixing with the coarse grid arrangement, which can be shown clearly by the concentration distributions in Figures 6.14 and 6.15.
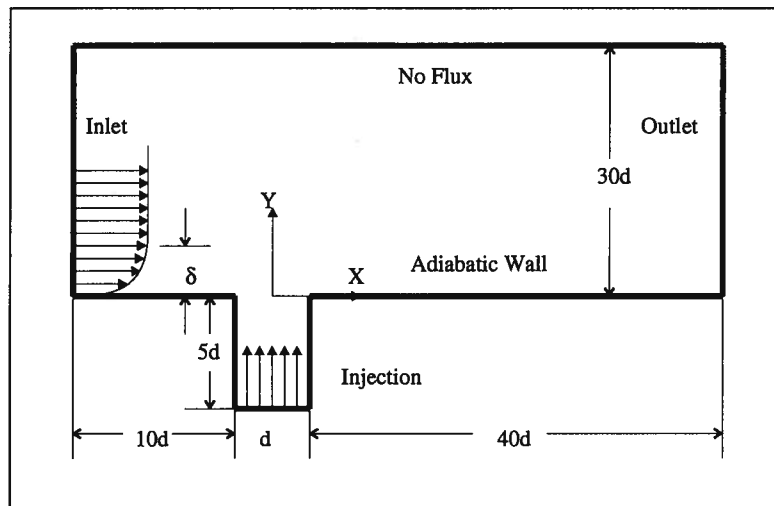
Figure 6.1: Computational domain for 2-D computations.
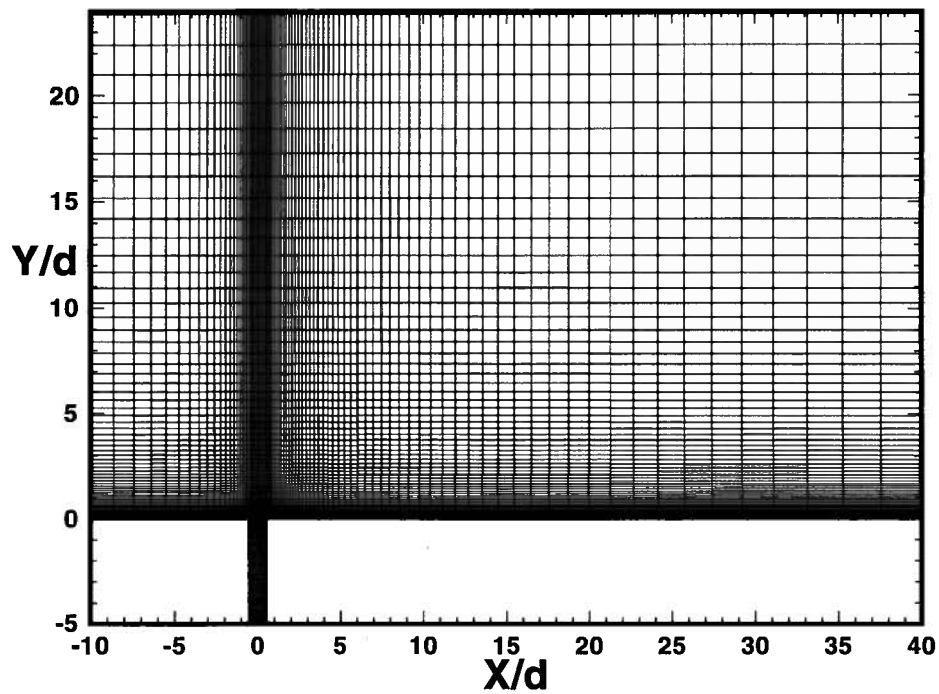
Figure 6.2: Typical grid arrangement for 2-D computations (Grid 3).
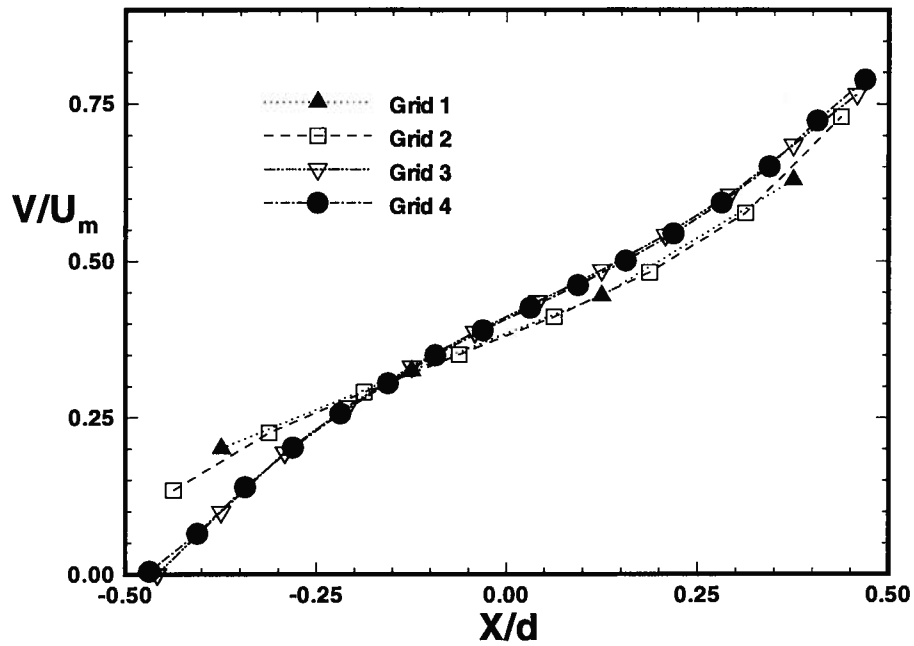
Figure 6.3: Predicted 2-D vertical velocity distribution at the slot exit (KE&LK, $R_M = 0.4$).
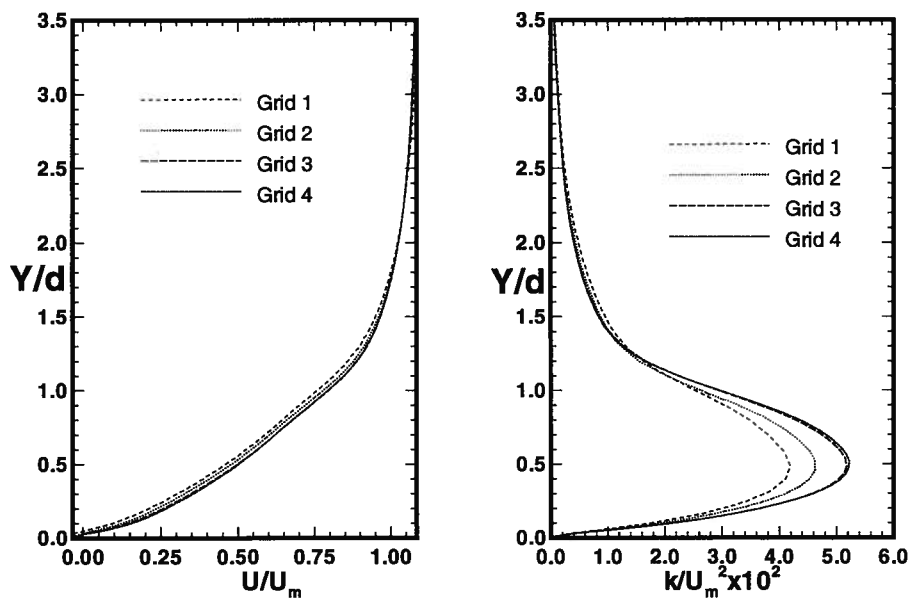
Figure 6.4: Mean velocity and turbulence kinetic energy downstream of injection ($X/d = 3$) predicted by four progressive refined grids (KE&LK, $R_M = 0.4$, 2-D model).
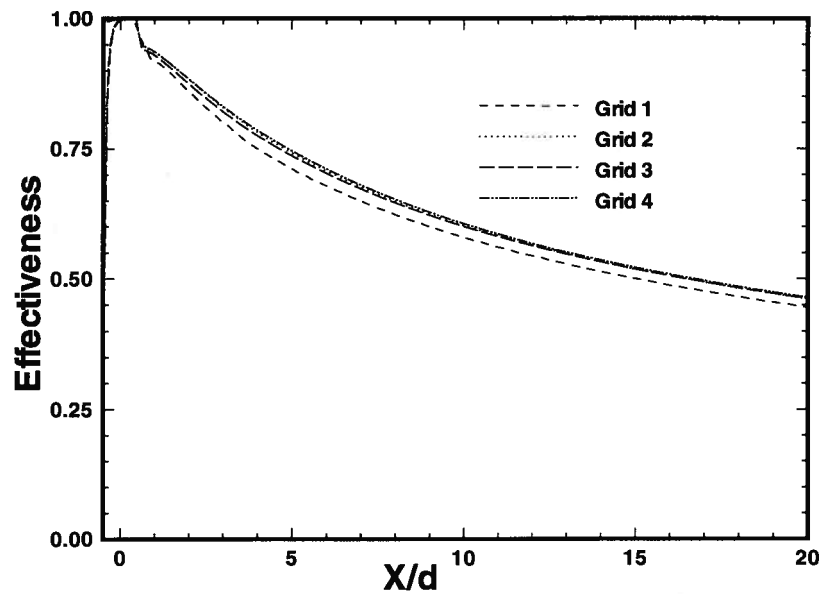
Figure 6.5: Film cooling effectiveness predicted by four progressive refined grids
(KE&LK, $R_{M} = 0.4$, 2-D model)
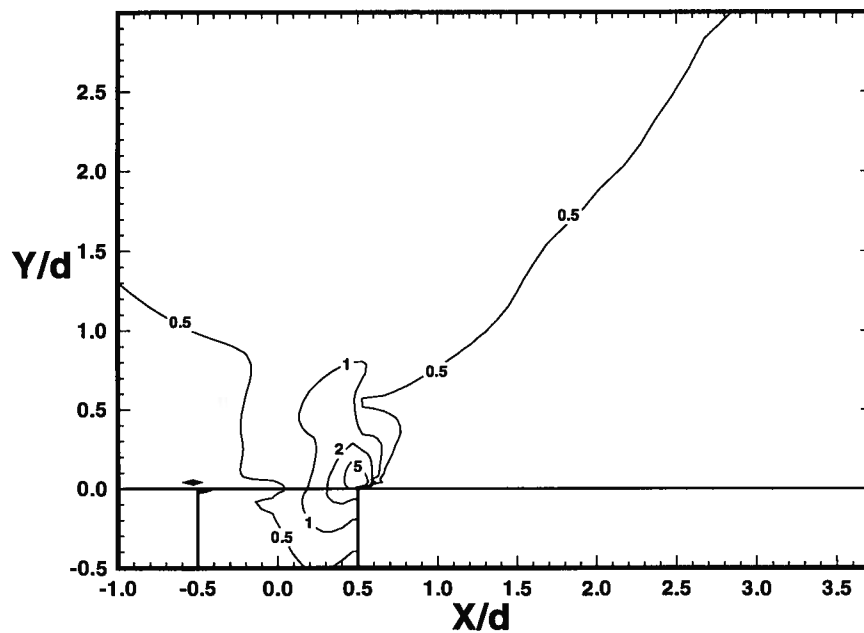
Figure 6.6: Estimated false diffusion coefficient for Grid 3 (KE&LK, $R_M = 0.4$, the estimated values are indicated on the contours, 2-D model).
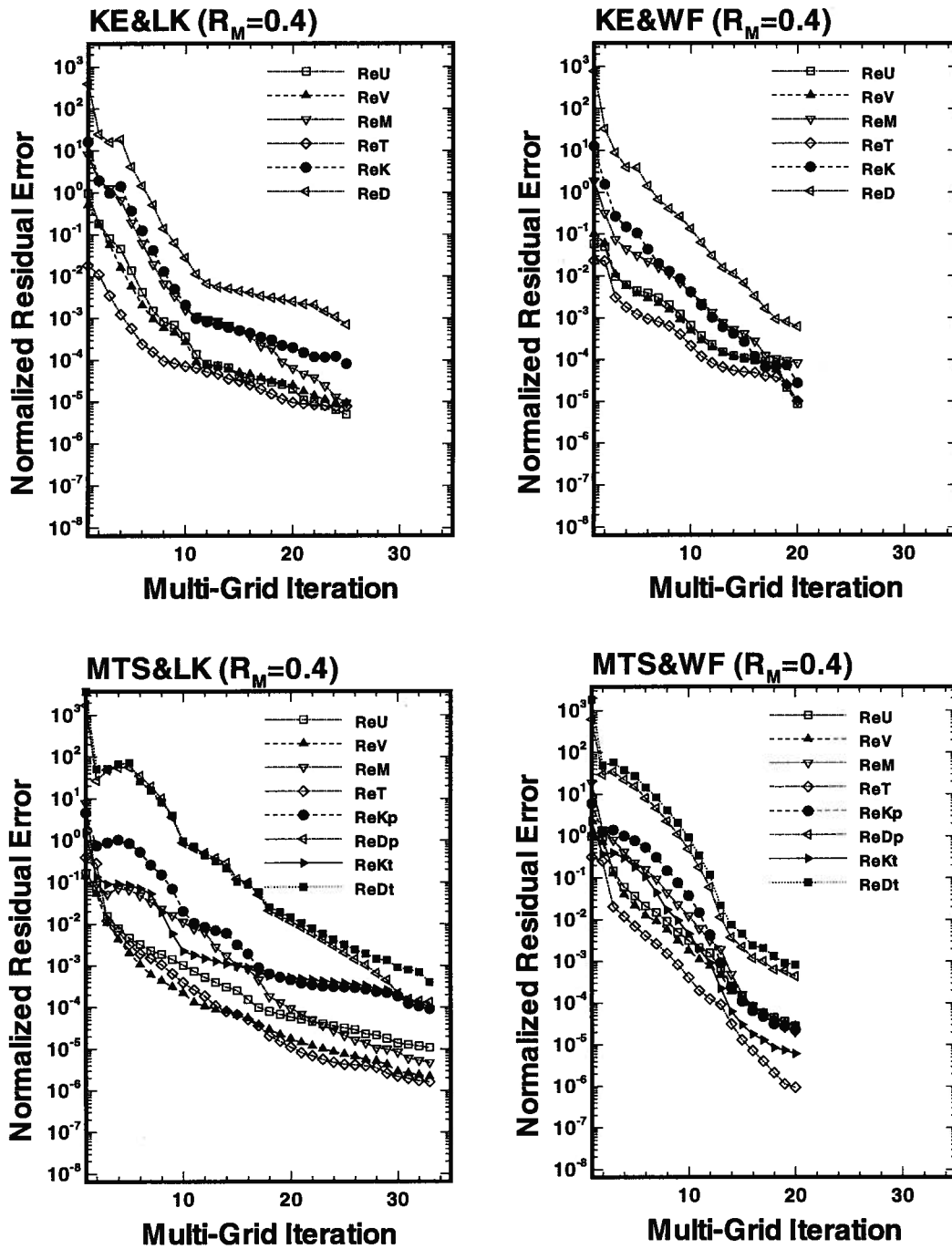
Figure 6.7: Typical 2D-MGFD multi-grid iteration convergence performance ($R_M = 0.4$).
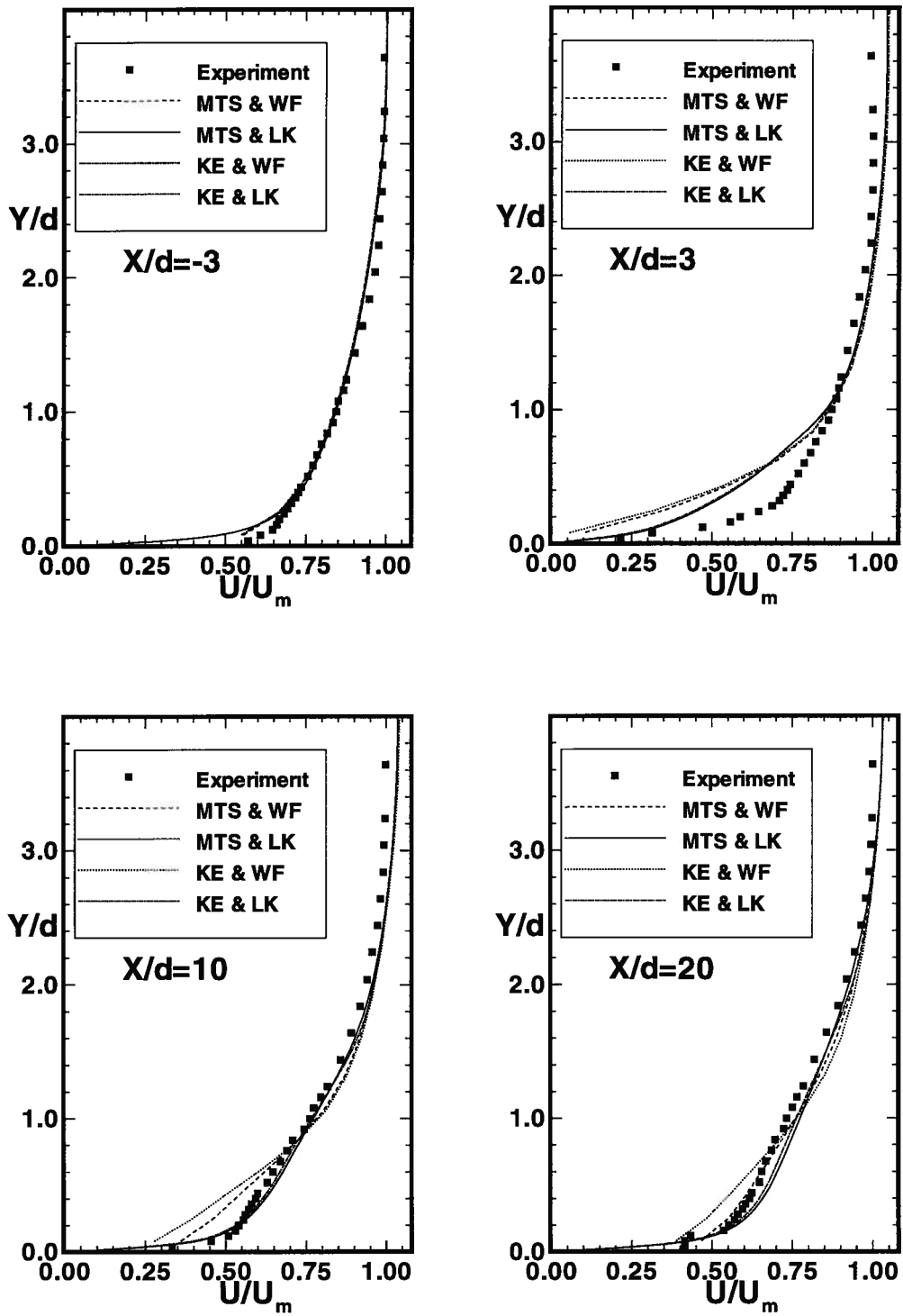
Figure 6.8: 2-D mean velocity distribution ($R_M = 0.2$).
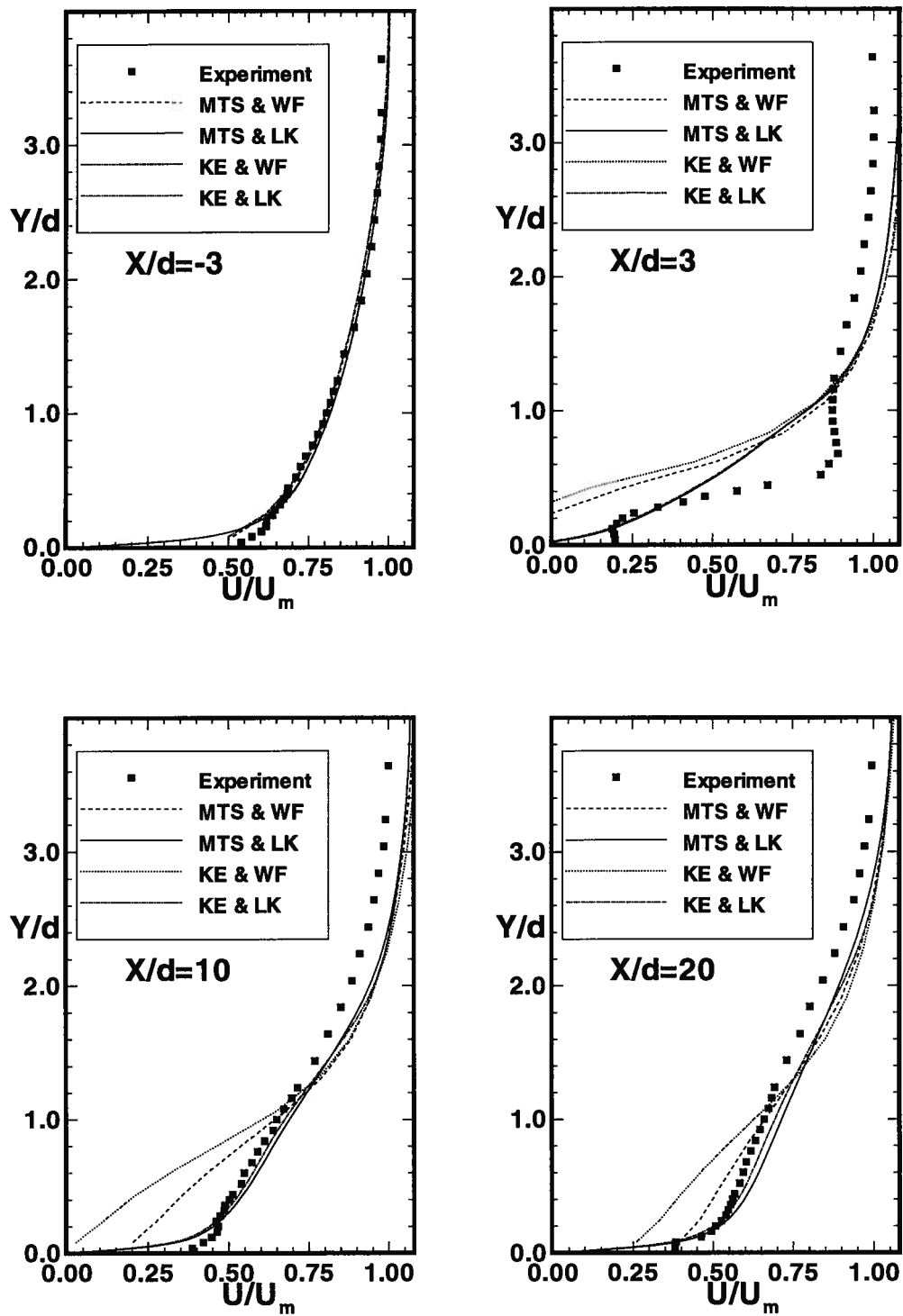
Figure 6.9: 2-D mean velocity distribution ($R_M = 0.4$).

MTS&LK (R$_M$=0.2)

10m/s

MTS&LK (R$_M$=0.4)

10m/s

MTS&LK (R$_M$=0.6)

10m/s
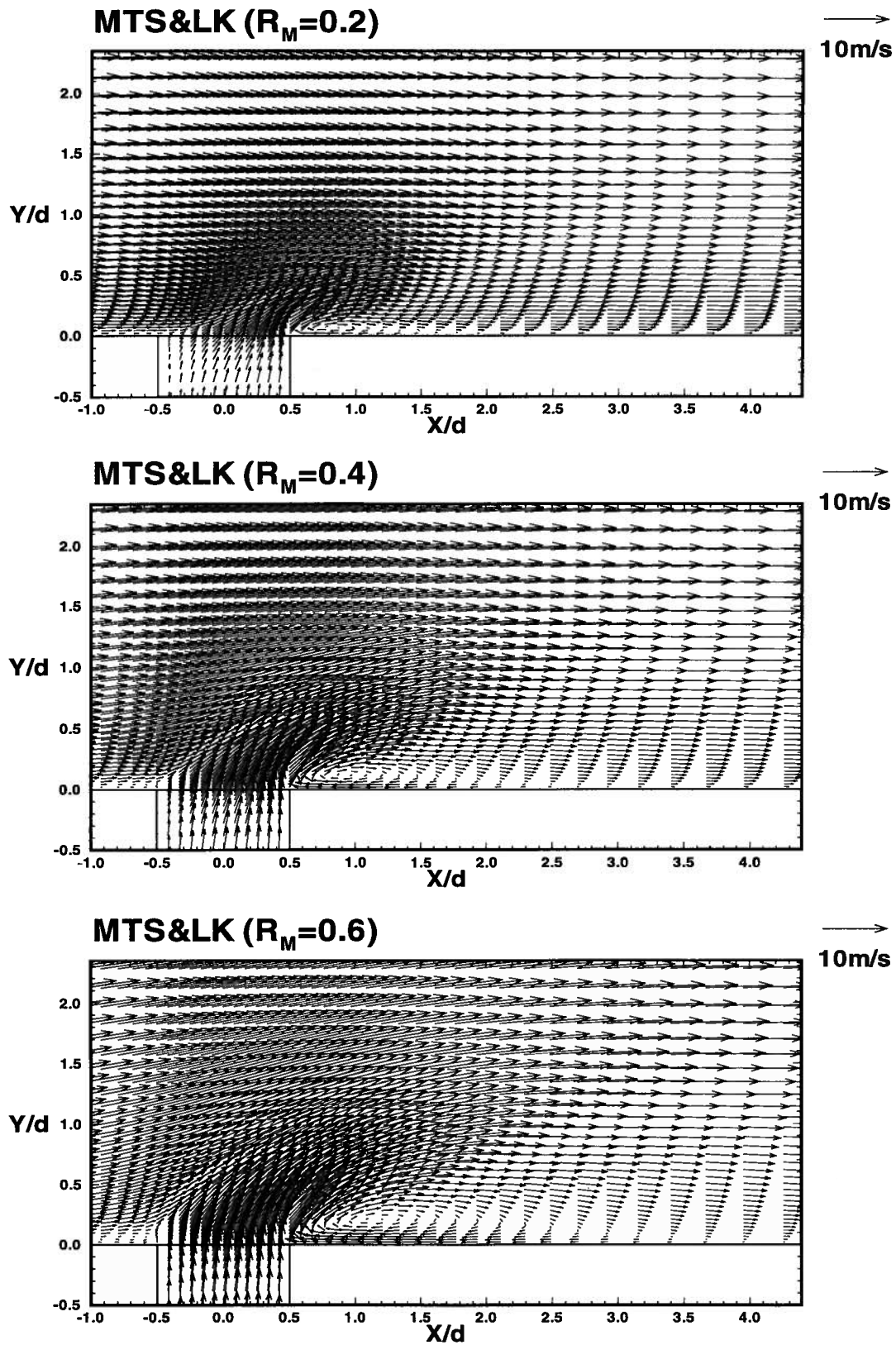
Figure 6.10: Predicted Vector fields by the 2-D MTS/LK model ($R_M = 0.2, 0.4, 0.6$).
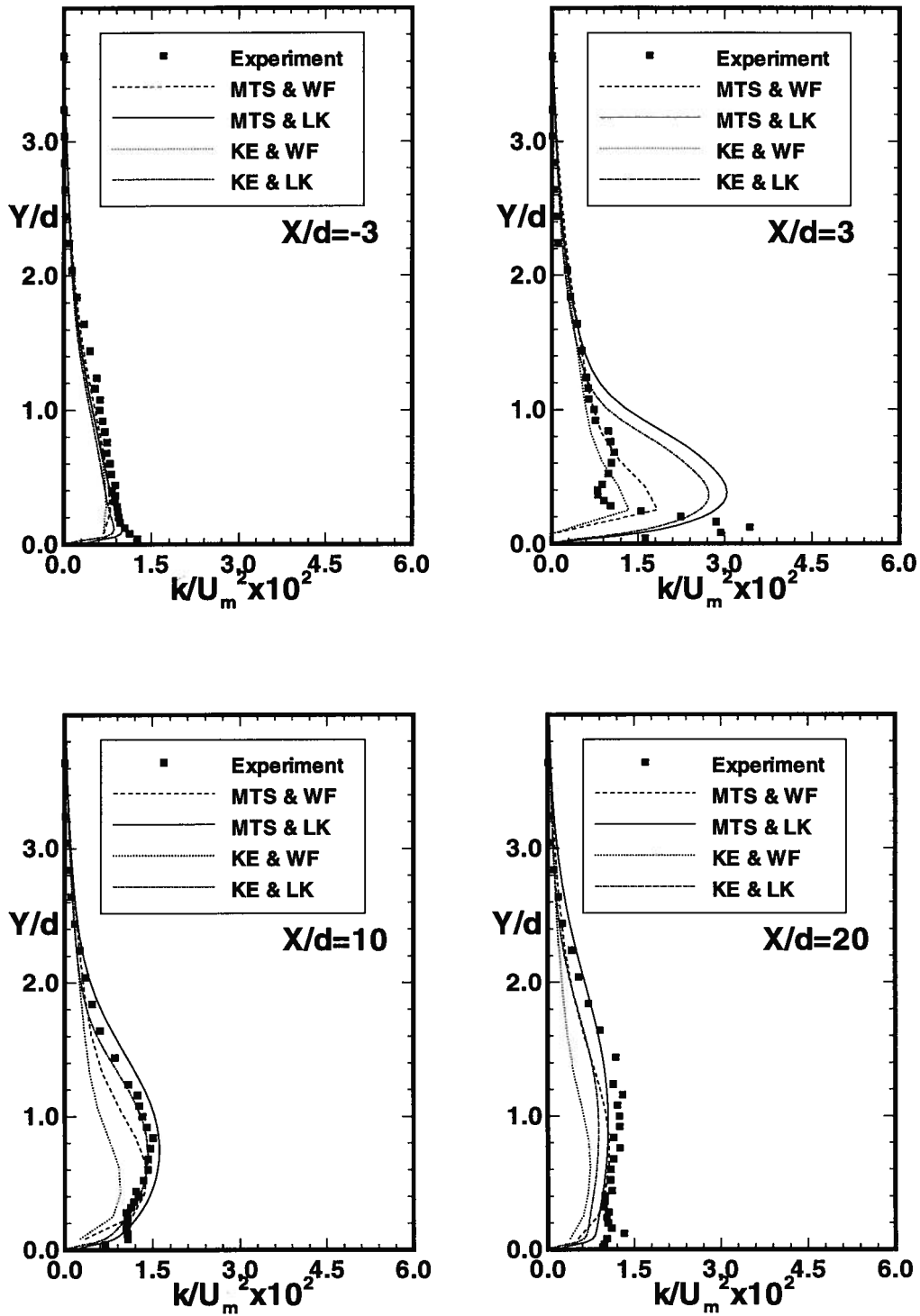
Figure 6.11: 2-D turbulent kinetic energy distributions ($R_M = 0.2$).
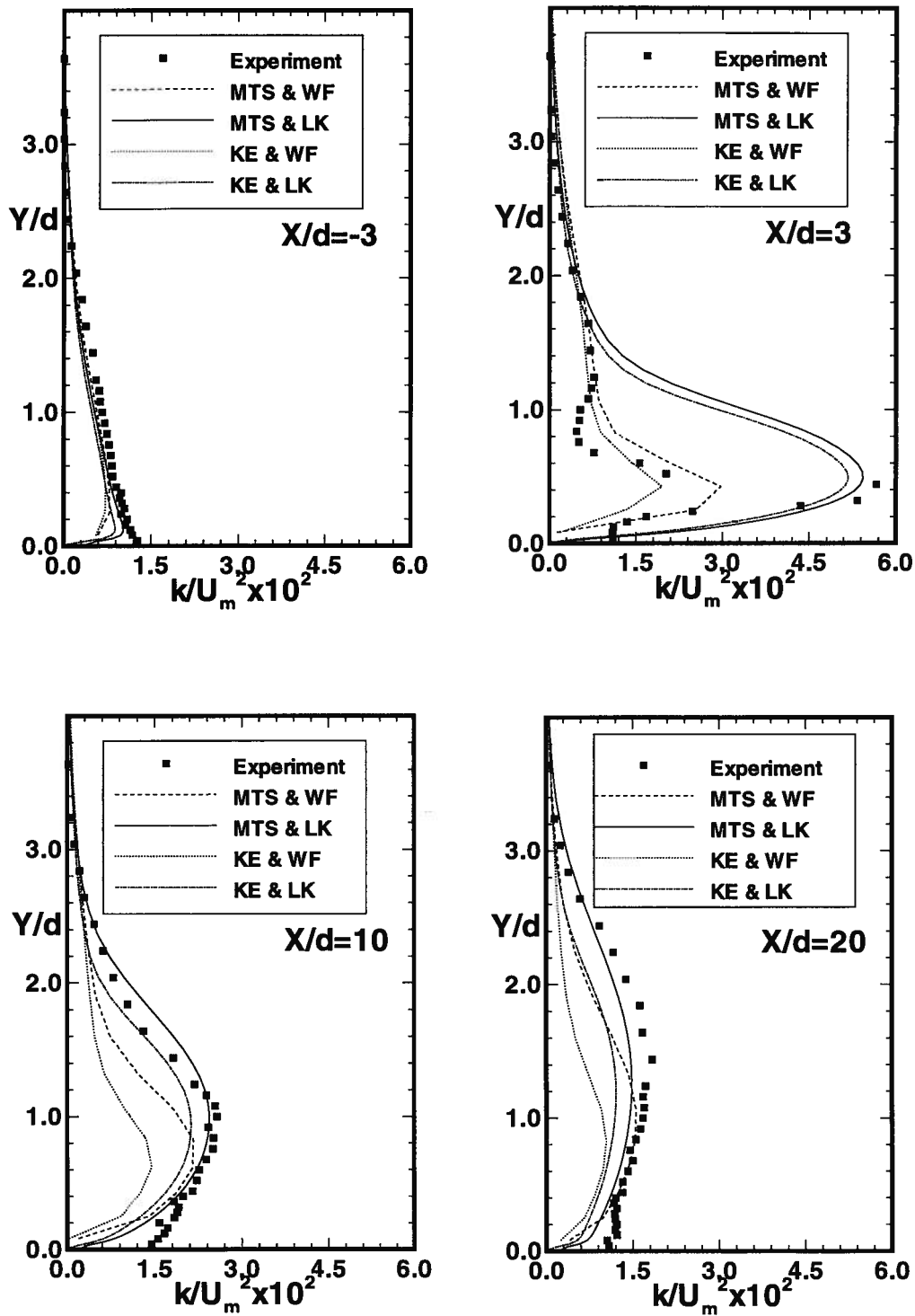
Figure 6.12: 2-D turbulent kinetic energy distributions ($R_M = 0.4$).
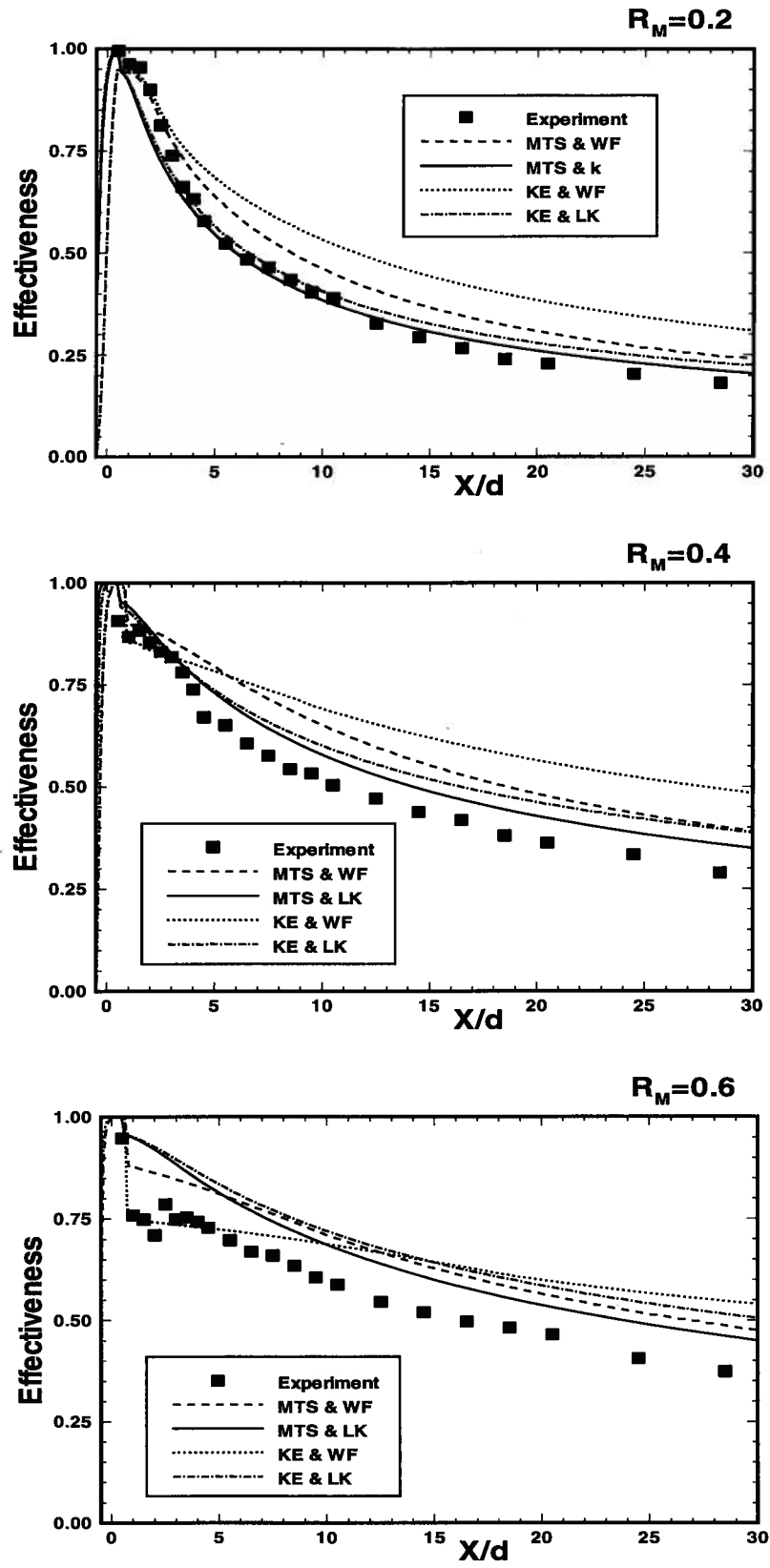
Figure 6.13: 2-D film cooling effectiveness ($R_M = 0.2, 0.4, 0.6$).
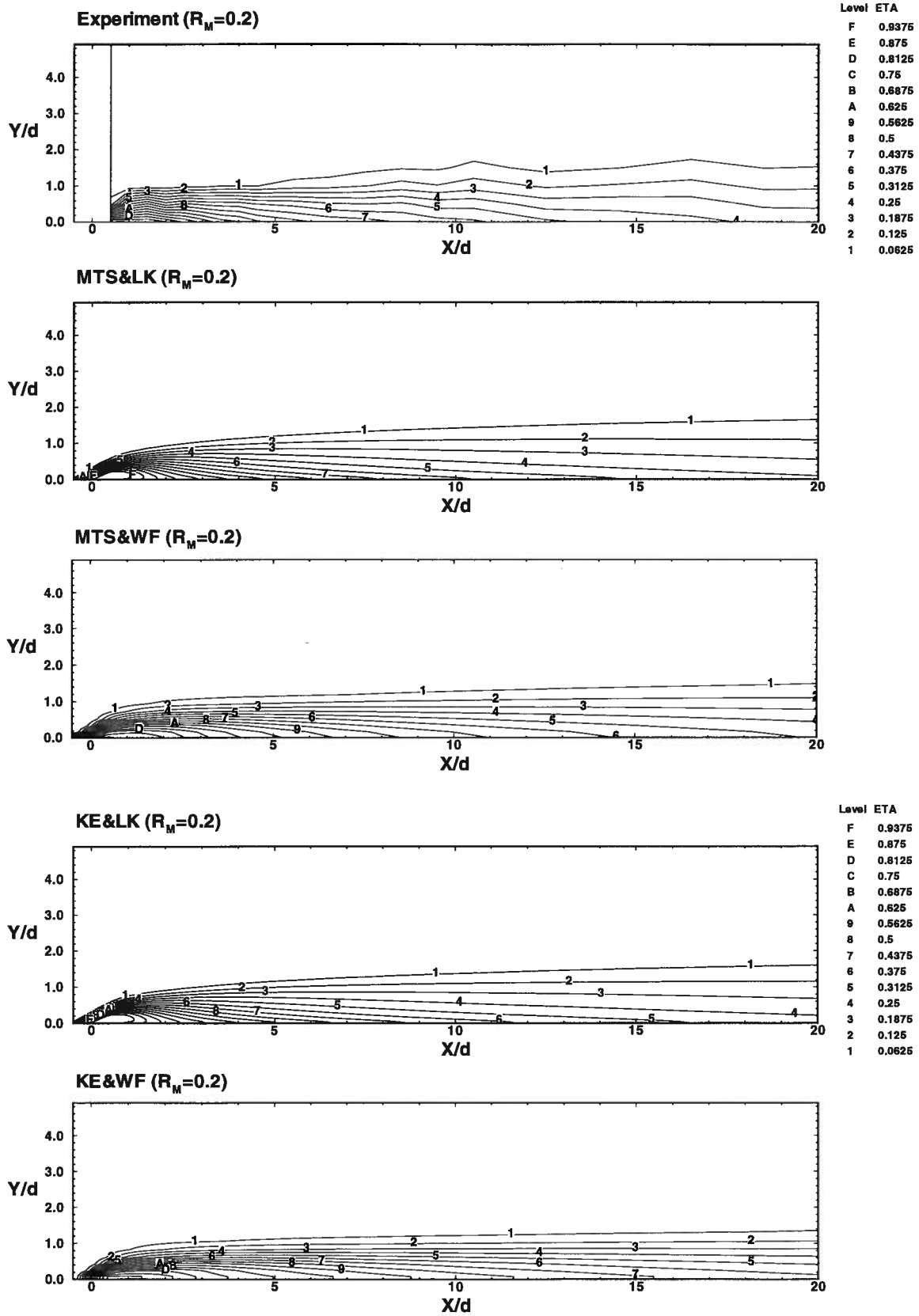
Figure 6.14: 2-D Concentration distribution on the vertical streamwise plane ($R_M = 0.2$).
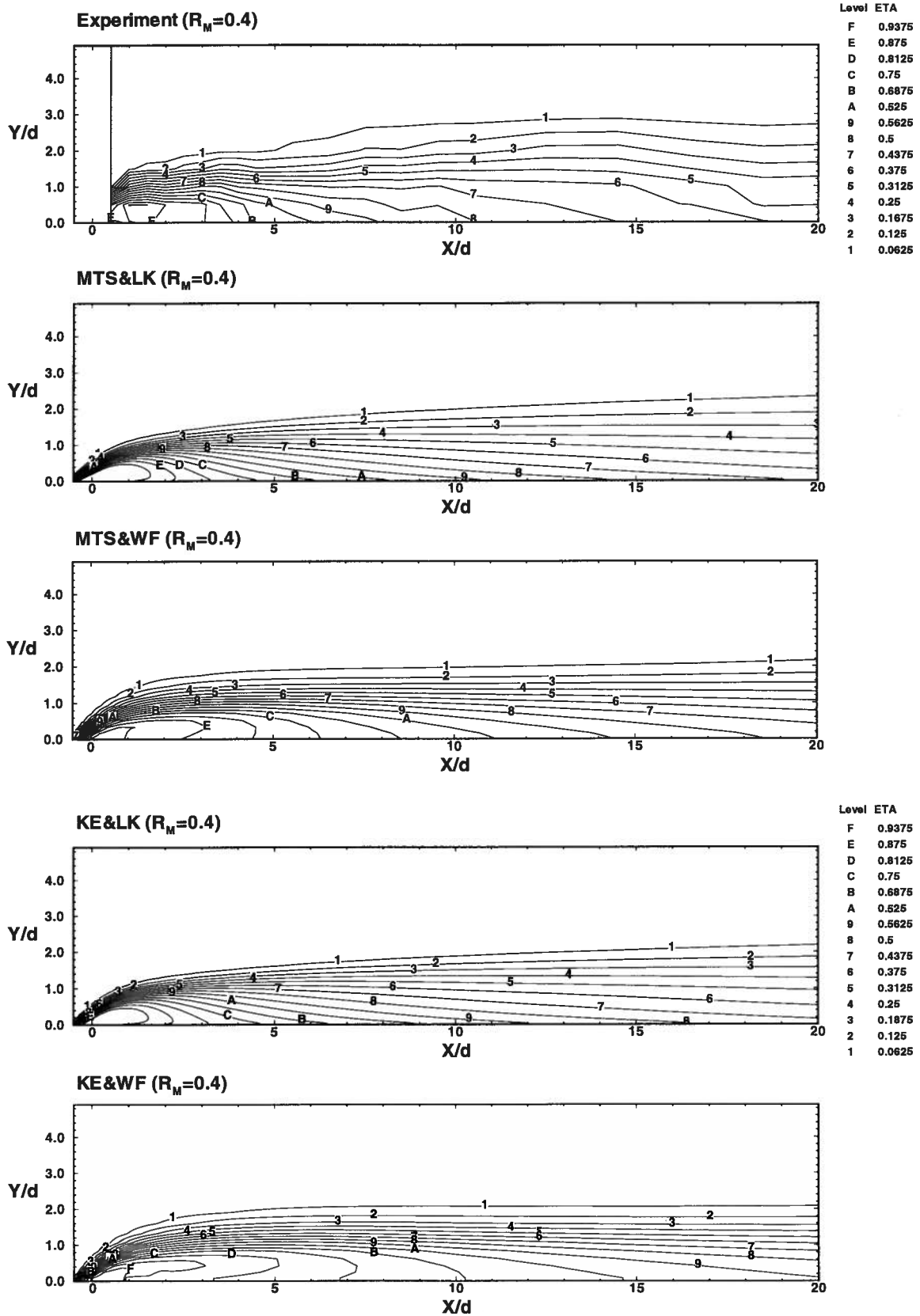
Figure 6.15: 2-D Concentration distribution on the vertical streamwise plane ($R_M = 0.4$).

Chapter 7
Results II: Three-Dimensional Case

This chapter presents the measured and computed results of film cooling effectiveness and flow field for the simplified geometry of vertical injection with square holes. This simplified geometry produces a flow with many of the characteristics of actual film cooling; however, no direct application of numerical results to actual turbines is implied. The present numerical model uses the simplified nonisotropic k-ε model with the near-wall treatment of the low-Re k model (KE&LK). The improvement of the present model over the original 3D-MGFD code, which uses the standard k-ε model and the standard wall function (KE&WF), is shown by comparing the computed and measured cooling effectiveness, mean velocity, and turbulent kinetic energy. The computational domain and boundary condition treatments are described. The grid independence of the present computation are discussed.

The present numerical model was applied to investigate the effect of different parameters, namely mass flow ratio, hole spacing, and hole stagger on film cooling effectiveness with double-row injection. In the present computations, the results for inclined injection cases were obtained using a prescribed velocity imposed at the slot exit which is inclined uniformly in the slot direction. It is believed that realistic trends are represented by these parametric studies, which are intended primarily as illustrations of the insight one can obtain through numerical computations. The observations are strictly valid only for the range of parameters investigated.

7.1. Predictions and Comparison with Experimental Data

7.1.1. Computational Domain and Grid Arrangement

Figure 7.1 shows the computational domain and the boundary conditions for the present 3-D computations. The problem shown consists of an infinite number of holes in the spanwise direction. Because of symmetry on the vertical streamwise planes between holes, the computational domain is reduced to the region between two neighboring symmetric planes and the symmetry conditions are imposed on these two planes. The boundary condition treatments for inlet, outlet, top wall, and the adiabatic wall are the same as those discussed in the 2-D case in Section 6.2.

The grid independence of the numerical model is determined using four progressively refined grids. These grids were selected based on the grid independence tests in the 2-D case discussed in Section 6.3. Grids 1 through 4 introduced in the 2-D case were used in the X- and Y-directions and uniform square grid cells are used over the injection hole and in the Z-direction (see Figure 7.1 for detailed description of the coordinate system). Computations using the LK treatment were carried out for the four grids at $R_M = 0.4$.

Figure 7.2 shows the predicted vertical mean velocity distribution along the streamwise center line at the exit of the injection hole. It is shown that a refined grid gives increased peak velocity and therefore an increased penetration of injected coolant. The profiles predicted by Grid 3 and Grid 4 are nearly identical. Figure 7.3 shows the predicted mean velocity and turbulent kinetic energy downstream of the injection at *X/d=3* on the plane *Z/d=0*. The mean velocities predicted by Grid 3 and Grid 4 reach good agreement with each other, although the turbulent kinetic energy predicted by Grid 4 is slightly higher than that predicted by Grid 3. However, such slight differences do not affect the predicted values of effectiveness using Grid 3 or 4 as shown in Figure 7.4. .

The cross-streamwise false diffusion resulting from the use of Grid 3 was computed based on Equations 5.10-5.12. It was found that the projected component of

the false diffusion coefficient on the *X-Y* plane has relatively higher values than the projected components on other planes. Figures 7.5 and 7.6 show the false diffusion coefficient distributions on the *X-Y* plane at *Z=0* and the *Y-Z* plane at *X/d=0.5*. Overall, coefficients greater than unity are generally located near the injection exit. Since it was found that further refinement gives identical results in terms of film cooling effectiveness, Grid 3 was chosen for later computations

A two-level multi-grid iteration was used in the computations. The iteration parameters used in the 3D-MGFD code is listed in Table 7.1. Typical convergence performance for both near-wall treatments is shown in Figure 7.7. The multi-grid convergence rate deteriorates for computations using the LK treatment with refined grid. This is due partly to two factors: 1) In the 3D-MGFD code, on the coarse grid correction level the restriction of the finer grid solution was not used. Instead the original converged coarse grid solution was used. This formulation prohibits the transfer of information on the finer grid to the coarse grid, and 2) A refined grid was used near the solid wall. For this nonlinear system, the convergence rate is sensitive to the number of grid points deteriorating with an increasing number of grid points.

Table 7.1: Multi-grid parameters in the 3D-MGFD code.

Description	Number of Smoothing	Under-relaxation Factor
Solution on the coarser grid	500	0.6
Correction on the coarser grid	10	0.6
Pre-Solution on the finer grid	5	0.6
Post-Solution on the finer grid	5	0.6
Multi-grid steps for solution on the finer grid	30 ~ 40	N/A

7.1.2. Mean Velocity

The comparison of the experimental and computational mean velocity profiles is carried out both upstream and downstream of the injection holes. The mean velocities were measured along the center line of the injection hole. Although the symmetry of the velocity field should be observed, the uncertainties involved in the measured values due to the injection flow condition and the positioning accuracy of the measuring equipment should be recognized.

Figures 7.8 and 7.9 show the mean velocity distribution at $R_M = 0.4, 0.8$. The velocities are normalized by the free stream velocity $U_m = 10$. Good agreement is observed by both treatments upstream of the injection at *X/d=-5*.

Downstream of the injection, the flow detaches and reattaches and a pair of kidney-shaped vortices are formed along the jet. Figures 7.10 and 7.11 show the predicted vector fields on the vertical streamwise plane (*Z=0*) and on the cross section (*Y-Z*) at X/d=3.

The comparison of the mean velocities downstream of injection indicates that good agreement between computation and experiment is achieved by the LK treatment at $R_M = 0.4$ in regions near the injection at X/d=3 and farther downstream at X/d=10, 20. However, the agreement deteriorates in regions farther downstream at the higher mass flow ratio, $R_M = 0.8$. The WF treatment generally cannot predict the mean flow gradient and the wall shear stress is not properly calculated by the coarse grid.

7.1.3. Turbulent Kinetic Energy

Figures 7.12 and 7.13 compare the measured and computed turbulent kinetic energy at $R_M = 0.4, 0.8$. The measured turbulent kinetic energy k is calculated from the measured turbulence intensity $\sqrt{(u')^2}$, as described in Section 6.4.2 (i.e. $k = 1.1\overline{(u')^2}$.) It should be

noted here that the measurement of the turbulence intensity along the centerline contains uncertainties about position and that there is an assumption of symmetry. Farther downstream these uncertainties should be reduced as spanwise gradients decrease.

Both computations give good agreement with experiments upstream of the injection $X/d=-5$. Downstream, but near the injection at $X/d=3$, the LK treatment gives good agreement at $R_M = 0.4, 0.8$ although slightly overpredicting the peak value. The WF treatment underestimates the turbulent kinetic energy and the position of the peak value is lower than measured.

Farther downstream at $X/d=10$ and $X/d=20$, good agreement is achieved by both treatments. The LK treatment gives a higher peak value of the turbulent kinetic energy than the measured one while the WF treatment gives lower values. The underprediction of k using the WF treatment was found near the wall $(Y/d<1)$, while good agreement was achieved using the LK treatment. At the higher mass flow ratio $R_M = 0.8$, the underprediction using the WF treatment becomes larger.

7.1.4. Film Cooling Effectiveness

Figures 7.14 shows a comparison of the computed and measured spanwise-averaged effectiveness as well as the effectiveness along the center line downstream of an injection hole at $R_M = 0.2, 0.4, 0.8$. Detailed surface cooling effectiveness distributions are shown in Figures 7.15-7.17. In the experiments, measurements of cooling effectiveness were carried out in half of the domain due to the symmetry situation.

At mass flow ratio $R_M = 0.2$, the LK treatment gives good averaged and center line effectiveness everywhere downstream of the injection. The WF treatment severely overpredicts the center line effectiveness. Good prediction of averaged effectiveness is obtained using the WF treatment except in the region near the injection where the effectiveness is underpredicted due to the false diffusion on the coarse grid.

As mass flow ratio increases to $R_M = 0.4, 0.8$, the agreement between averaged effectiveness calculated using the LK treatment and the experimental measurements near the injection hole deteriorates, although good agreement is still obtained in the recovery region. The underprediction of the averaged effectiveness is probably caused by inadequate modeling of the complex flow immediately downstream of the injection. From the surface cooling effectiveness distribution, it is found that the LK treatment overpredicts the penetration of the jet due to the fact that the increased turbulent mixing resulting from nonequilibrium turbulence and swirling flow at high mass flow ratio is not well represented by the present model. The computations generally under-predict the spanwise spreading of the jet, despite the use of the nonisotropic turbulent eddy-viscosity.

Conversely, as the mass flow ratio increases to $R_M = 0.4, 0.8$ the WF treatment consistently gives lower averaged effectiveness than the measured values even farther downstream while the center line effectiveness appears to be improved at $R_M = 0.8$. Due to the lack of near-wall flow resolution, the penetration of the jet is overpredicted and the spanwise spreading of the jet is severely underpredicted.

The present comparison shows that the LK treatment improves the prediction of effectiveness. However, it also suggests that the k-ε turbulence model cannot correctly describe the turbulence stresses and scalar fluxes when the shear flow between the main stream and jets is high and the associated streamwise vorticity is strong. Based on the 2-D computations, it appears that the turbulence modelling of the complex flow at high mass flow ratio can be improved by using the M-T-S turbulence model which takes into account the increased non-equilibrium turbulence.

In the present work, the M-T-S turbulence model was added to the 3D-MGFD code. However, the code could not provide a converged solution due to the fact that in the code all variables are solved simultaneously in a coupled nature (see Appendix D). An attempt should be made to decouple the turbulence equations from the mean flow in order to stablize the turbulence equations.

Also, it appears that the stronger vortices downstream of injection at higher mass flow ratios require a solution of the full Reynolds stress equation in order to take into account the nonisotropic turbulence resulting from the swirling flow in the vortices.

7.2. Parametric Analysis

7.2.1. Computational Domain and Boundary Conditions

Computations have been carried out for single and double staggered cooling orifices. The computational domain is shown in Figure 7.18. The parameters used in the tests were chosen as suggested in the work of Gartshore et al. (1991) (See Table 7.2). For the inclined jets, the coolant orifice was not square at the exit surface and this was taken into account. The arrangement of the computational grid was the same as in the previous section. For the two-row injection, a uniformly refined grid was used between the rows to ensure that the interaction between the jets is well represented.

Table 7.2: 3-D parametric tests.

Parameter	Value
Mass Flow Ratio	$R_M = 0.4, 0.8, 1.2$
Injection Angle to the Mainstream	$\alpha = 0^o, 90^o$
Injection Angle to the Surface	$\beta = 30^o$
Hole Spacing	$S/d= 4, 5$
Row Spacing	$R/d=3$
Stagger factor	$A/d=0, 1, 2, 3$

Non-uniformity of the injection flow at the slot exit has been observed in the computed results for the vertical cooling orifices. Figure 7.19 shows the predicted mean

velocity at the exit of an injection hole. The mean injection flow velocity is 4 m/s. It is found that at the exit surface, the vertical velocity reaches a peak value of about 7 m/s while the streamwise velocity has a more uniform value of about 2 m/s over the whole surface. The influence of this nonuniformity on the cooling effectiveness is studied by carrying out a computation with no slot and an assumed uniform injection at the injection location. Figure 7.20 shows the predicted film cooling effectiveness by computations with and without a slot. The comparison indicates that the averaged effectiveness has less than ±0.05 difference near the injection and no appreciable difference farther downstream. However, the center line effectiveness has ±0.10 difference near the injection and less than ±0.02 difference farther downstream. This suggests that computations within the injection oriface might be required in order to study the detailed distribution of effectiveness near the injection.

Since the present code is limited to a Cartesian coordinate system, special treatment is needed for computations with an inclined jet. Nevertheless, some indication of the effects of the non-uniform flow can be determined by assuming a flow profile based on the observations in the vertical cooling orifice computations. This issue of the uniformity of the flow at the slot exit needs to be explored further using codes able to correctly represent non-Cartesian systems.

In the present computations, the jet flow at the exit is assumed to follow the injection direction. Therefore, the velocity components of the jet can be expressed as

$$U = V_T \cos\beta \sin\alpha, \qquad V = V_T \sin\beta, \qquad W = V_T \cos\beta \cos\alpha \qquad (7.1)$$

where V_T denotes the total velocity at each point on the exit surface. The total velocity can be distributed uniformly: $V_T(x,z) = V_M$, where V_M is the jet mean velocity. However, in order to take into account the non-uniformity of the jet, a simple linear distribution for V_T is assumed on the exit surface. For example, for the lateral injection,

$$V_T(x,z) = V_M \left(\frac{2x}{d_x} + 1 \right) \left(\frac{2z}{d_z} + 1 \right) \qquad (7.2)$$

where d_x and d_z represent the hole width in X and Z directions.

Figure 7.21 shows the predicted cooling effectiveness values resulting from the uniform and linear jets. The linear jet has a higher peak velocity at the edge of the exit, thus higher lateral injection momentum, which prevents the coolant from detaching from the surface. The resulting cooling effectiveness near the injection orifice with the linear profile is higher than with the uniform profile. However, the difference is reduced at the higher mass flow ratio $R_M = 0.8$. No significant effects have been found far downstream of the injection.

7.2.2. Finite Array Effects

For the film cooling with lateral injection, it is assumed that there are an infinite number of holes in the lateral direction. Because of periodicity in that direction, the computational domain is restricted to one period as shown in Figure 7.18. In the present work, the periodic boundary condition is imposed at the level of the discretized equations by adding extra computational cells outside of the computational domain and imposing periodic values. Such treatment is introduced in the 3D-MGFD code and the procedure can be described as follows: Considering a row of grid cells, which includes two surfaces where the periodic boundary conditions need to be imposed (See Figure 7.22). The periodic condition is imposed before each smoothing by letting

$$U_{i,Nk} = U_{i,2}, \qquad U_{i,1} = U_{i,Nk-1}$$
$$S_{i,Nk} = S_{i,2}, \qquad S_{i,1} = S_{i,Nk-1} \tag{7.3}$$

With this updated flow field, the velocity components $W_{i,Nk}, W_{i,2}$ on the surfaces are calculated in the same way as those in the interior nodes. The mass fluxes through both surfaces are monitored to determine the convergence of this iterative procedure. Less than 1% imbalance in the mass fluxes on the surfaces was found once the iterations in the entire computational domain have converged to specified criteria.

The computations with the periodic array represents film cooling with a large number of holes in a row. It is different from the case of a finite array (e.g. 5 to 6 holes), which is often used in experimental studies. This difference can be demonstrated by comparing the film cooling effectiveness distributions predicted by a finite array (5 holes) and the periodic array as shown in Figures 7.23 and 7.24. For the finite array computations, two edge-walls ($Z/d=\pm16$) were treated as solid walls.

At the lower mass flow ratio $R_M = 0.8$, the surface effectiveness near the injection *(X/d<15)* downstream of the middle hole is close to that observed in the periodic array. However, at the higher mass flow ratio $R_M = 1.2$, the effectiveness distribution downstream of each hole of the finite array varies significantly from one hole to another. The difference can also be shown by comparing the averaged effectiveness of the periodic array and middle section of the finite array (see Figure 7.25). This effect increases with increasing R_M, presumably because the coolant layer becomes thicker and the disturbance at the edge of the finite array becomes larger and more significant.

7.2.3. Single-Row Injection vs. Double-Row Injection

Figure 7.26 shows the spanwise-averaged cooling effectiveness for streamwise and lateral injection for a single-row of holes and for lateral injection for a double-row of holes. The total mass flow ratio was chosen to be equal for single and double row injection and its value, R_M, is defined by the mass flow ratio for single row cases. Lateral injection performs much better than streamwise injection near the coolant orifice but loses its advantage farther downstream. The best cooling performance is given by the double-row lateral injection. The superior performance of the lateral injection is attributed to: 1) the higher spanwise spreading of the laterally injected coolant which forms more uniform spanwise effectiveness distributions downstream of the injection, and 2) the single dominant vortex formed downstream of each hole which interacts with the neighboring fluid to push cold fluid towards the surface near $Z=0$. Comparison of the single- and

double-row lateral injections shows a lower penetration for the double row but also a strong interaction of vortices which tends to push colder fluids toward the surface.

Figure 7.27 illustrates the film cooling effectiveness distribution on the wall. The superior coverage of the lateral injection arrangement is obvious. This is further illustrated in Figure 7.28 which shows the concentration in planes perpendicular to the cooled surface at a distance of *X/d=3* from the coolant orifice. As expected, the spanwise spreading of the coolant distribution is much higher for lateral than for streamwise injection.

The flow distribution in the film cooling process can be shown with vector velocity fields in a cross flow plane at *X/d=3* (Figure 7.28). For streamwise single row injection, two symmetric vortices are formed which lift the coolant jet near *Z=0* and entrain the hot fluid towards the surface and therefore deteriorate the cooling effectiveness. For the lateral injection a single dominant vortex is formed and its interaction with the neighboring fluid tends to push the cold fluid towards the surface.

7.2.4. Hole Spacing Effect in Single-Row Injection

The effect of spanwise hole spacing on the cooling effectiveness is studied for lateral injection with hole spacings of *S/d=4* and *5*. In the present tests, a mass flow ratio per unit span $R_S = \dfrac{R_M}{S/d}$ is introduced which is proportional to the mean flow from the coolant holes divided by flow across the holes in an area one d high and S width, is introduced. The tests are carried out at three mass flow ratios, $R_S = 0.1, 0.2, 0.3$. Figure 7.29 shows the averaged cooling effectiveness ($\overline{\eta}$) of lateral injection. There exists a small region just after the injection where $\overline{\eta}$ decreases with an increase of R_S. As the spacing increases from *S/d=4* to *5*, the drop of $\overline{\eta}$ with R_S becomes larger and this drop can be found farther downstream (up to *X/d=5~8)*. Far downstream of the injection, $\overline{\eta}$ increases with R_S.

Overall, wider spacing gives consistently lower $\bar{\eta}$ in the present testing range, which is shown in Figure 7.30.

The detailed surface cooling effectiveness distribution, the vector field and the concentration contours in a cross plane at $X/d=3$ of a single-row lateral injection for $X/d=4$ and 5 are shown in Appendix B.1. It is clear that small spacing is preferred for overall cooling performance (although in real design, there exist structural and machining problems if the holes are too close together). Also, low mass flow ratio is preferred for better performance near the injection region. The film cooling process can be explored further by investigating the flow and coolant distribution farther downstream. For the lateral injection, a dominant vortex is formed for each injection orifice. This vortex lifts the cool fluid away from the surface which is then pushed back towards the surface by the neighboring vortex. Such interaction is enhanced as R_S increases. It is found that the vortex interaction has a negative effect on the overall $\bar{\eta}$ in the region near injection where the fluid has higher temperature gradients near the wall surface than in the fluid farther downstream. Farther downstream, $\bar{\eta}$ increases with R_S since the vortex interaction is weaker. For $S/d=5$, the interaction between the vortices loses more cold fluid into the mainstream than for $S/d=4$, due to the larger spacing. This phenomenon is more severe for higher mass flow ratios.

7.2.5. Stagger Effect in Double-Row Injection

The cooling performance of double row lateral injection is studied on four staggered-hole arrangements, $A/d=0, 1, 2, 3$, where A indicates the shift between the two rows of holes that have hole spacing $S/d=4$. ($A=0$ represents in line holes and $A=0$ is the same as $A=4$.) The total mass flow ratio, R_M, was chosen to be equal to the mass flow ratio for single row cases.

.   Figures 7.31 and 7.32 show the spanwise-averaged cooling effectiveness for double row lateral injection with four staggered-hole arrangements. The arrangement of

A/d=3 shows superior performance over the other arrangements for $R_M = 0.4, 0.8, 1.2$ while *A/d=1* shows reduced overall performance. The arrangement of *A/d=0* (in line) gives promising performance especially, near the injection region as R_M increases.

Figure 7.33 show the predicted effectiveness vs. the stagger factor *A/d* resulting from the four hole arrangements. The lowest value of effectiveness can be found consistently between A/d=1 and 2 in the present range of parameters. The best performance can be found consistently between A/d=3 and 4. The fully staggered arrangement is commonly used in the real design because of the needs for structural integrity and efficient internal cooling. These tests suggest that it is possible to consistently achieve better performance, even with the fully staggered arrangement, by changing the injection direction slightly streamwise. Further investigation needs to be carried out using a generalized coordinate system.

The detailed surface effectiveness distributions are shown in Appendix B.2. The flow and coolant distribution downstream is studied in order to gain insight into the double-row film cooling process. The vector fields and concentration contours in a cross flow plane at *X/d=3* are given in Appendix B.2 with discussions.
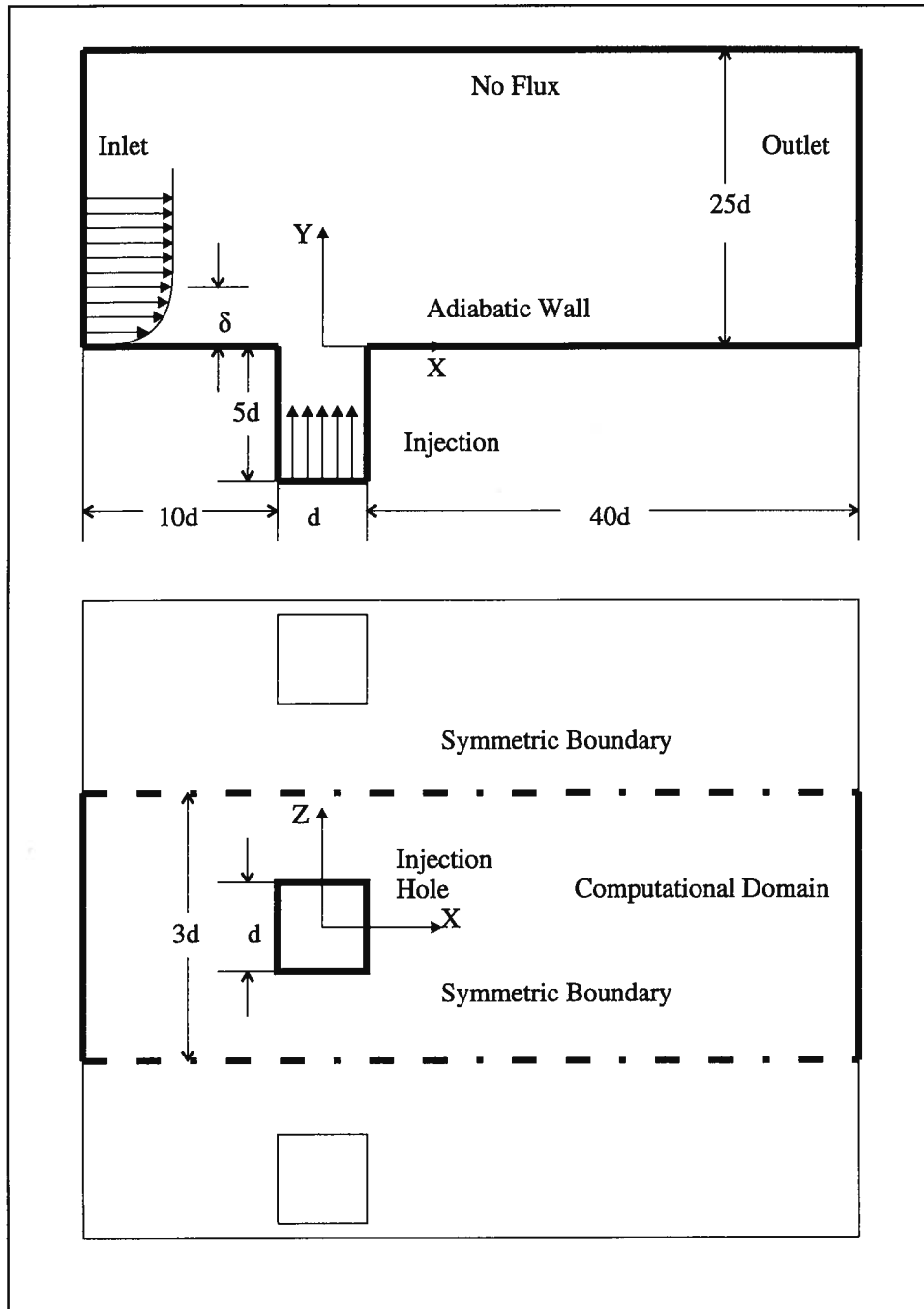
Figure 7.1: Computational domain for 3-D film cooling model.
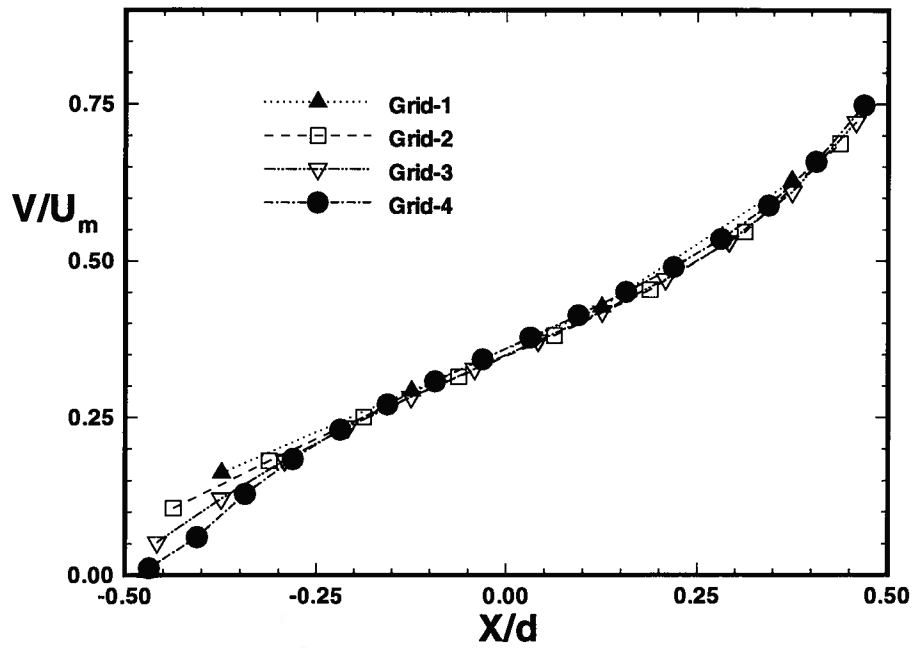
Figure 7.2: Vertical mean velocity at the hole exit predicted by four progressively refined grids (KE&LK, $R_M = 0.4$).
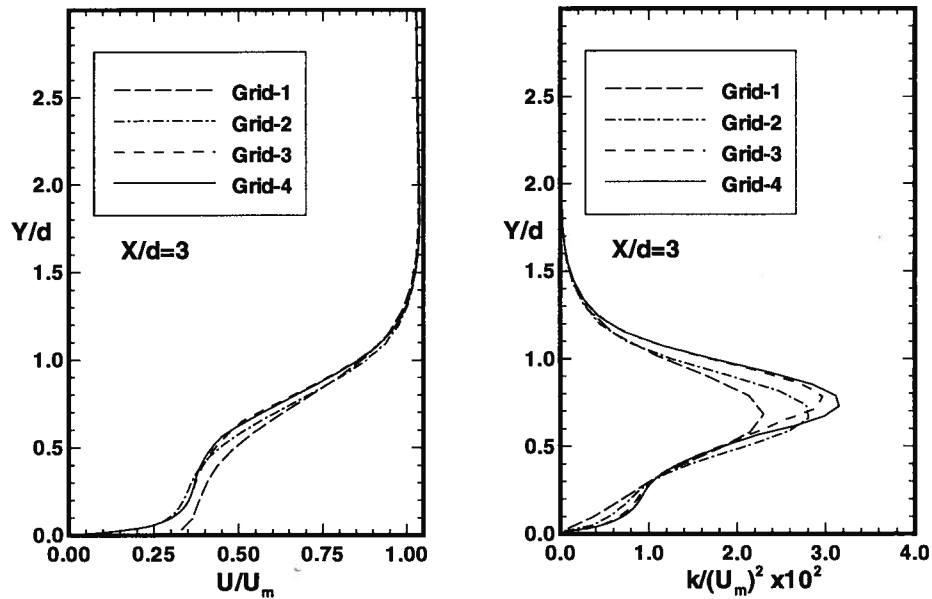
Figure 7.3: Mean velocity and turbulence kinetic energy at $X/d = 3$ predicted by four progressively refined grids (KE&LK, $R_M = 0.4$).
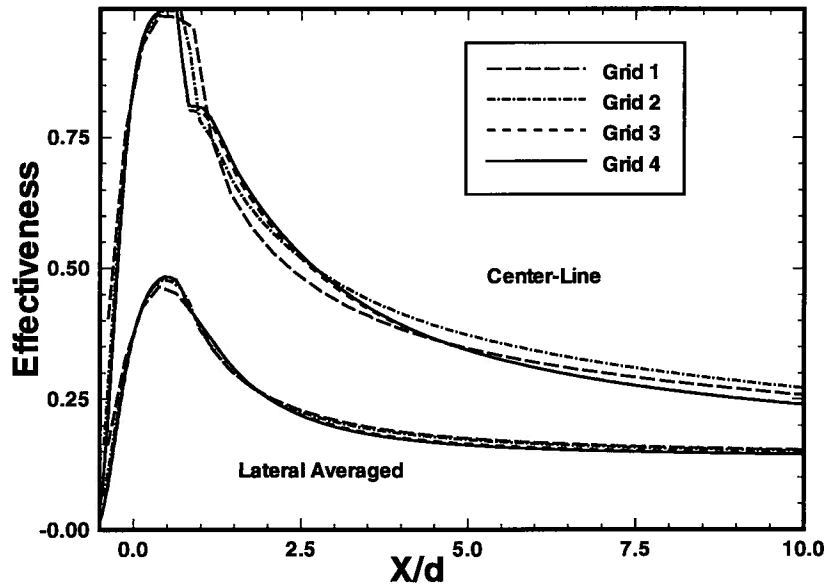
Figure 7.4: Film cooling effectiveness predicted by four progressively refined grids (KE&LK, $R_M = 0.4$).
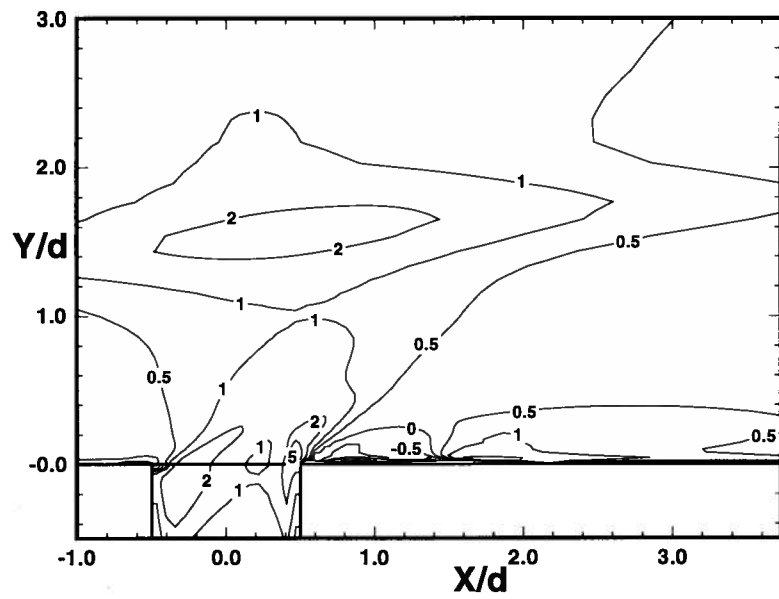
Figure 7.5: Estimated false diffusion coefficient on the vertical streamwise plane $Z = 0$ using Grid 3 (KE&LK, $R_M = 0.4$).

X/d=0.5
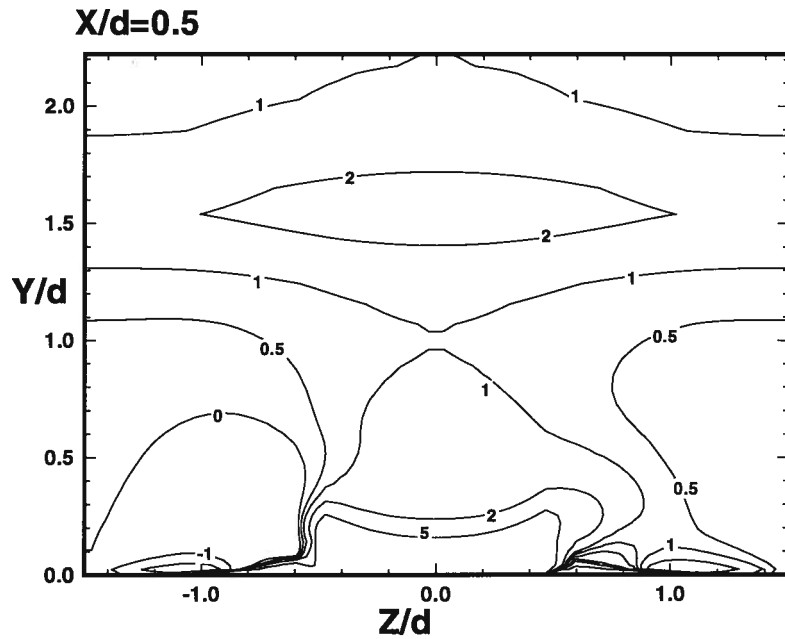
Figure 7.6: Estimated false diffusion coefficient on the vertical cross plane $X = 0.5$ using Grid 3 (KE&LK, $R_M = 0.4$).
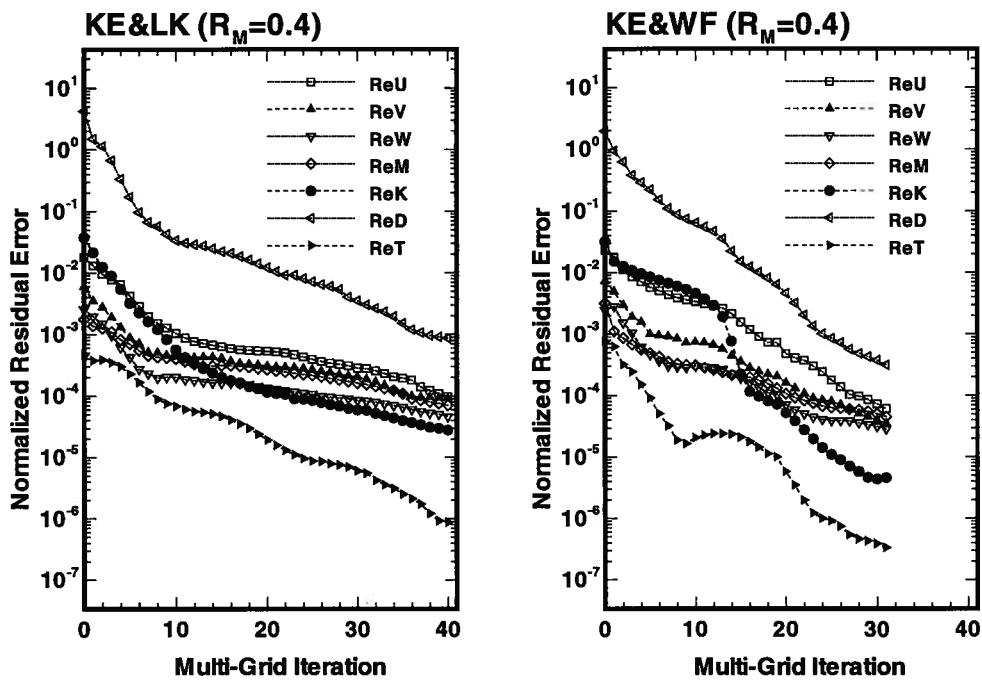
Figure 7.7: Typical 3D-MGFD iteration convergence performance ($R_M = 0.4$).
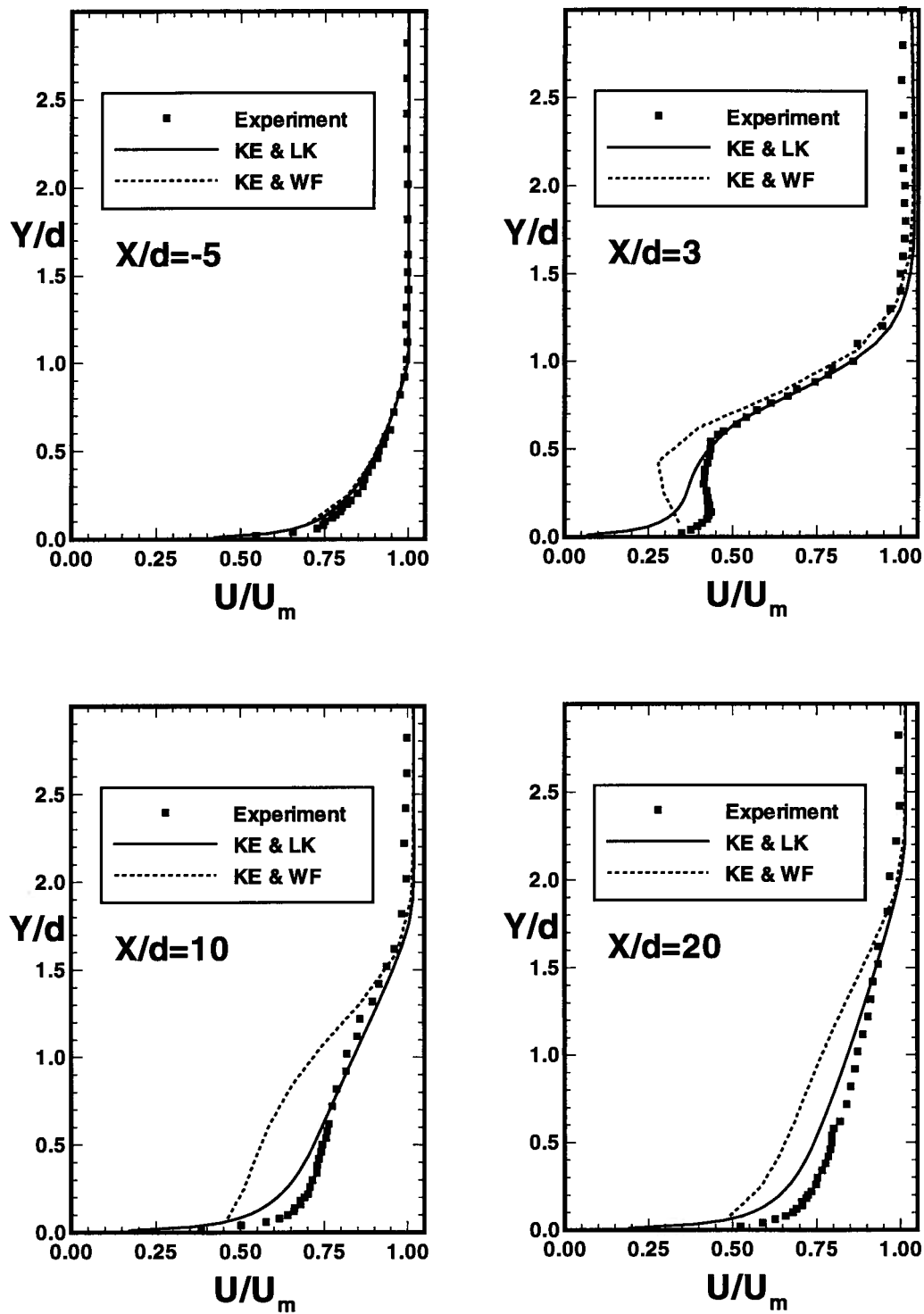
Figure 7.8: Mean velocity distribution (3-D model, $R_M = 0.4$).
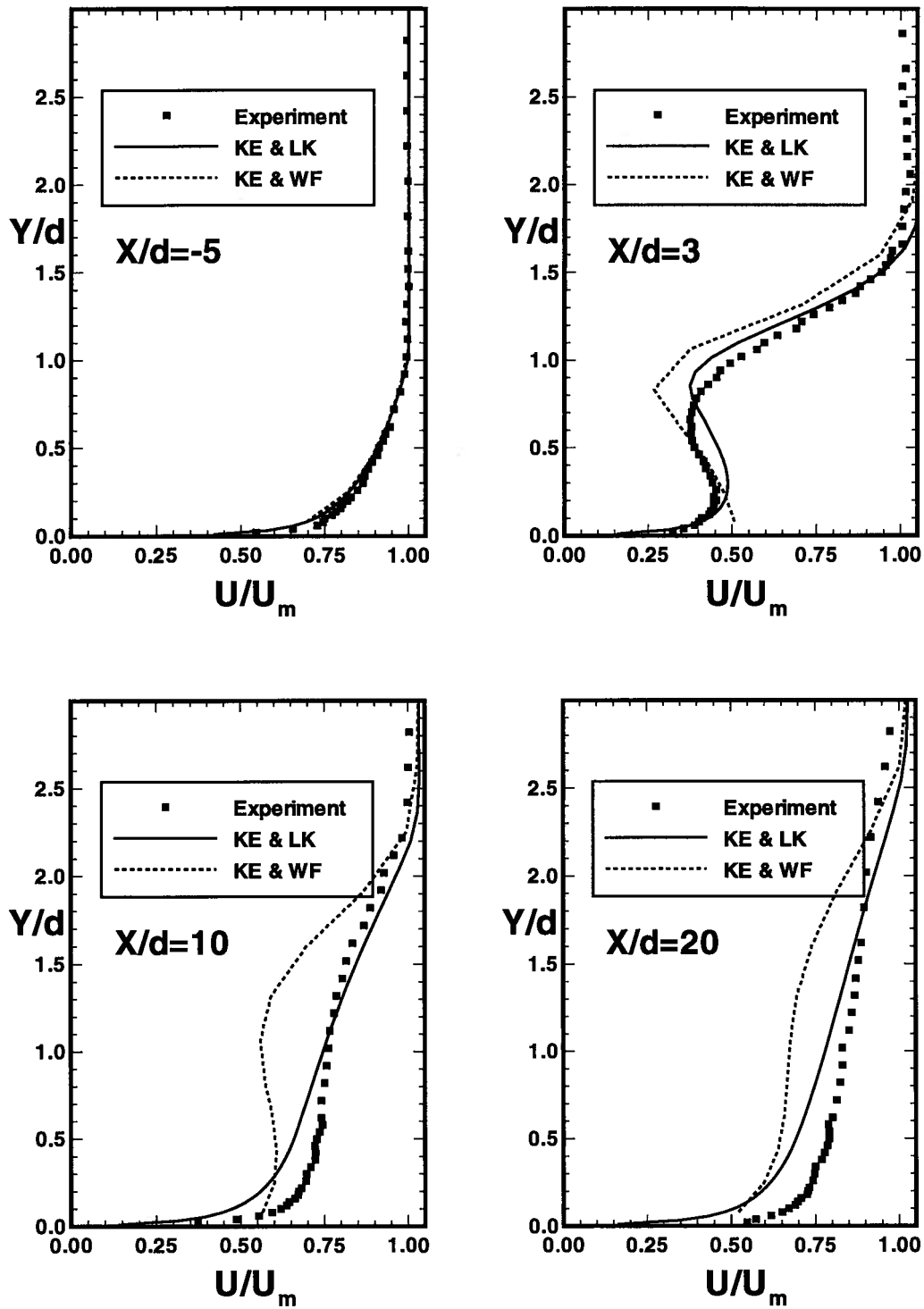
Figure 7.9: Mean velocity distribution (3-D model, $R_M = 0.8$).
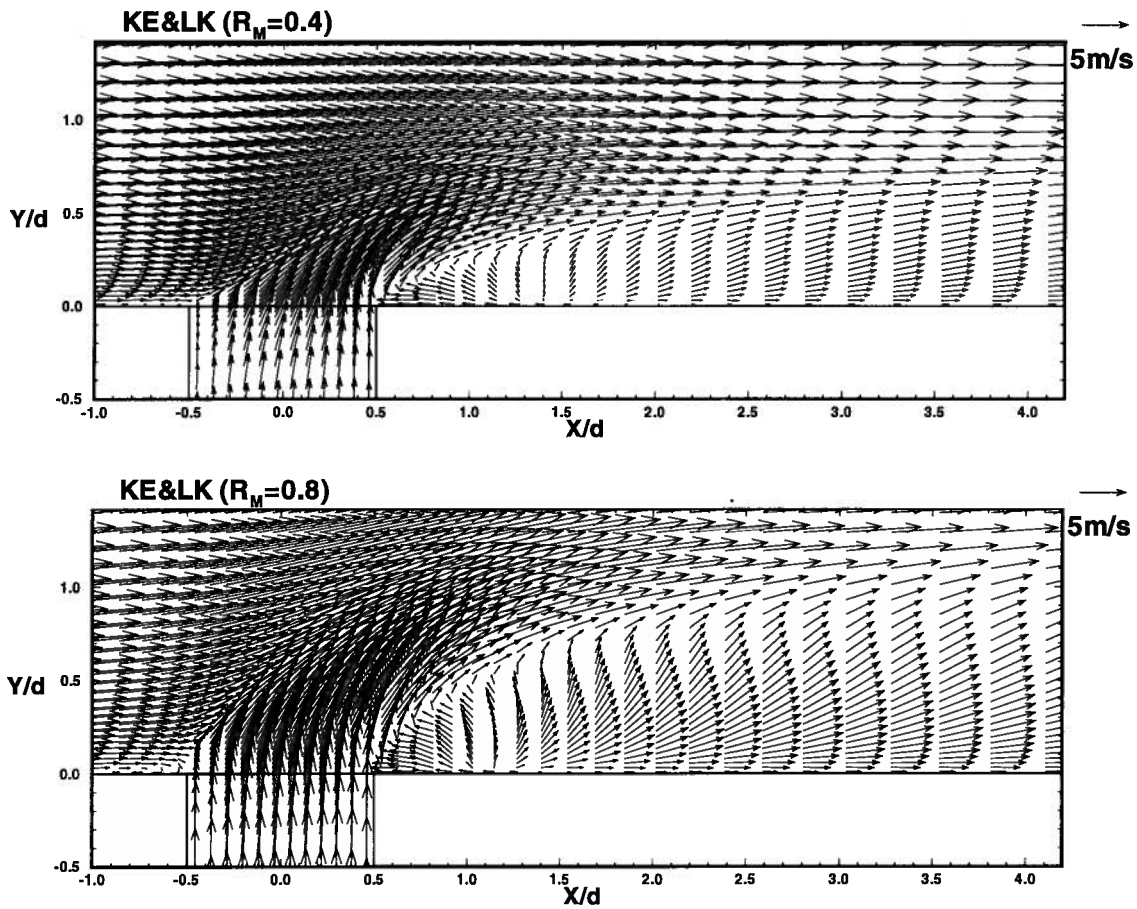
Figure 7.10: Predicted vector fields on the vertical streamwise plane $Z = 0$ (KE&LK, $R_M = 0.4, 0.8$).
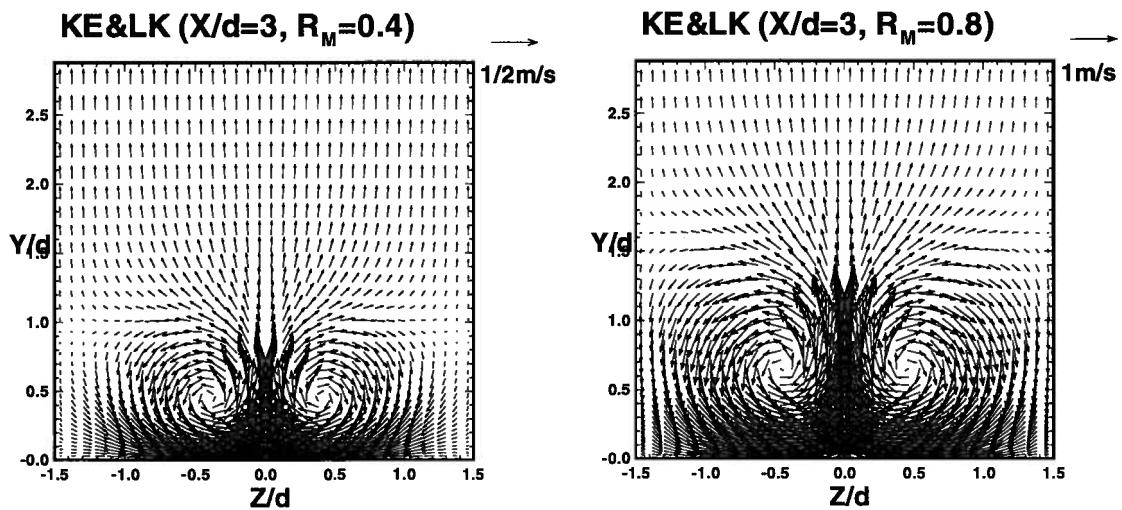
Figure 7.11: Predicted vector fields on the vertical cross plane $X/d = 3$ (KE&LK, $R_M = 0.4, 0.8$).
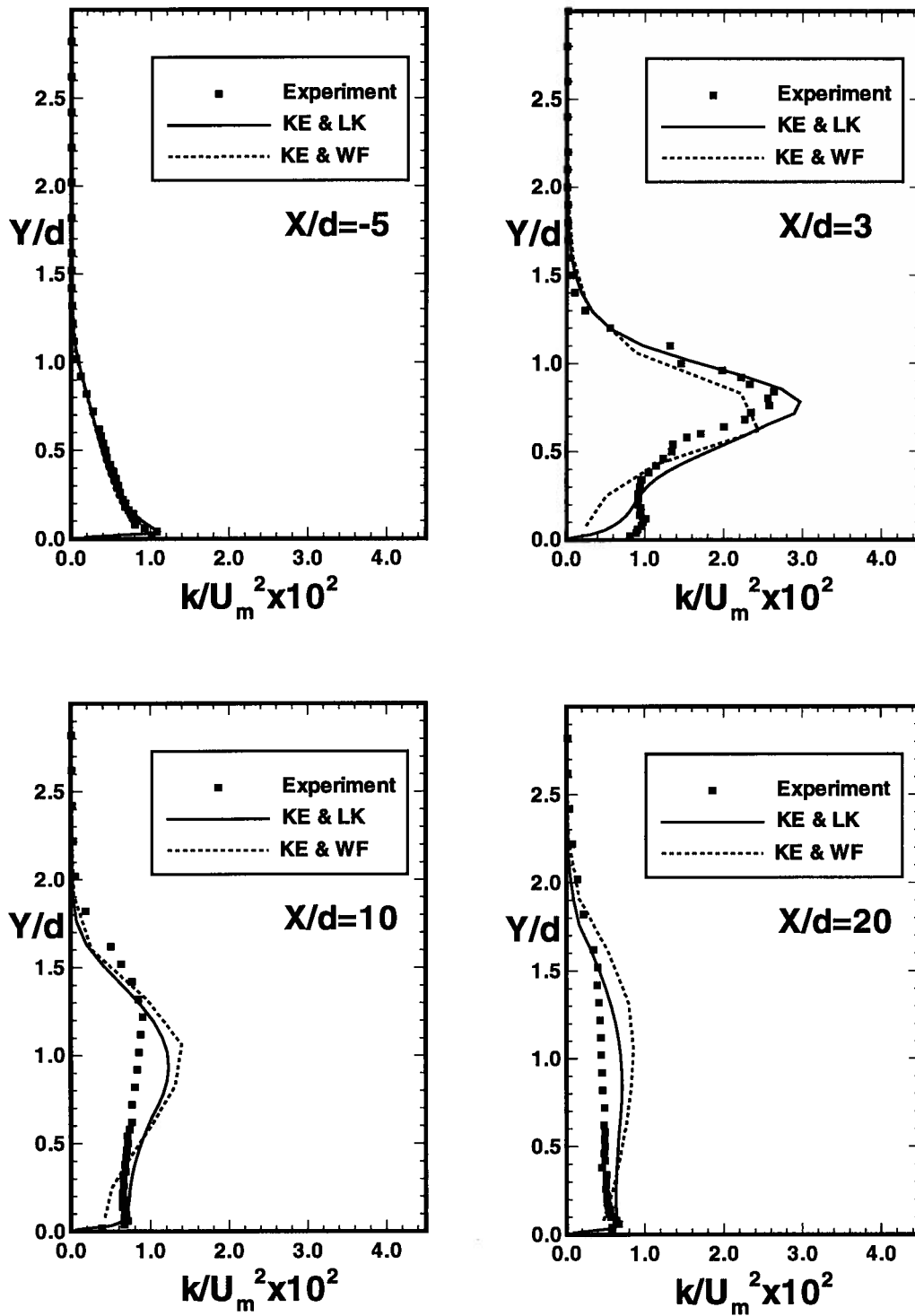
Figure 7.12: Turbulent kinetic energy distributions (3-D model, $R_M = 0.4$).
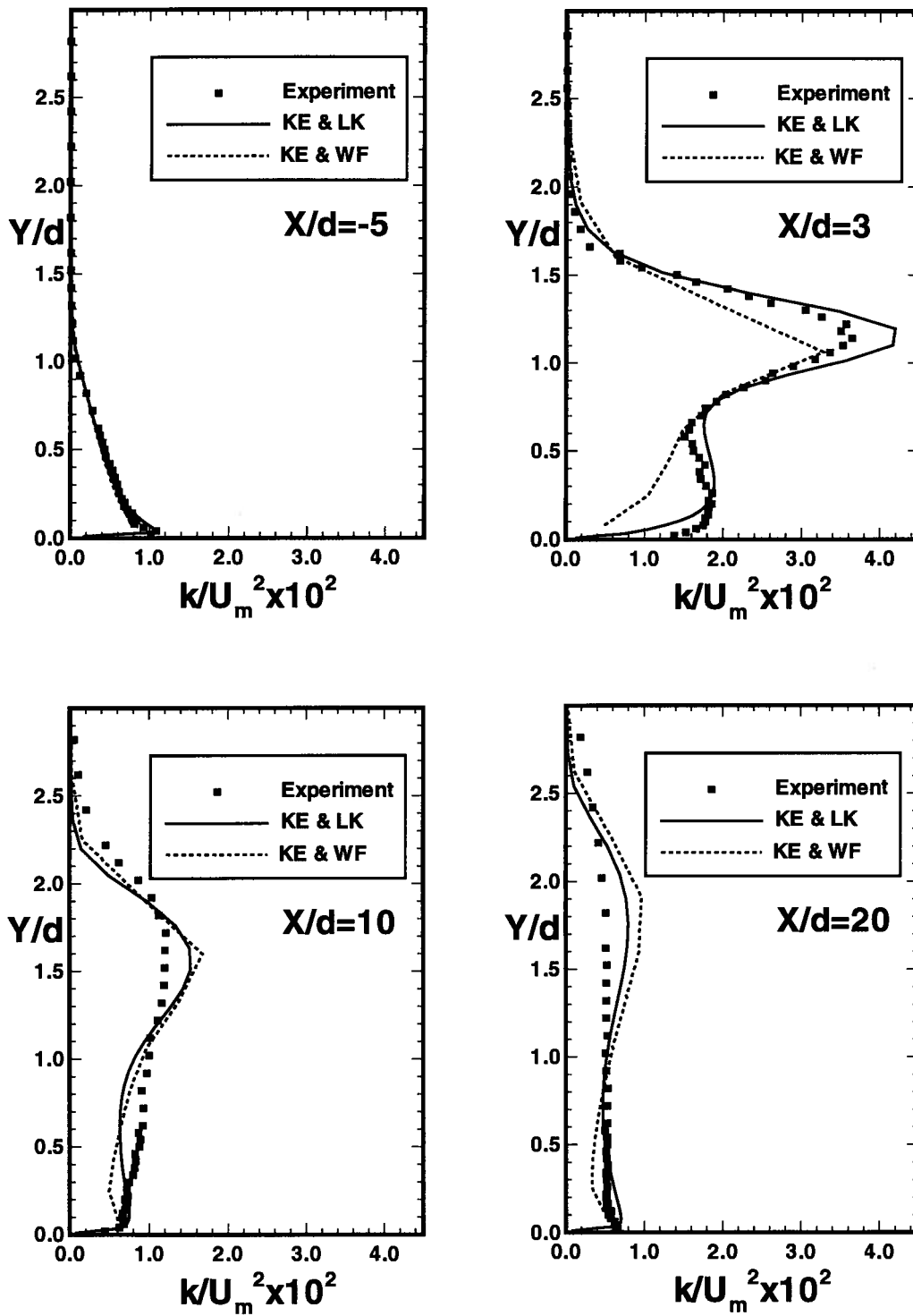
Figure 7.13: Turbulent kinetic energy distributions (3-D model, $R_M = 0.8$).
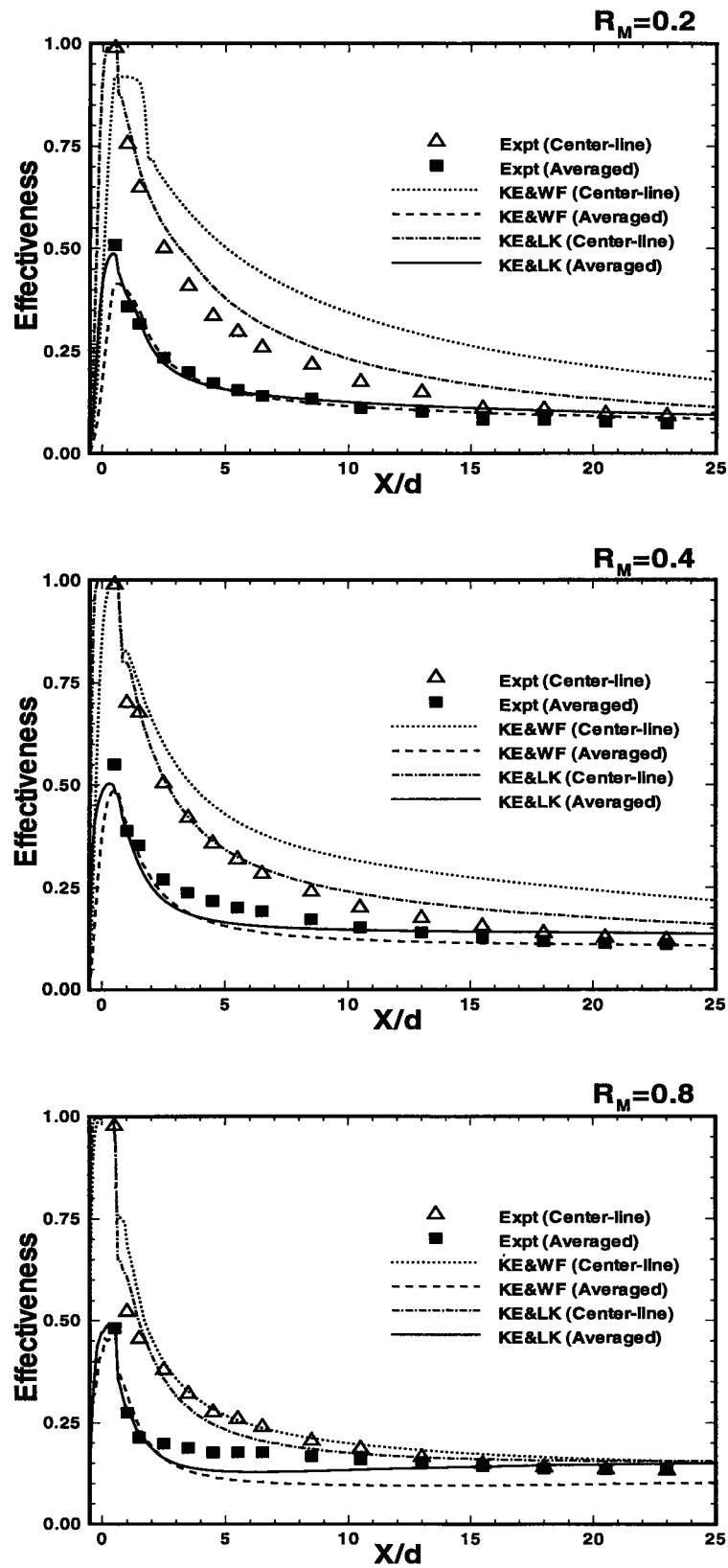
Figure 7.14: Film cooling effectiveness (3-D model, $R_M = 0.2, 0.4, 0.8$).
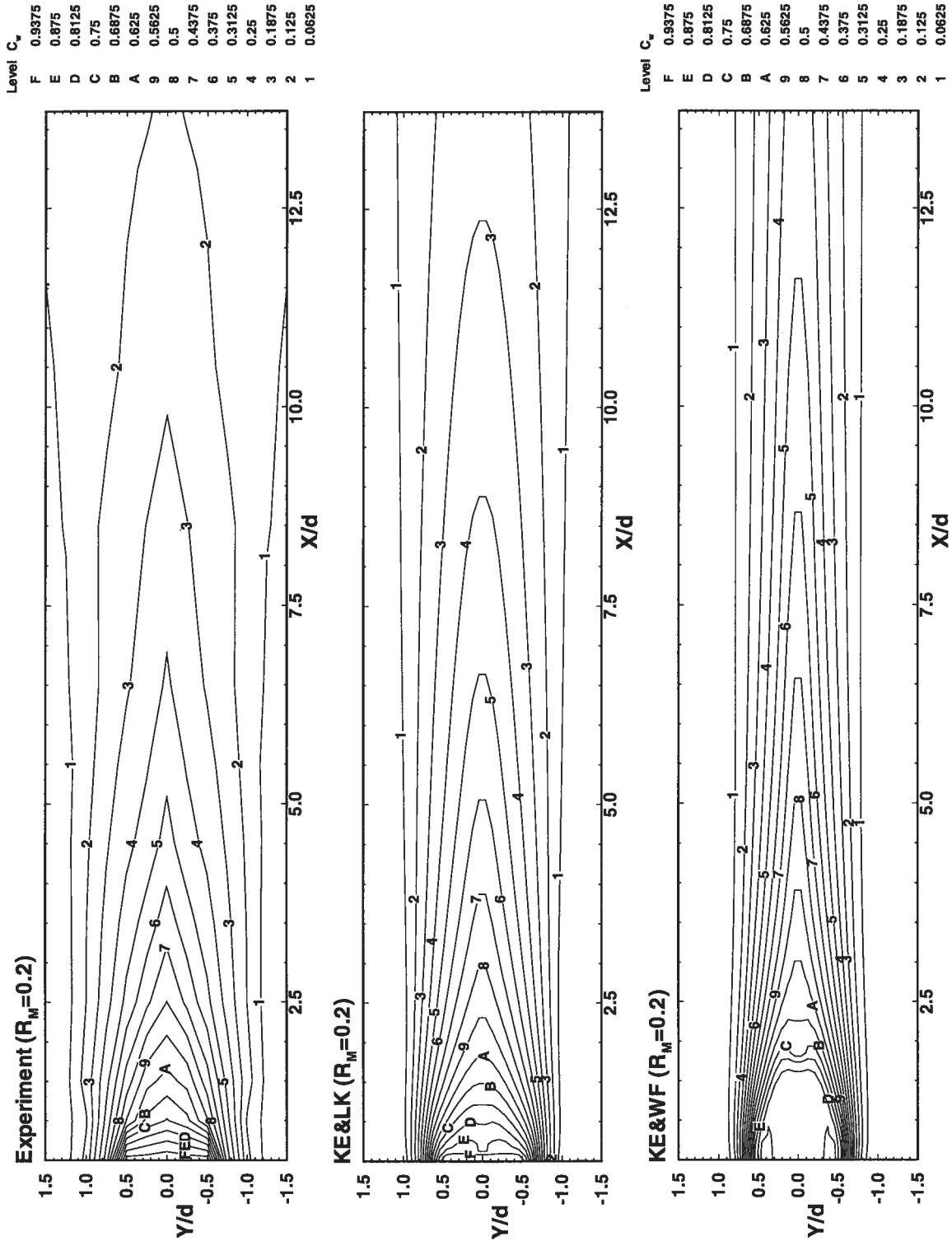
Figure 7.15: Film Cooling effectiveness distribution on the wall surface ($R_M = 0.2$).
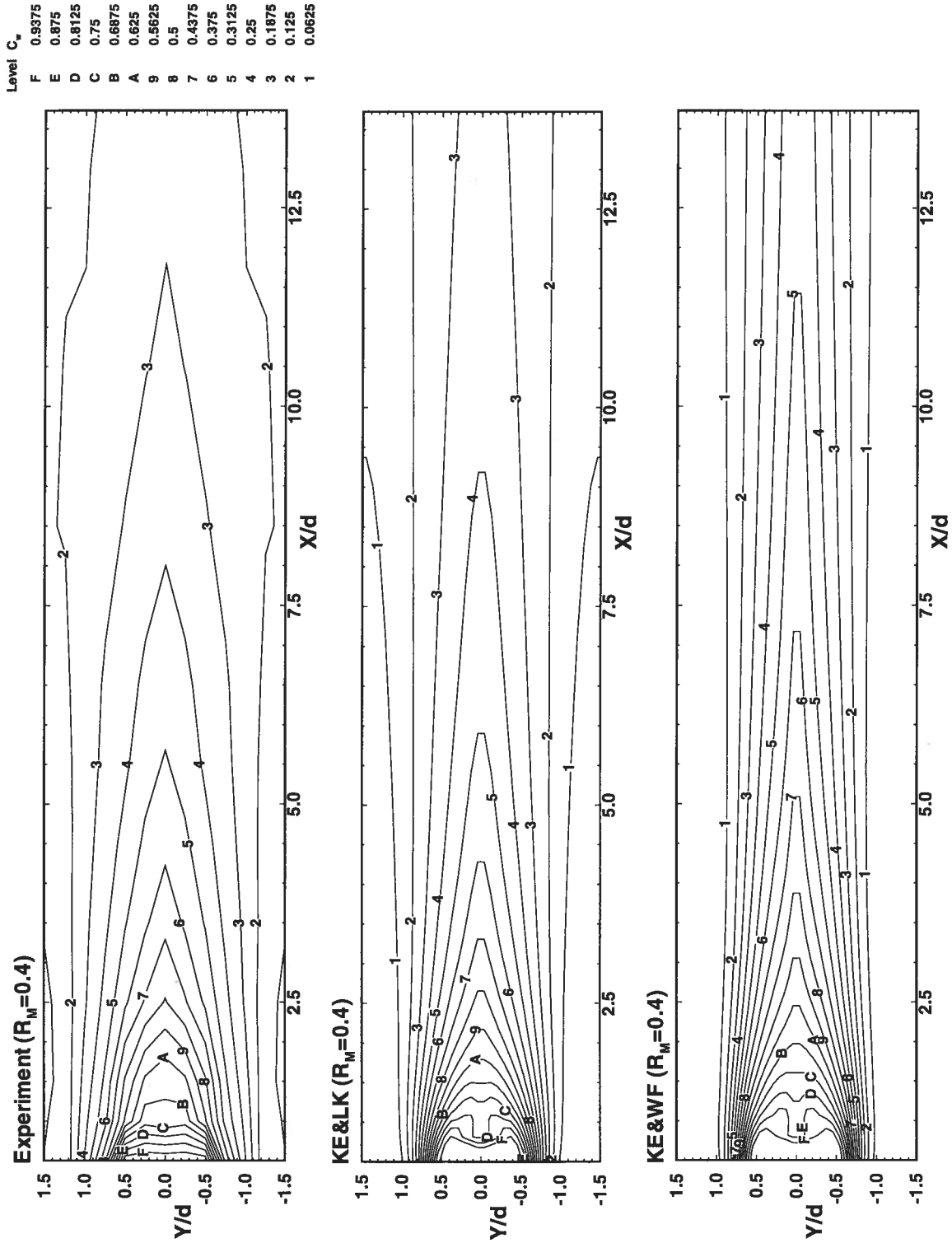
Figure 7.16: Film Cooling effectiveness distribution on the wall surface ($R_M = 0.4$).

Level	C_w
F	0.9375
E	0.875
D	0.8125
C	0.75
B	0.6875
A	0.625
9	0.5625
8	0.5
7	0.4375
6	0.375
5	0.3125
4	0.25
3	0.1875
2	0.125
1	0.0625
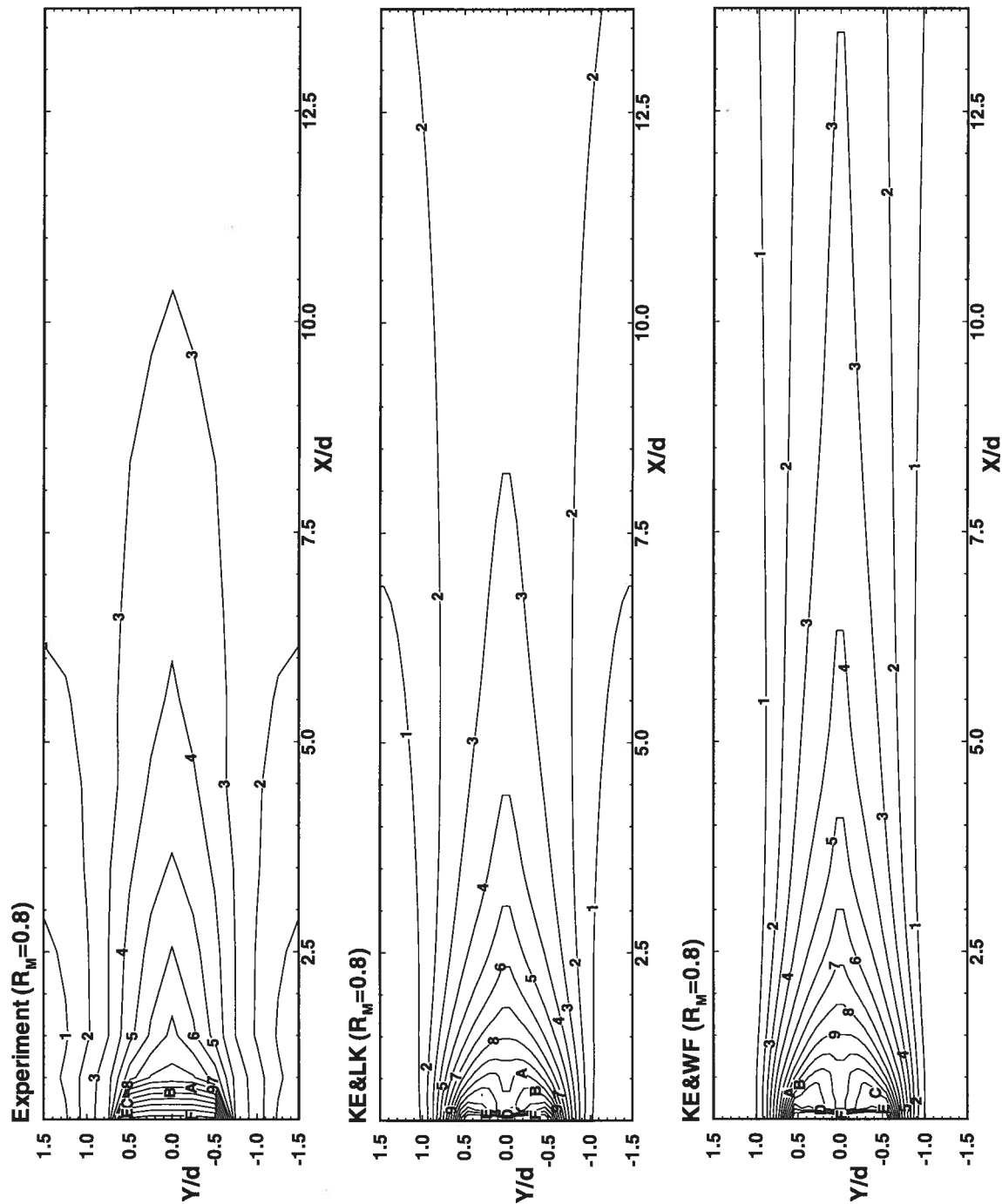
Figure 7.17: Film Cooling effectiveness distribution on the wall surface ($R_M = 0.8$).
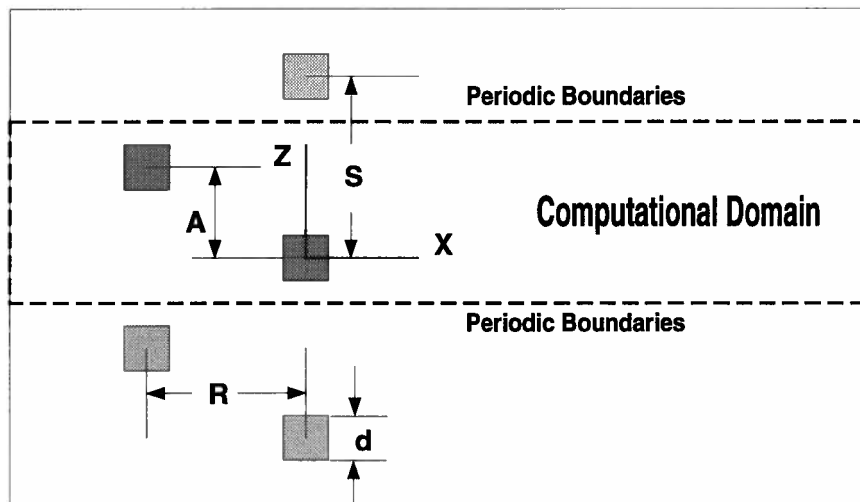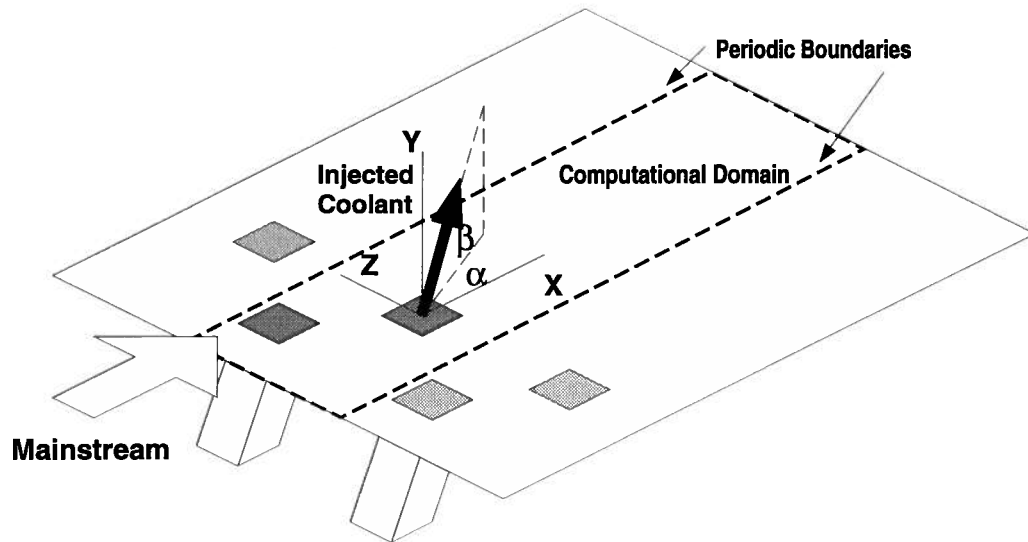
Figure 7.18: Computational domain for 3-D parametric tests.
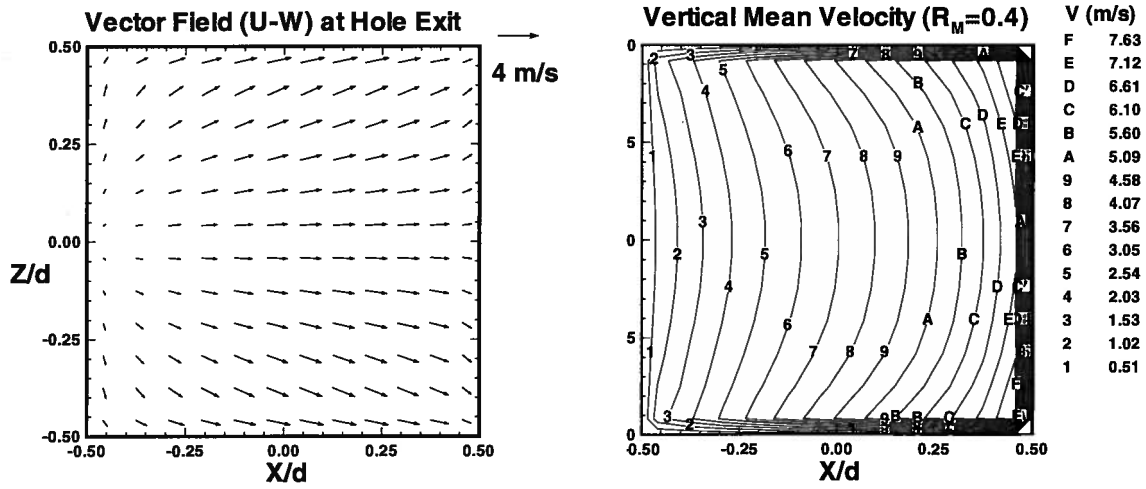
Figure 7.19: Predicted Mean velocity at the hole exit (KE&LK, $R_M = 0.4$).
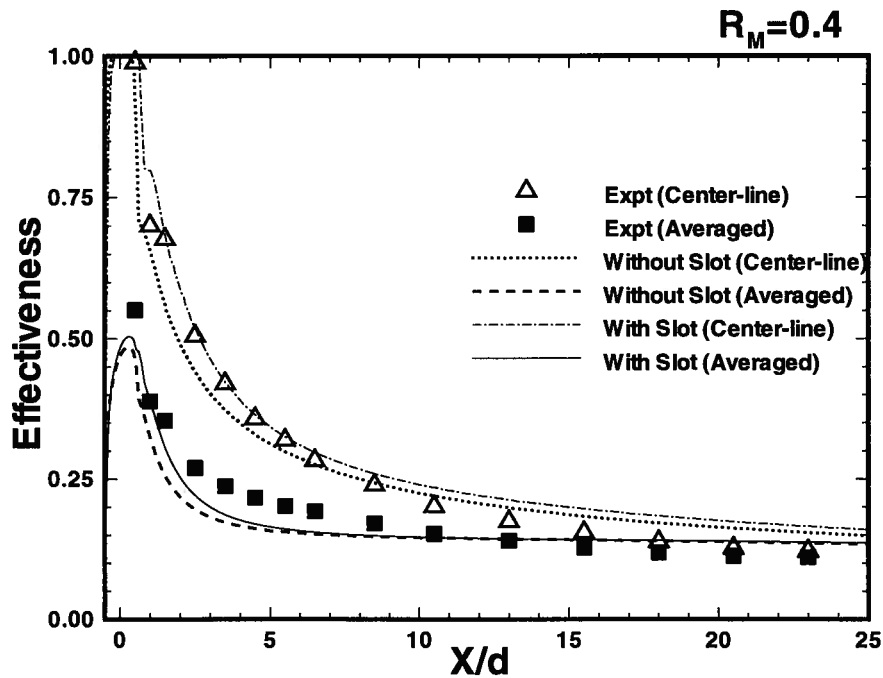
Figure 7.20: Film Cooling effectiveness predicted by a) No slot and an assumed uniform injection (without slot) and b) Including the slot (with slot) (KE&LK, $R_M = 0.4$).
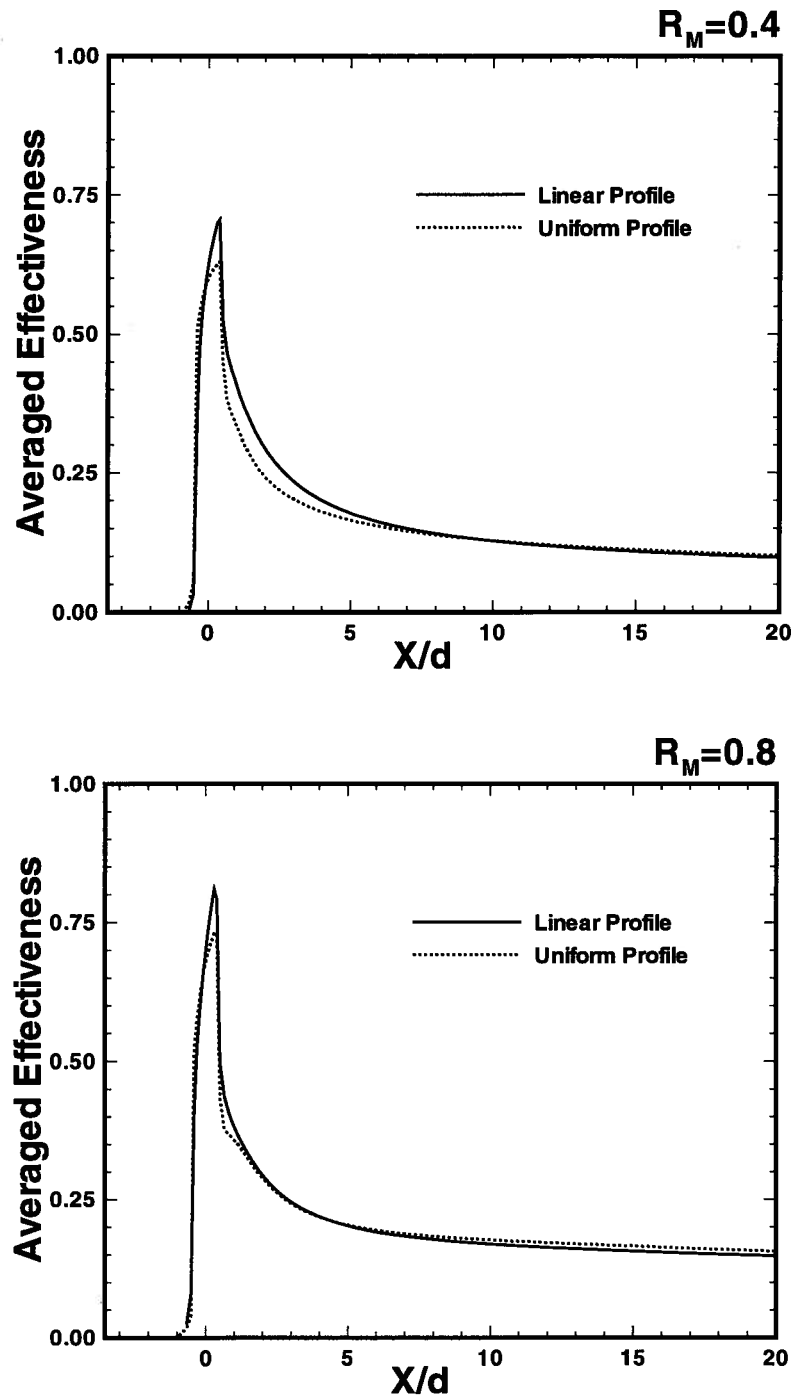
Figure 7.21: Film cooling effectiveness predicted by linear and uniform injection flow profiles ($S/d = 4$).
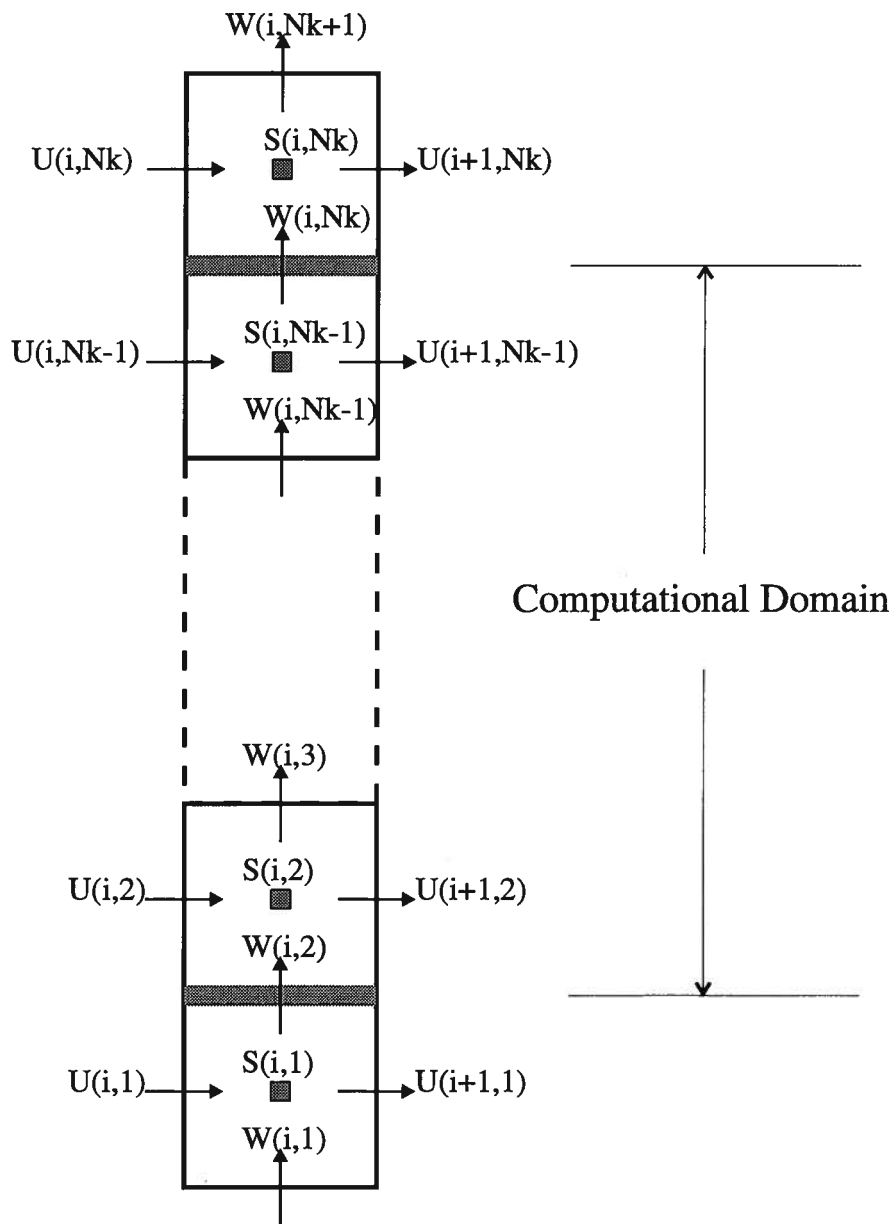
Figure 7.22: Schematic description of the periodic boundary condition.

Finite Array (R$_M$=0.8)

Level	c$_w$
F	0.94
E	0.88
D	0.81
C	0.75
B	0.69
A	0.62
9	0.56
8	0.50
7	0.44
6	0.38
5	0.31
4	0.25
3	0.19
2	0.12
1	0.06

Periodic Array (R$_M$=0.8)
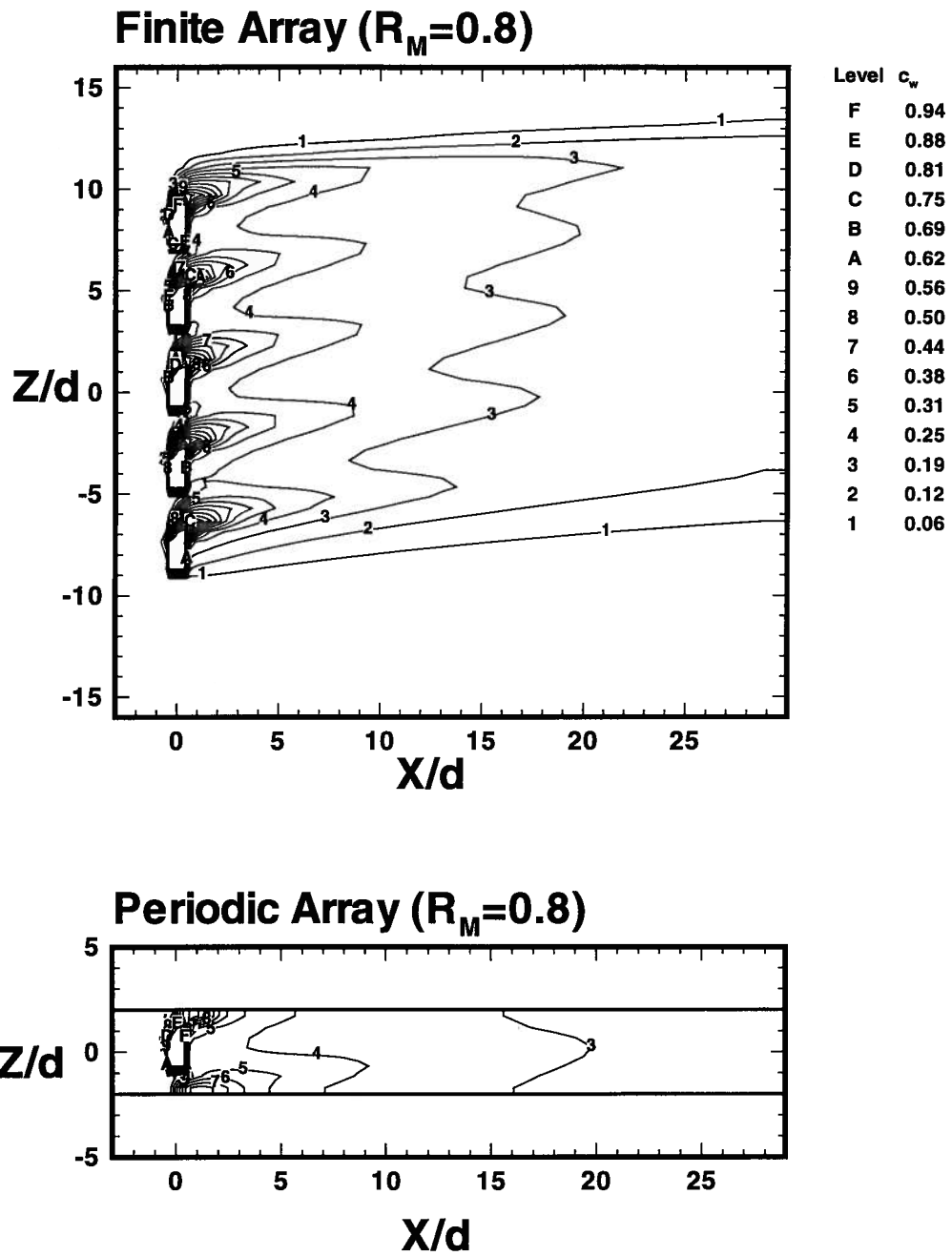
Figure 7.23: Predicted surface effectiveness of finite array and periodic array of lateral injection ($S/d = 4$, $R_M = 0.8$).

## Finite Array (R_M=1.2)

Level	c_w
F	0.94
E	0.88
D	0.81
C	0.75
B	0.69
A	0.62
9	0.56
8	0.50
7	0.44
6	0.38
5	0.31
4	0.25
3	0.19
2	0.12
1	0.06

Periodic Array (R_M=1.2)
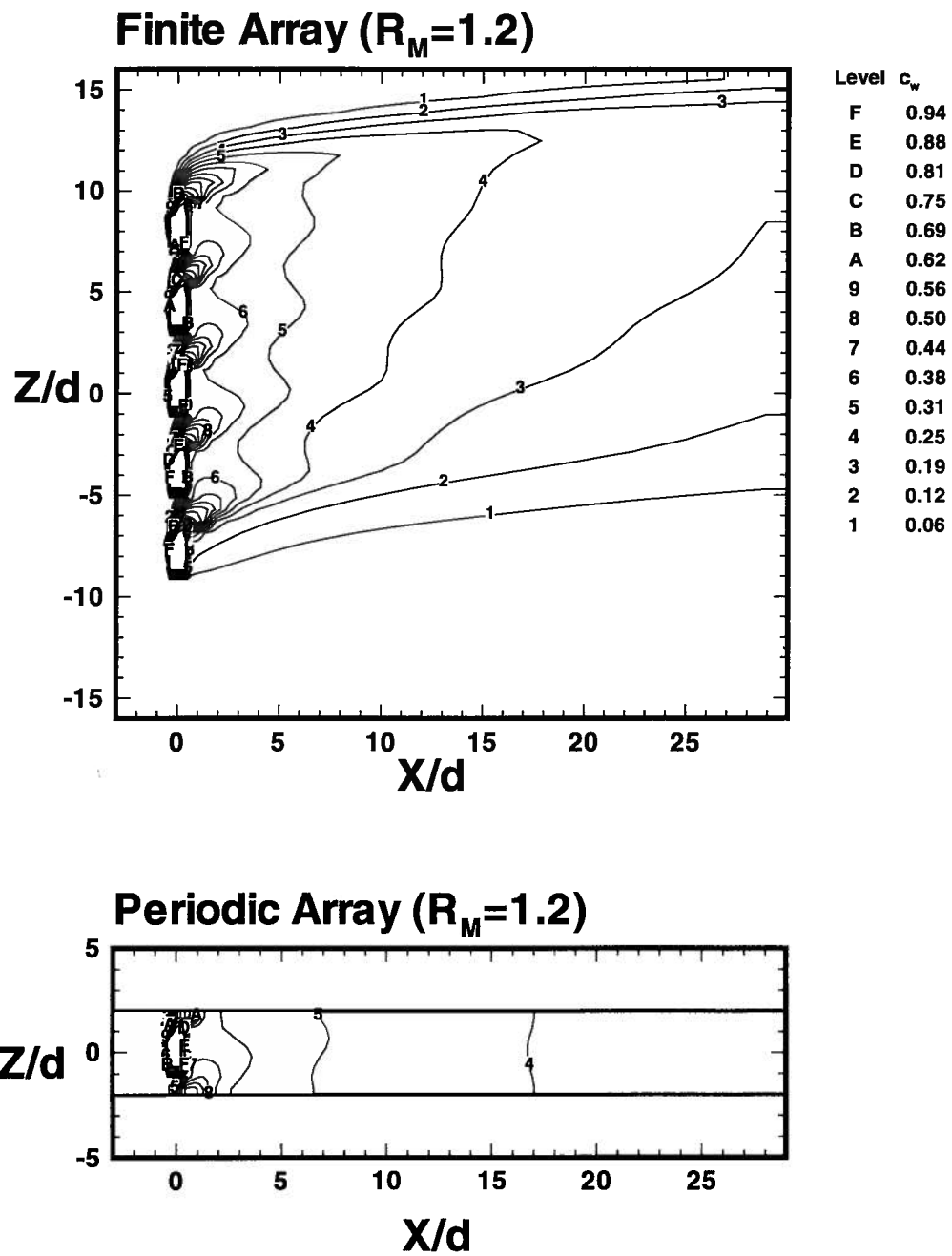
Figure 7.24: Predicted surface effectiveness of finite array and periodic array of lateral injection ($S/d = 4$, $R_M = 1.2$).
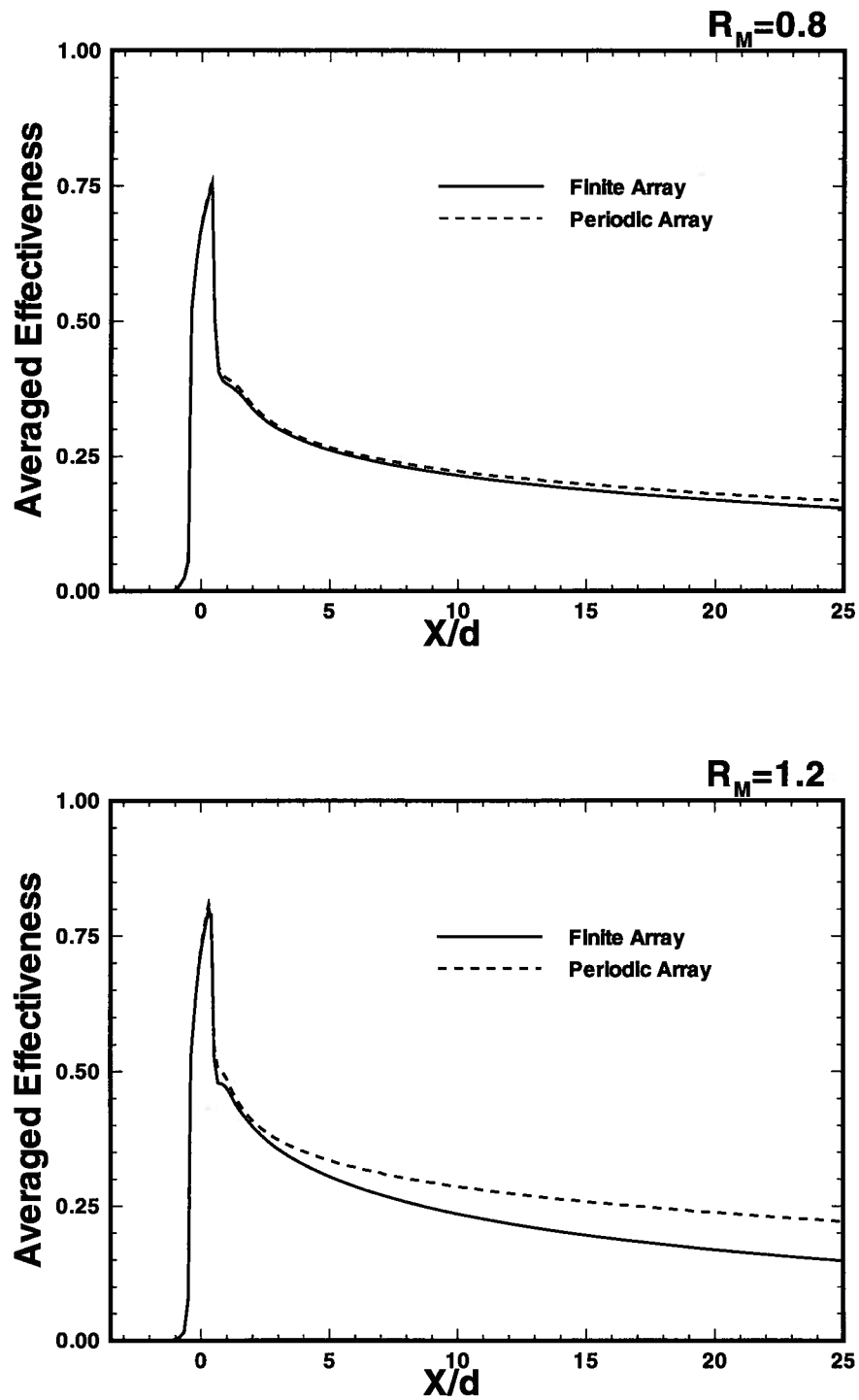
Figure 7.25: Predicted lateral averaged cooling effectiveness of finite array and periodic array of lateral injection ($R_M = 0.8$ and 1.2, $S/d = 4$).
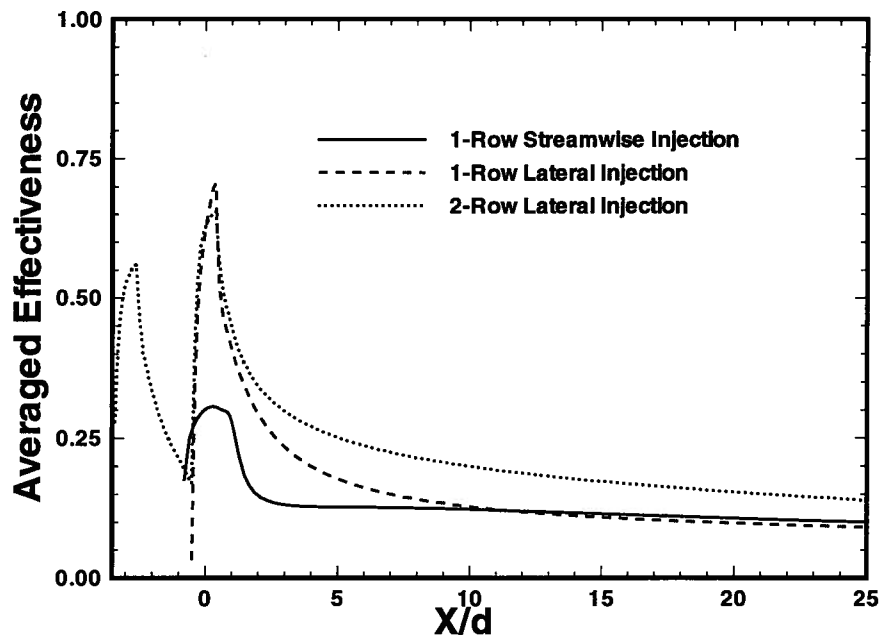
Figure 7.26: Predicted averaged cooling effectiveness by streamwise and lateral injection $(R_M = 0.4,\ S/d = 4)$.
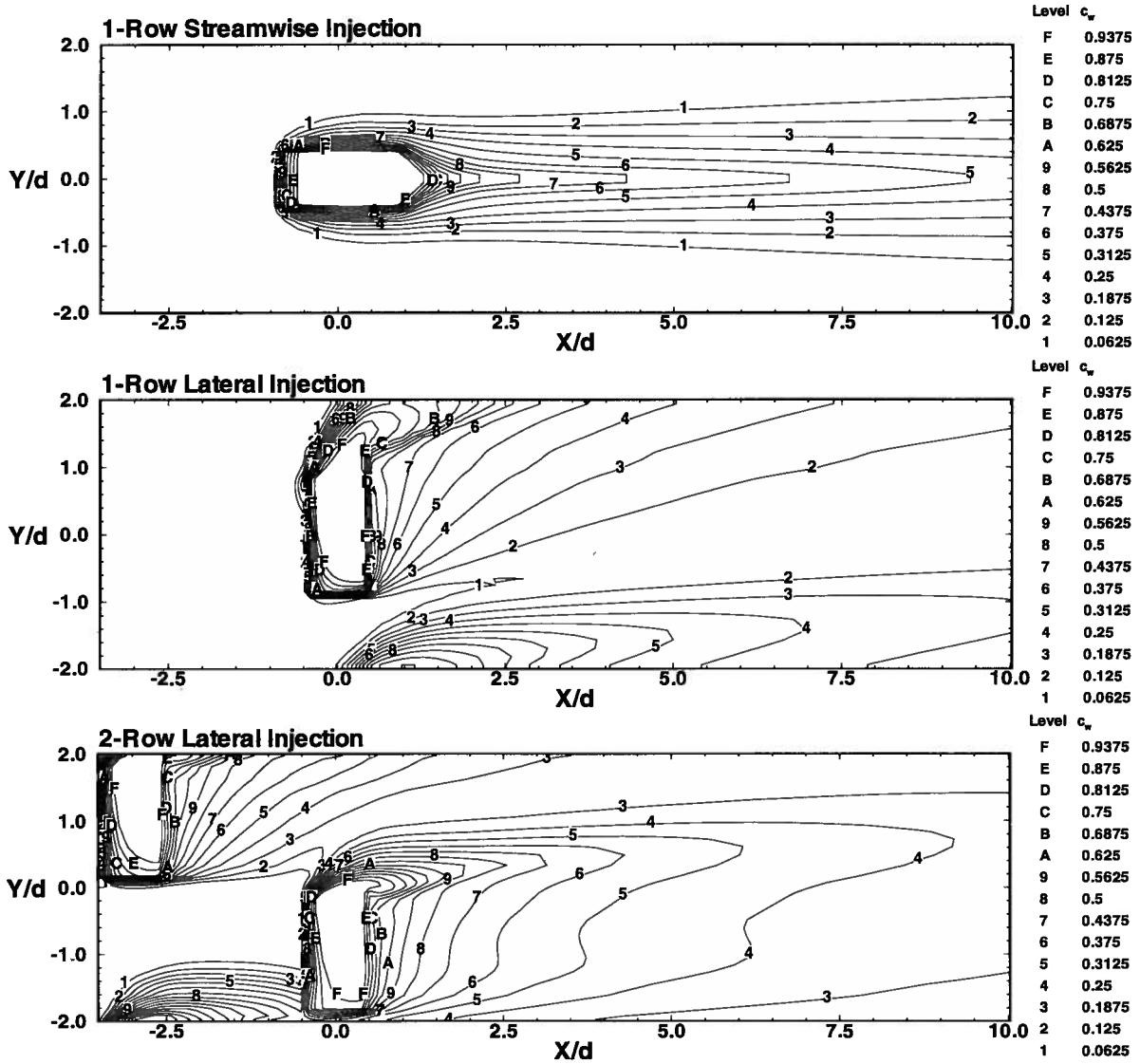
Figure 7.27: Predicted surface effectiveness by streamwise and lateral injection ($R_M = 0.4$, $S/d = 4$).
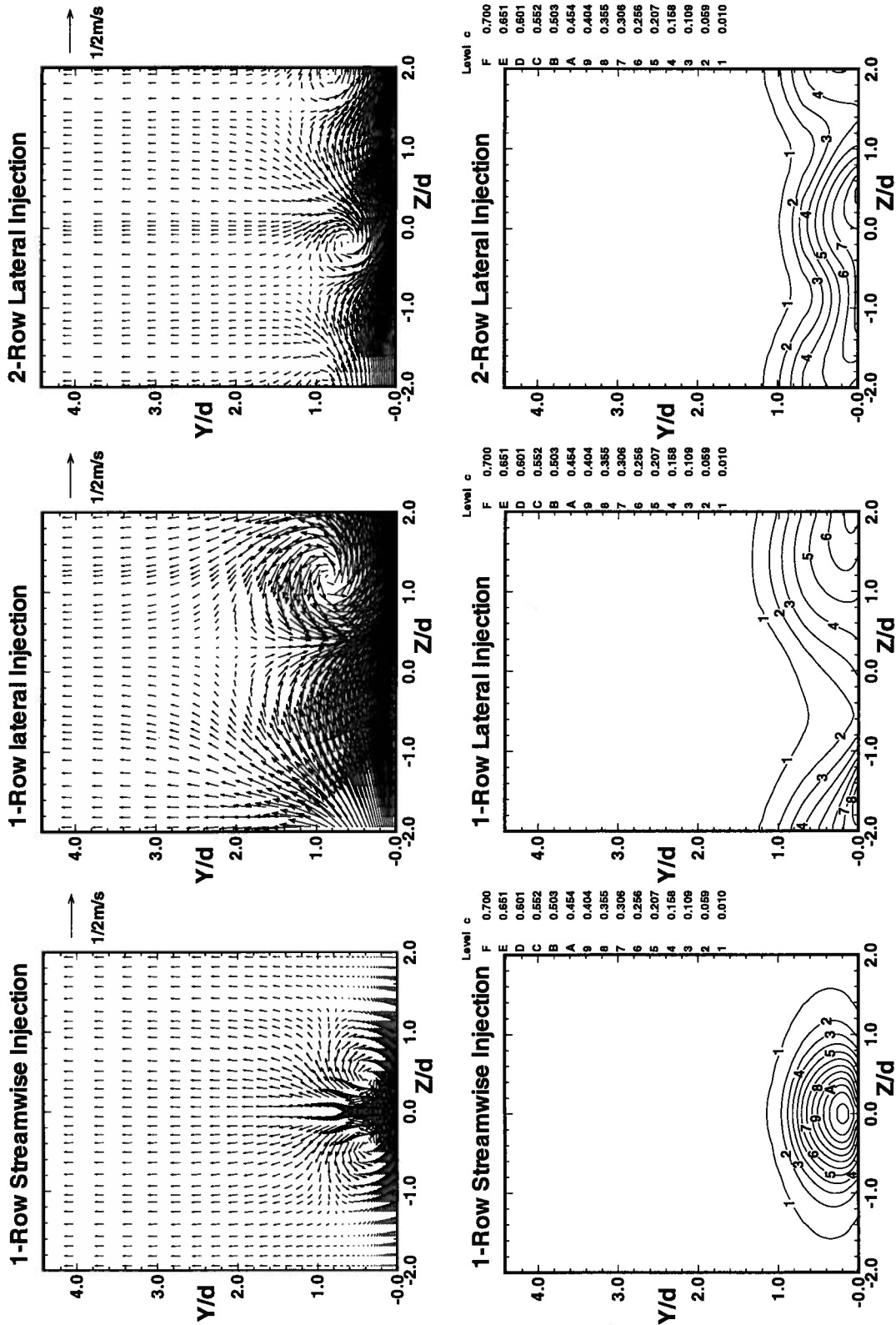
Figure 7.28: Vector fields and concentration distributions at $X/d = 3$ predicted by streamwise and lateral injection ($R_M = 0.4$, $S/d = 4$).
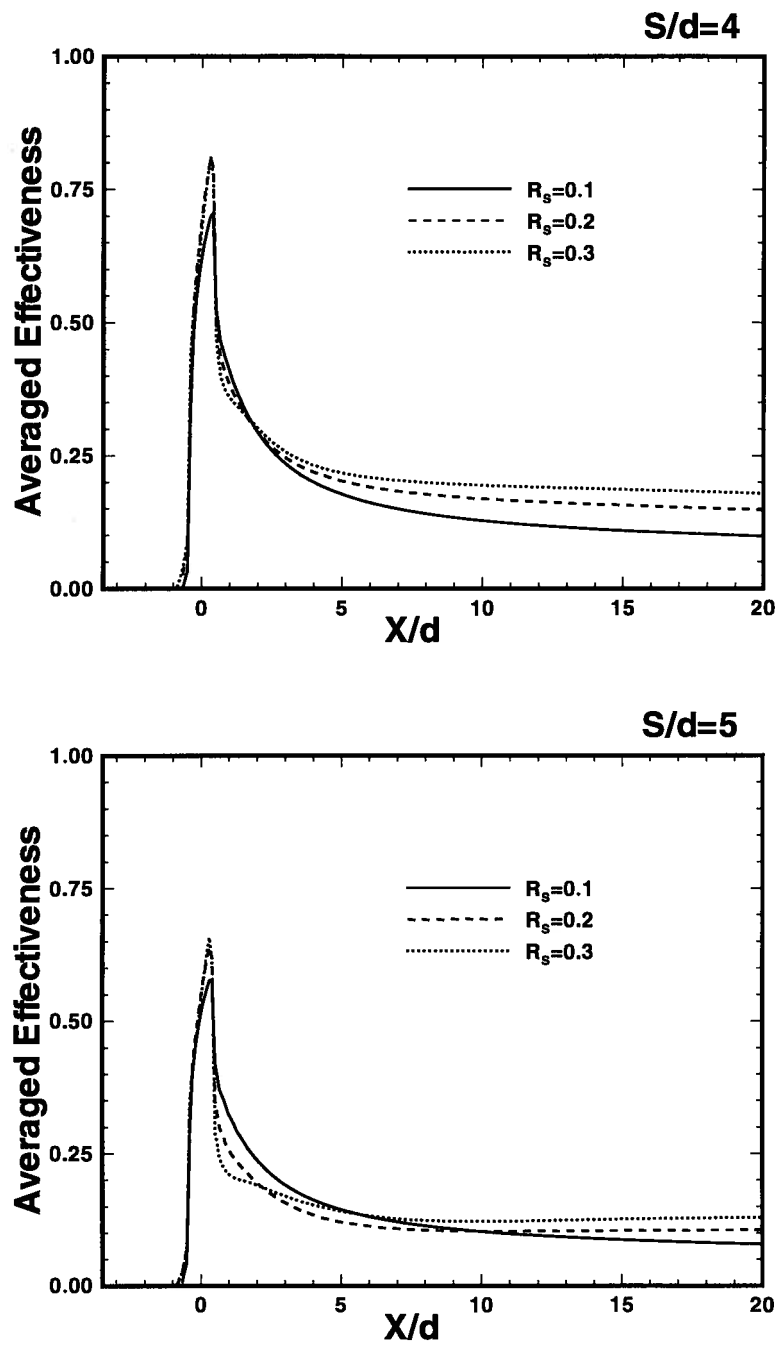
Figure 7.29: Predicted averaged cooling effectiveness vs. X/d for $S/d = 4$ and 5.
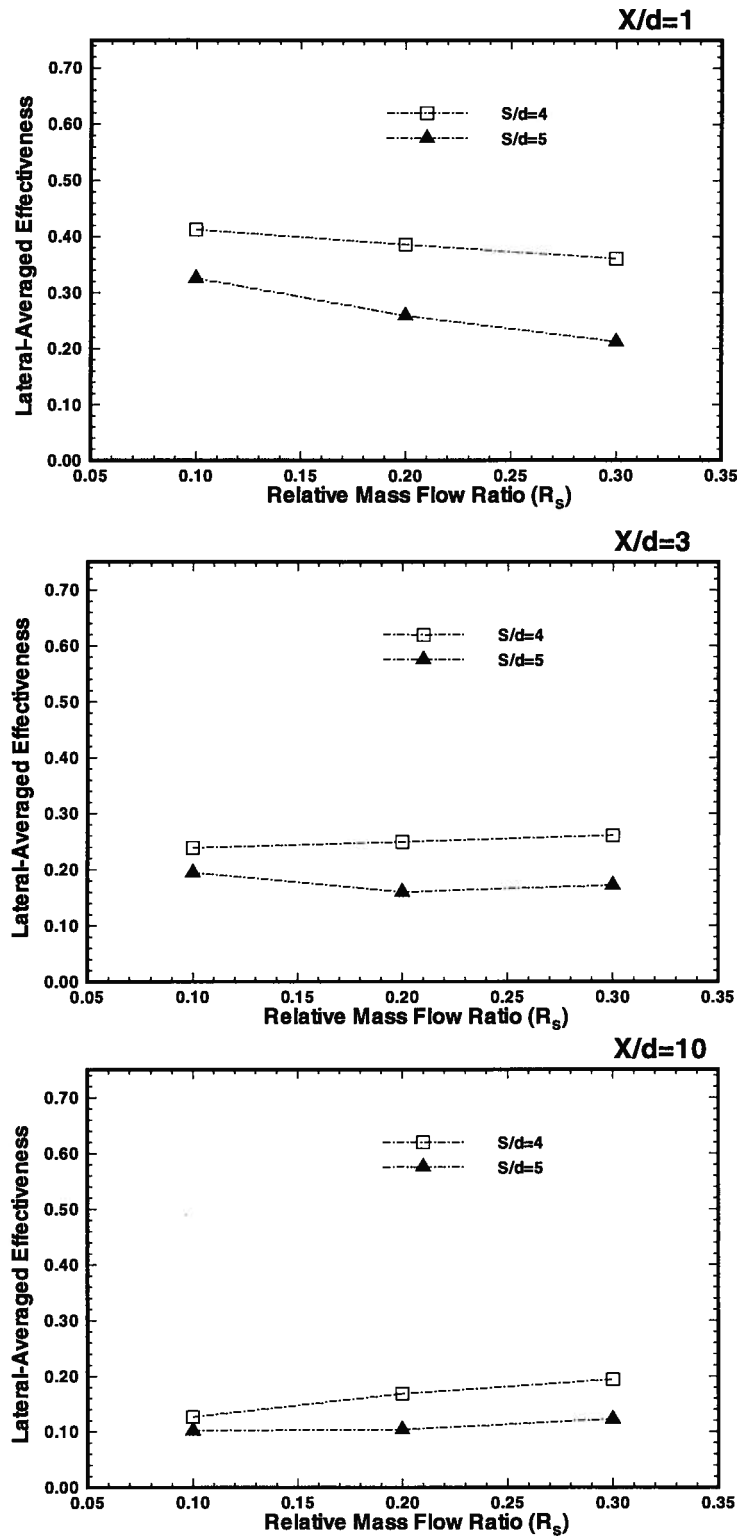
Figure 7.30: Predicted averaged cooling effectiveness vs. R_S ($S/d = 4$ and 5).
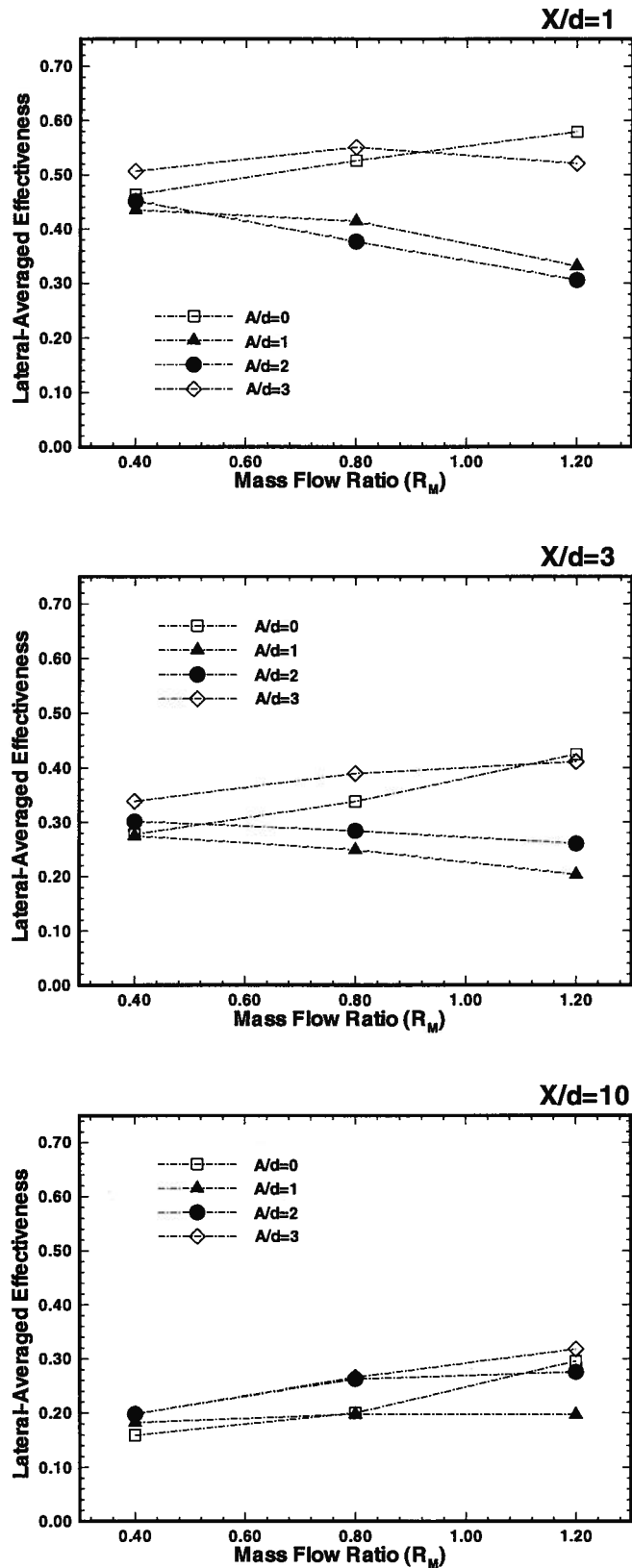
Figure 7.31: Predicted averaged cooling effectiveness vs. mass flow rate R_M.
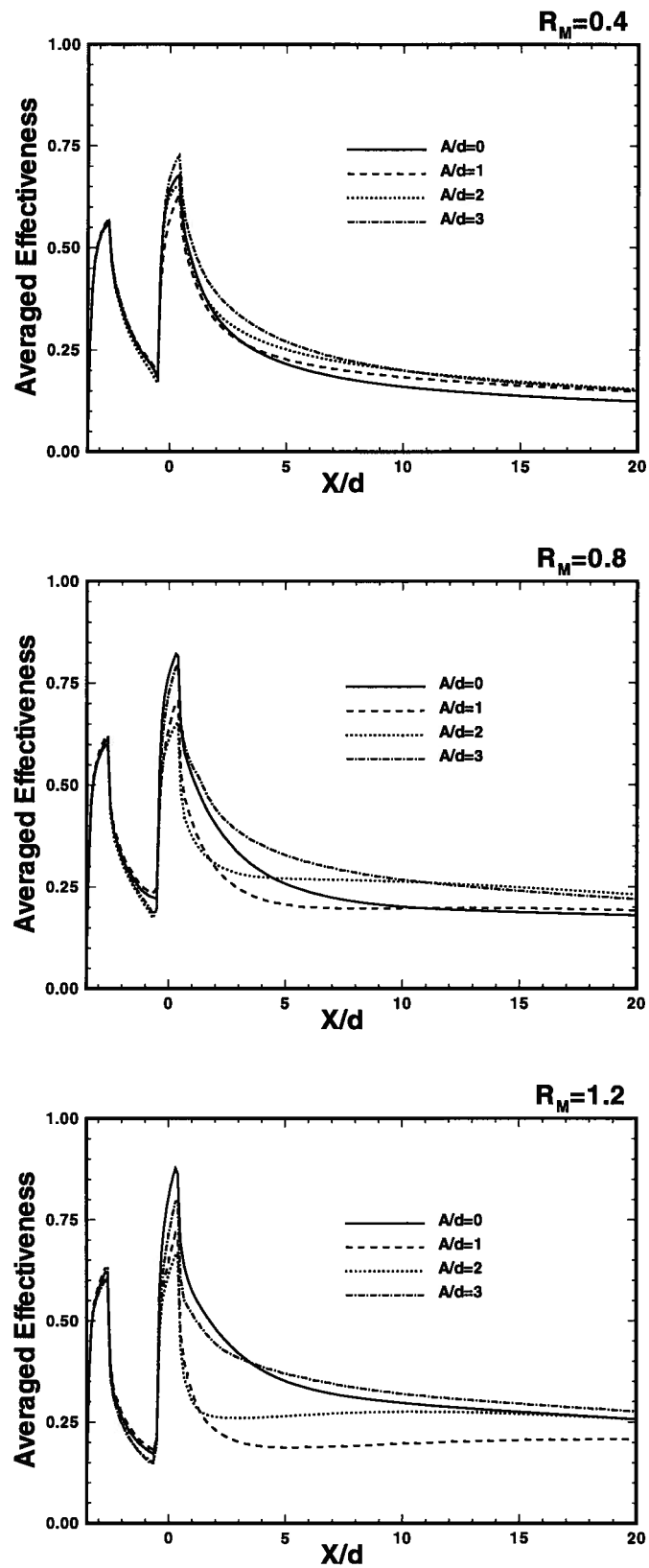
Figure 7.32: Predicted averaged cooling effectiveness vs. X/d.
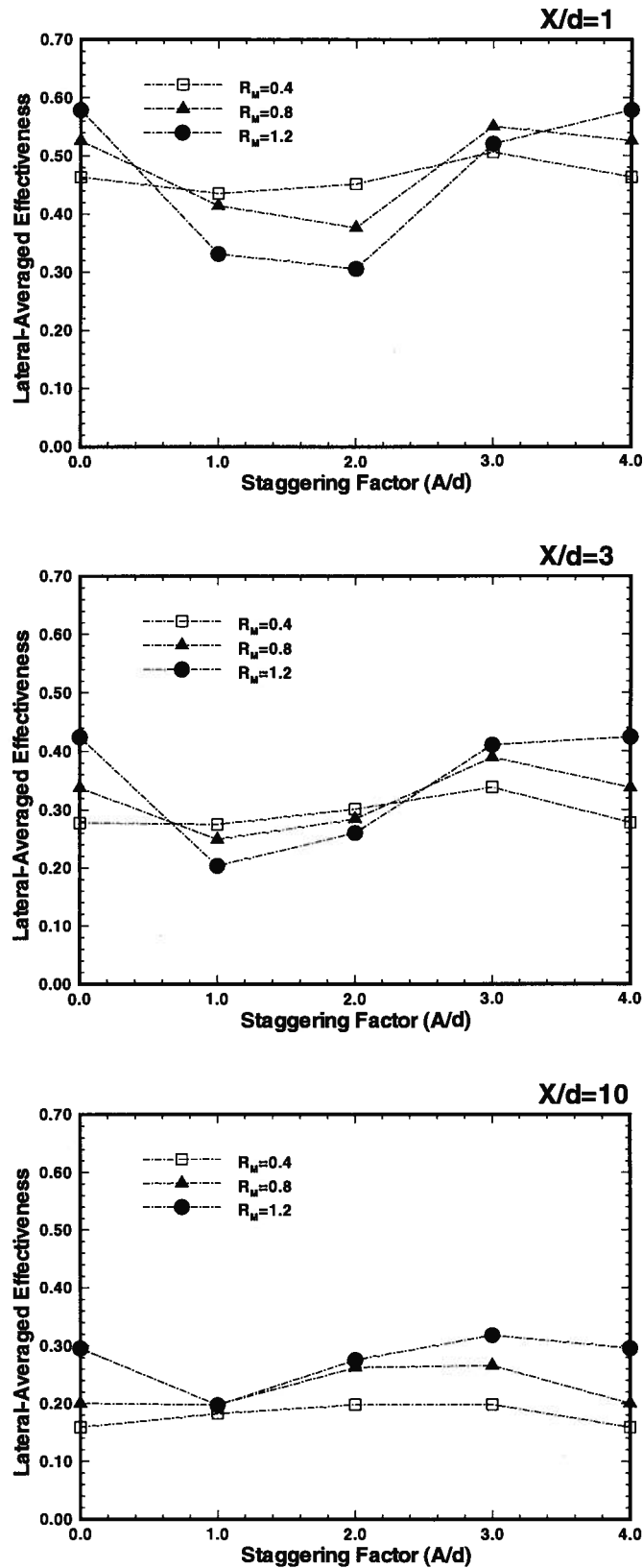
Figure 7.33: Predicted averaged cooling effectiveness vs. stagger factor A/d.

Chapter 8
Conclusions and Recommendations

Experimental and computational work have been carried out for two-dimensional and three-dimensional film cooling. The film cooling effectiveness, mean flow, and turbulence were measured in the wind tunnel based on the heat-mass transfer analogy using the flame ionization detector and hot-wire anemometry. The numerical models are assessed by using the new experimental data. In the present computations, the flow and the associated heat transfer are resolved using grid refinement. The converged refined-grid solutions are obtained efficiently by using the multi-grid method. The numerical model uses improved turbulence models in order to take into account the non-equilibrium of the turbulence, viscosity affected near-wall turbulence, and the nonisotropic turbulence, none of which are considered in the traditional modelling approach of the k-ε model with a wall function. The present investigation of the simplified 2-D and 3-D film cooling models has illustrated the deficiency of traditional turbulence modelling approaches and has presented a computational method suitable for real geometries in film cooling.

In the 2-D computation, the M-T-S model combined with the LK treatment shows the best agreement with the experiments. As the mass flow rate increases, the improvement of the present model over the traditional approach using the k-ε model with a wall function is significant. It is necessary to use the LK treatment with a near-wall refined grid in order to predict accurately the flow and heat transfer, thus the effectiveness. However, it is found that within the separation bubble the LK treatment cannot predict the increased mixing due to the separation. The disagreement between the measured and computed effectiveness suggests that the extra mixing created by the unsteadiness in the actual flow near reattachment is not well represented with the present modelling.

132

Comparisons between experiments and computations of the 3-D case show good agreement at low mass flow ratios. However the agreement deteriorates at higher mass flow ratios due to deficiencies in the turbulence modeling. There is a need for an improved definition of the Reynolds stresses in order to reflect the increased turbulence generation and subsequent increased diffusion observed in the experimental results. It is important to note that for three-dimensional complex flows, there is a need for an improved definition of the Reynolds stresses, which can not be represented by the isotropic assumption in the k-ε models. Consideration should also be given to the unsteady nature of the separation and reattachment of the flow. The algebraic turbulent stress model and the multi-time scale model may improve the modeling of turbulence in 3-D film cooling flow.

Parametric studies have been carried out in order to understand the flow phenomena in the film cooling process. Film cooling through single and double rows of holes with streamwise and spanwise injection have been presented. The superior performance of lateral injection, mainly near the coolant orifices has been illustrated and discussed. It was shown that lower jet penetration and a favorable interaction of vortices produced by the jets issuing from the two rows of holes are responsible for the superior performance of the lateral injection near the holes. For double-row injection, consistently better performance of the arrangement with staggering factor *A/d=3* for two rows of holes is found for the range of parameters investigated. Such behavior is observed in experimental work on a more realistic turbine model (Gartshore et al., 1993).

Some recommendations are made as follows:

1) Experimental data in the near-wall and injection exit regions are needed to guide the turbulence modelling of these regions. Non-intrusive measurements using laser Doppler velocimetry (LDV) and particle image velocimetry (PIV) are suggested in order to obtain detailed data of mean velocity and turbulent

shear stresses in the 3-D flow field. Measurements of wall shear stress and local pressure distribution on the wall surface are also suggested.

2) Computations of more complex geometries, such as injection through circular orifices and curved surfaces which are present near the leading edge of real turbine blades, should be carried out using the present numerical model with the Navier-Stokes solver on a curvilinear coordinate system.

3) The multiple-time scale model should be introduced into the 3-D simulations to improve the prediction of effectiveness at high mass flow ratios where the nonequilibrium turbulence is significant. The algebraic Reynolds stress model or the full Reynolds stress model should also be used to handle the turbulent mixing and transport in the flow with swirling flow, pressure gradients, and strong streamline curvature. Also, an appropriate near-wall turbulence treatment to represent the increased mixing occurring in the separation bubble should be further investigated.

4) The present results show that the vertical jet film cooling arrangement constitutes a severe test for discretization schemes as well as turbulence models and near-wall turbulence treatments. In both cases, inadequacies appear to be magnified as a result of the high streamline curvature and large gradients in the flow field. These features, as well as the simple uniform flow upstream boundary condition, suggest the adoption of this flow configuration as a benchmark test for numerical methods and turbulence models.

References

[1] A.A. Amer and B.A. Jubran and M.A. Hamdan (1992), "Comparison of different two-equation turbulence models for prediction of film cooling from two rows of holes," *Numerical Heat Transfer*, Part A, Vol. 21, pp. 143-162.

[2] U.M. Ascher, H. Chin, and S. Reich (1994), " Stabilization of DAEs and invariant manifolds", *Numer. Math.*, Vol. 67, pp. 131-149.

[3] G. Bergeles, A.D. Gosman, and B.E. Launder (1976a), "The near-field character of a jet discharged normal to a main stream," *J. Heat Transfer*, pp. 373-378.

[4] G. Bergeles, A.D. Gosman, and B.E. Launder (1976b), "The prediction of three-dimensional discrete-hole cooling processes, part 1: Laminar flow," *J. Heat Transfer*, pp. 379-386.

[5] G. Bergeles, A.D. Gosman, and B.E. Launder (1978), "The turbulent jet in a cross stream at low injection rates: A three-dimensional numerical tTreatment," *Numerical Heat Transfer*, Vol. 1, pp. 217-242.

[6] G. Bergeles, A.D. Gosman, and B.E. Launder (1981), "The prediction of three-dimensional discrete-hole cooling processes, part 2: Turbulent flow", *J. Heat Transfer*, Vol. 103, pp. 141-145.

[7] A. Brandt (1977), "Multi-level adaptive solutions to boundary-value problems", *Math. Comp.*, Vol. 31, No. 138, pp. 333-390.

[8] A. Brandt (1980), "Multi-level adaptive computations in fluid dynamics", *AIAA J.*, Vol. 18, No. 10, pp. 1165-1172.

[9] J.W. Dally, W.F. Riley, and K.G. McConnel (1984), "Instrument for engineering measurement," John Wiley & Sons, Inc.

[10] A.O. Demuren (1985), "False diffusion in three-dimensional flow calculation", *Computers & Fluids*, Vol. 13, No. 4, pp. 411-419.

[11] A.O. Demuren, W. Rodi, and B. Schonung (1986), "Systematic study of film cooling with a three-dimensional calculation procedure", *Journal of Turbomachinery*, Vol. 108, pp. 124-130.

[12] A.O. Demuren (1990), "Calculation of 3d turbulent jets in crossflow with a multigrid method and a second-moment closure model", *Engineering Turbulence Modelling and Experiments*, Elsevier Science Publishing Co., Inc., pp. 155-159.

[13] N. Djilali (1987), "An Investigation of Two-Dimensional Flow Separation with Reattachment," Ph.D. Thesis, Department of Mechanical Engineering, the University of British Columbia, Canada.

[14] E.R.G. Eckert (1984), "Analysis of film cooling and full coverage film cooling of gas turbine blades," *J. of Eng. for Gas Turbines and Power*, Vol. 106, pp. 206-213.

[15] R. Eckert and R.M. Drake, Jr.(1987), *Analysis of Heat and Mass Transfer*, hpc.

[16] J.E. Fackrell (1980), "A flame ionization detector for measuring fluctuating concentration", *J. of Phys. E: Sci. Inst.*, Vol. 13, pp. 888-893.

[17] J.H. Ferziger (1987), "Simulation of incompressible turbulent flows", *J. Comp. Phy.*, Vol. 69, pp. 1-8.

[18] N.W. Foster and D. Lampard (1980), "The flow and film cooling effectiveness injection through a row of holes", *Journal of Engineering for Power*, Vol. 102, pp. 584-588.

[19] I.S. Gartshore, M. Salcudean, Y. Barnea, K. Zhang, and F. Aghadasi (1993), "Some effects of coolant density of film cooling effectiveness", ASME 93-GT-76.

[20] R.J. Goldstein, E.R.G. Eckert, V.L. Eriksen, and J.W. Ramsey (1970), "Film cooling following injection through inclined circular tubes", *Israel Journal of Technology*, Vol. 8, pp. 145-154.

[21] R.J. Goldstein and E.R.G.Eckert (1974), "Effects of hole geometry and density on three-dimensional film cooling", *Int. J. Heat Transfer*, Vol. 107, pp. 595-607.

[22] R.J. Goldstein (1971), "Film cooling," *Advances in Heat Transfer*, pp. 321-379.

[23] R.J. Goldstein, Y. Kornblum, and E.R.G. Eckert (1982), "Film cooling effectiveness on a turbine blade", *Israel Journal of Technology*, Vol. 20, pp. 193-200.

[24] W. Haas, W. Rodi, and B. Schonung (1991), "The influence of density difference between hot and coolant gas on film cooling by a row of holes: predictions and experiments", *ASME 91-GT-255*.

[25] S. Honami, T. Shizawa, A. Uchiyama, and M. Yamamoto (1991), " An experimental study of film cooling in the lateral injection", 91-Yokohama-IGTC-30.

[26] W.P. Jones and B.E. Launder (1972), "The prediction of laminarization with a two-equation model of turbulence", *Int. J. Heat Mass Transfer*, Vol. 15, pp. 301-314.

[27] B.A. Jubran and A. Brown (1985), "Film cooling from two rows of holes inclined in the streamwise and spanwise directions", *J. Engr. Gas Turbine Power*, Vol. 107, pp. 85-91.

[28] B.A. Jubran (1989), "Correlation and prediction of film cooling from two rows of holes", *J. Turbomachinery*, Vol. 111, pp. 502-509.

[29] B.E. Launder and D.B. Spalding (1974), "The numerical computation of turbulence flow", *Comp. Meths. Appl. Mech. Engng.*, Vol. 3, pp. 263-289.

[30] B.E. Launder, G.J. Reece, and W. Rodi (1975), " Progress in the development of a Reynolds-stress turbulence closure," J. Fluid Mech., vol. 68, pp. 566-570.

[31] S.-W. Kim and C.-P. Chen (1989), "A multiple-time-scale turbulence model based on variable partitioning of the turbulent kinetic energy spectrum", *Numerical Heat Transfer*, Part B, Vol. 16, pp. 193-211.

[32] S.-W. Kim (1991), "Calculation of divergent channel flows with a multiple-time-scale turbulence model", *AIAA Journal*, Vol. 29, No. 4, pp. 547-554.

[33] S.-W. Kim and T.J. Benson (1993), "Fluid flow of a row of jets in crossflow - a numerical study", *AIAA Journal*, Vol. 31, No. 5, pp. 806-811.

[34] J.H. Leylek and R.D. Zerkle (1993), "Discrete-jet film cooling: A comparison of computational results with experiments", ASME 93-GT-207.

[35] P.M. Ligrani, S. Ciriello, and D.T. Bishop (1992), "Heat transfer, adiabatic effectiveness, and injectant distributions downstream of a single row and two staggered rows of compound angle film cooling holes", *J. of Turbomachinery*, Vol. 114, pp. 687-700.

[36] S. McCormick (1989), "Multilevel adaptive methods for partial differential equations", SIAM.

[37] A.B. Mehendale and J.C. Han (1992), "Influence of high mainstream turbulence on leading edge film cooling heat transfer: effect of film hole spacing", *J. of Heat Mass Transfer*, Vol. 135, pp. 2593-2604.

[38] R.J. Moffat (1986), "Turbine blade cooling," *Heat Transfer and Fluid Flow in Rotating Machinery*, pp. 1-26.

[39] Y. Nagano and M. Tagawa (1990), "An improved k-ε model for boundary layer flows", *Journal Fluids Engineering*, Vol. 113, pp. 33-39.

[40] P. Nowak (1991), "3-D segmented multi-grid computing code", *Technical Report*, Department of Mechanical Engineering, UBC, Canada.

[41] S.V. Patankar, A.K. Rastogi, and J.H. Whitelaw (1973), "The effectiveness of three-dimensional film cooling slots - II. predictions," *Int. J. Heat Mass Transfer*, Vol. 16, pp. 1665-1681.

[42] S.V. Patankar, D.K. Basu, and S.A. Alpay (1977), "Prediction of the three-dimensional velocity field of a deflected turbulent jet," *Journal of Fluid Engineering*, pp. 758-762.

[43] S.V. Patankar (1980), *Numerical Heat Transfer and Fluid Flow*, Hemisphere.

[44] W. Rodi (1984), *Turbulence Models and Their Application to Hydraulics - A State of the Art Review*.

[45] W. Rodi (1991), "Experience with two-layer models combining the k-ε with a one-equation model near the wall," *AIAA-91-0216*.

[46] M. Salcudean, Z. Abdullah, and P. Nowak (1992), "Mathematical modeling of recovery furnaces," *1992 International Chemical Recovery Conference*, Seattle, WA.

[47] M. Salcudean, I.S. Gartshore, K. Zhang, and I. McLean (1994a), "An experimental study of film cooling effectiveness near the leading edge of a turbine blade," *ASME Journal of Turbomachinery*, January.

[48] M. Salcudean, I.S. Gartshore, K. Zhang, and Y. Barnea (1994b), "Leading edge film cooling of a turbine blade model through single and double row injection: Effects of coolant density", to be presented at ASME IGTCE, June 1994, The Hague, Holland.

[49] P. Sathyamurthy and S.V. Patankar (1990), "Prediction of film cooling with lateral injection", *Heat Transfer in Turbulent Flow*, pp. 61-70.

[50] B. Schonung and W. Rodi (1987), "Prediction of film cooling by a row of holes with a two-dimensional boundary-layer procedure," *ASME Journal of Turbomachinery*, Vol. 9, pp. 579-587.

[51] D. Sidilkover and U.M. Ascher (1994), "A multigrid solver for the steady state Navier-Stokes equations using the pressure-Poisson formulation," Technical Report 94-3, Department of Computer Science, the University of British Columbia, Canada.

[52] S.P. Vanka (1986), "Block-implicit multigrid solution of Navier-Stokes equations in primitive variables", *Journal of Computational Physics*, Vol. 65, pp. 138-158.

[53] A.J. White (1980), "The prediction of the Flow and Heat Transfer in the Vicinity of a Jet in Crossflow", ASME 80-WA/HT-26.

[54] D.C. Wilcox (1993), *Turbulence Modelling for CFD*, DCW Industries, Inc., La Canada, California.

[55] C. Yap (1987), *Turbulent Heat and Momentum Transfer in Recirculating and Impinging Flows*, Ph.D. thesis, University of Manchester, England.

[56] J.M. Zhou (1990), "A multi-grid computation of film cooling flow," *M.Sc. Thesis*, University of British Columbia, Canada.

[57] J.M. Zhou and M. Salcudean (1990), "A multi-grid local mesh-refinement method for recirculating flows", *Computational Fluid Dynamics*, M. Rahman ed.,

[58] J.M. Zhou, M. Salcudean, and I.S. Gartshore (1993a), "A numerical computation of film cooling effectiveness," *Near-Wall Turbulent Flows*, R.M.C. So, C.G. Speziale and B.E. Launder eds., Elsevier, pp. 377-386.

[59] J.M. Zhou, M. Salcudean, and I.S. Gartshore (1993b), "Prediction of film cooling by discrete-hole injection," ASME 93-GT-75.

[60] J.M. Zhou, M. Salcudean, and I.S. Gartshore (1994), "Application of the multiple-time scale turbulence modeling to the prediction of film cooling effectiveness," paper accepted by *the 10th International Conference of Heat Transfer*, August 1994, Brighton, England.

Appendices

A. Experimental Measurement Uncertainty Analysis

The experimental data used in the present study were obtained using FID, hot-wire anemometry, Pitot tubes, and flow meters. Uncertainties are expected in the measured data due to changes in the process over the time interval required to make the measurements, as well as errors introduced from the instrumentation system (Dally et al., 1984). The uncertainty analysis describes the error which may be present in the measured data.

A.1.   Effectiveness Measurement

The error in effectiveness measurement is mainly associated with the FID. In the present measurements, the output of the FID voltage, E, and the concentration of propane in air, C, has a linear relationship

$$C = \alpha(E - E_0) \tag{A.1}$$

where α is a calibration constant and E_0 is the voltage output of pure air. From the calibration (see Figure 3.5), the standard deviation of propane concentration S_C can be expressed as:

$$S_C = \sqrt{\frac{\sum_{i=1}^{N}(C - C_{reg})^2}{N}} \tag{A.2}$$

where N is the number of calibration points and C_{reg} is the concentration from the linear regression. The standard deviation was found as 3.2 ppm.

During the experiment, the propane concentration in the injection chamber, C_C, may change due to the instability involved in the supply of compressed air and propane. By adjusting two flowmeters of compressed air and propane, the relative fluctuation in

C_C, e_C, was controlled to within ±2.5%. Since the propane concentration in the pure air C_∞=0, the uncertainty in the effectiveness η (see Equation 3.1) can be calculated by only considering S_C and e_C

$$\frac{\delta\eta}{\eta} = \sqrt{\left(\frac{S_C}{C_C}\right)^2 + e_C^2} \tag{A.3}$$

$$\delta\eta = \sqrt{\left(\frac{S_C}{C_C}\eta\right)^2 + \left(e_C\eta\right)^2} \tag{A.4}$$

In the present work, C_C is about 150 ppm and η ranges from 0 to 1. Therefore, the uncertainty in effectiveness is less than ±3.29%.

A.2. Velocity Measurement

The error in velocity measurement is mainly associated with the hot-wire anemometry. In the present experiments, the output of the bridge voltage, E, and the fluid velocity, U, are related through the following equation at the calibration condition:

$$E^2 = A + BU^N \tag{A.5}$$

where A and B are calibration constants and $N=0.45$. During calibration, the hot-wire probe was calibrated against a Pitot tube manometer. The velocity was obtained from the equation

$$\frac{1}{2}\rho U^2 = \rho_{Al}gh \tag{A.6}$$

where ρ_{Al} is the density of alcohol and h is the vertical height of the alcohol column in the manometer. A scale of 1:10 inclination of the column was chosen in calibration. The reading from the column gave an accuracy of ±0.5 mm. Converting this accuracy to the vertical height scale gives the error from reading δh=±0.05 mm. By differentiating Equation A.6, the error in air velocity from the reading on the column scale is

$$\varepsilon_U = \frac{\partial U}{\partial h}\delta h = \sqrt{\frac{\rho_{Al}gh}{2\rho}}\frac{1}{\sqrt{h}}\delta h = \frac{\rho_{Al}g}{\rho U}\delta h \tag{A.7}$$

At the room temperature, say 20°C, ρ=1.164 kg/m³ and ρ_{Al}=806.6 kg/m³, this error can be simplified to

$$\varepsilon_U = \frac{0.34}{U} \tag{A.8}$$

The error is inversely proportional to air velocity. The velocity was calibrated over a range of 3.5~11.0 m/s, and the error with respect to these two limits is in a range from 0.031 m/s to 0.097 m/s.

Similar to Equation A.2, the standard deviation of air velocity regression S_U (see Figure 3.6) is 0.07m/s. Changes of room temperature during experiments were less than 2°C, and thus can be neglected. The velocity range in the measurements is from 2.0 m/s to 10.0 m/s, therefore the uncertaity in the velocity is ±6%.

The turbulence intensity $\sqrt{\overline{(u')^2}}$ is calculated through

$$\sqrt{\overline{(u')^2}} = \sqrt{\frac{\sum_{i=1}^{N}(u_i - U)^2}{N}} \tag{A.9}$$

where U is mean velocity of all sample velocities u_i ($i = 1, \ldots, N$) and N is the number of samples. The uncertaity in the intensity can be similarly calculated as ±6% in the environment with turbulence intensity less than 6%.

A.3. Mass Flow Ratio

In the experiments, the mainstream velocity was measured using the Pitot tube manometer and the injection flow was measured by the flowmeter. The mainstream velocity was 10 m/s in the experiments, therefore, using Equation A.8 the uncertainty in the mainstream velocity is 0.034 m/s. The uncertainty in the injection velocity from the flowmeter's reading error is ±4.7×10⁻³ m/s. The uncertainty in the mass flow ratio, R_M, can be obtained by the error propagation formula

$$\delta R_M = \sqrt{\left(\frac{\delta U_C}{U_\infty}\right)^2 + \left(\frac{U_C}{U_\infty^2}\delta U_\infty\right)^2} = \sqrt{\left(\frac{\delta U_C}{U_\infty}\right)^2 + \left(R_M\frac{\delta U_\infty}{U_\infty}\right)^2} \qquad (A.10)$$

In the present experiment, R_M varies from 0.2 to 0.8, therefore the uncertainty in R_M is

$$\frac{\delta R_M}{R_M} = \pm 0.41\% \qquad (A.11)$$

B. Detailed Flow and Effectiveness Distributions

B.1. Spanwise Hole Spacing Effects in Single-Row Film Cooling

Figure B.1 and B.2 show the detailed surface cooling effectiveness distribution. Figure B.3 and B.4 show the vector field and concentration contour in a cross flow plane at $X/d=3$ of a single-row lateral injection for $X/d=4$ and 5.

B.2. Hole Staggering Effects in Double-Row Film Cooling

The detailed surface cooling effectiveness distributions are shown in Figures B.5-B.10. Figures B.11-B.16 show the vector fields and concentration contours in a cross-flow plane at $X/d=3$ for $A/d=0, 1, 2, 3$. It is found that two vortices from both front $(X/d=0)$ and back $(X/d=-3)$ rows merge forming a single vortex, except at $A/d=2$ (fully staggered) where two vortices are still visible. However, as R_M increases to 1.2, two vortices merge before $X/d=3$.

For different hole arrangements, the interaction between the vortices from front and back rows results in different lateral momentum, which can be observed by the position of the vortex. The lateral momentum in the direction of the injection pushes the cooler fluid back to the surface. Table B.1 shows the location of the vortex center measured from the front hole center and the circulation of positive vorticity Γ over the area of the cross section $(-2<Z/d<2, 0<Y/d<4)$ at $X/d=3$, where $\Gamma = \iint\limits_{Area}\left(\dfrac{\partial V}{\partial Z} - \dfrac{\partial W}{\partial Y}\right)ds$. It is found that $A/d=3$ gives consistently higher lateral movement than other arrangements. There is no clear evidence on the effect of the circulation on the effectiveness.

Table B.1: Location and circulation of vortices downstream of injection (X/d=3).

R_M	A/d	X/d=3	
		Location (Z/d,Y/d)	Circulation (m²/s)
0.4	0	*(1.1, 0.7)*	4.46×10^{-3}
	1	*(0.8, 0.6)*	4.69×10^{-3}
	2	*(0.8,0.6)&(0.9,0.9)*	3.39×10^{-3}
	3	*(1.9, 0.9)*	4.22×10^{-3}
0.8	0	*(0.9, 0.8)*	1.34×10^{-2}
	1	*(1.35, 0.8)*	1.21×10^{-2}
	2	*(1.3,0.8)&(1.5,1.3)*	8.69×10^{-3}
	3	*(2.4, 1.0)*	1.02×10^{-2}
1.2	0	*(3.0, 1.15)*	1.88×10^{-2}
	1	*(1.95, 1.1)*	2.07×10^{-2}
	2	*(1.7, 1.15)*	1.20×10^{-2}
	3	*(3.1, 1.2)*	1.63×10^{-2}
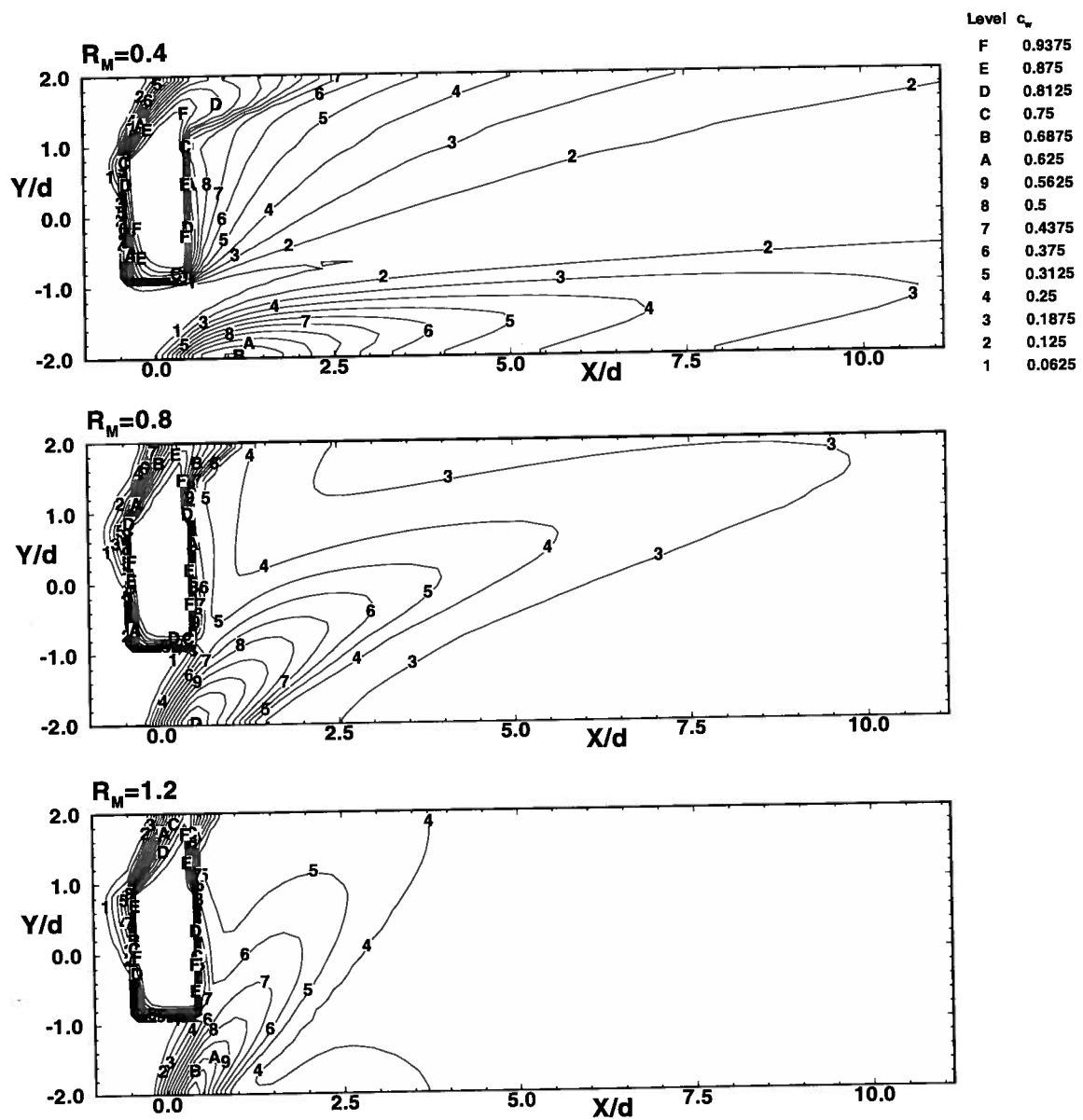
Figure C.1: Predicted surface cooling effectiveness (1-Row injection, $S/d = 4$).
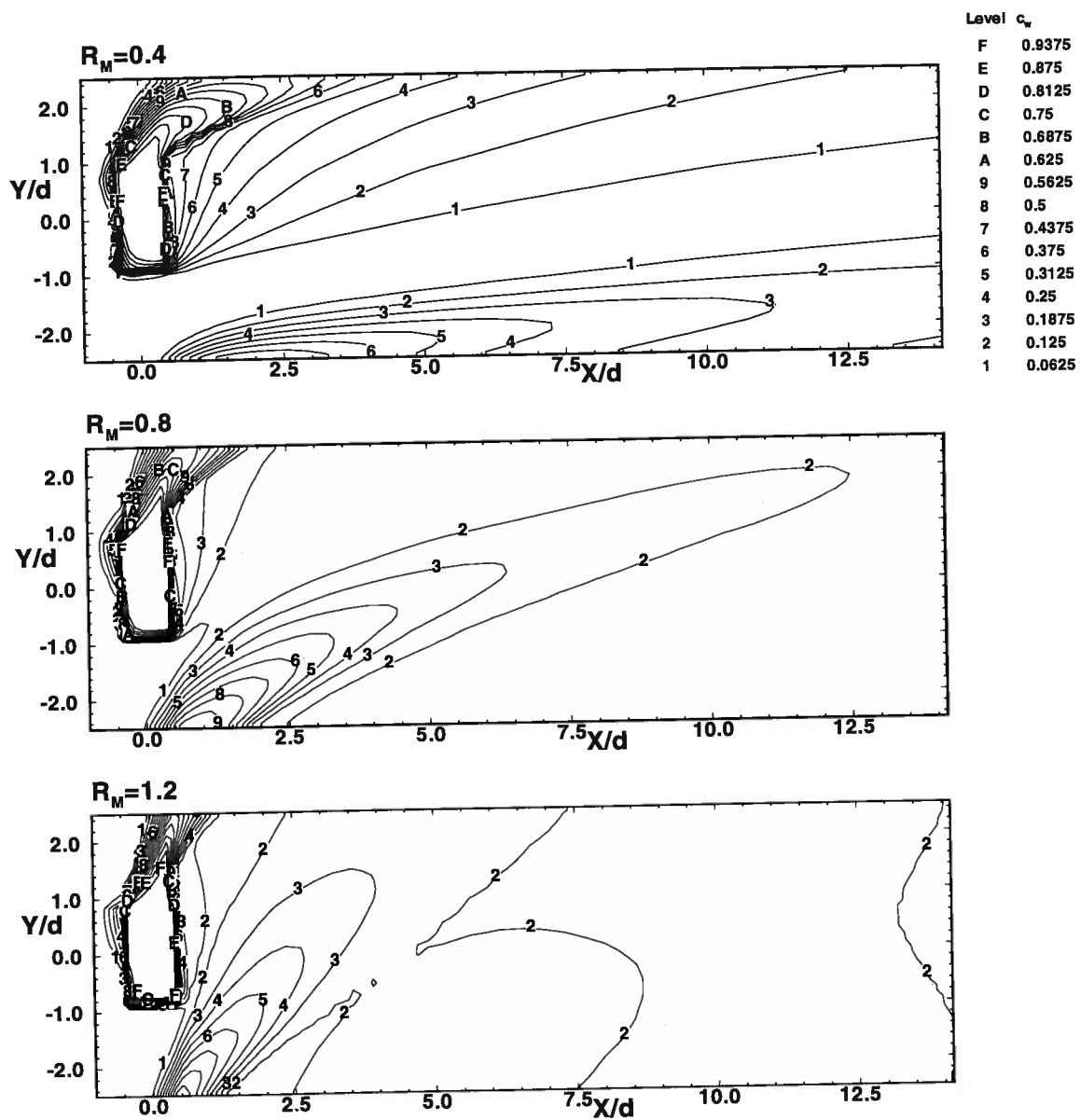
Figure C.2: Predicted surface cooling effectiveness (1-Row injection, $S/d = 5$).
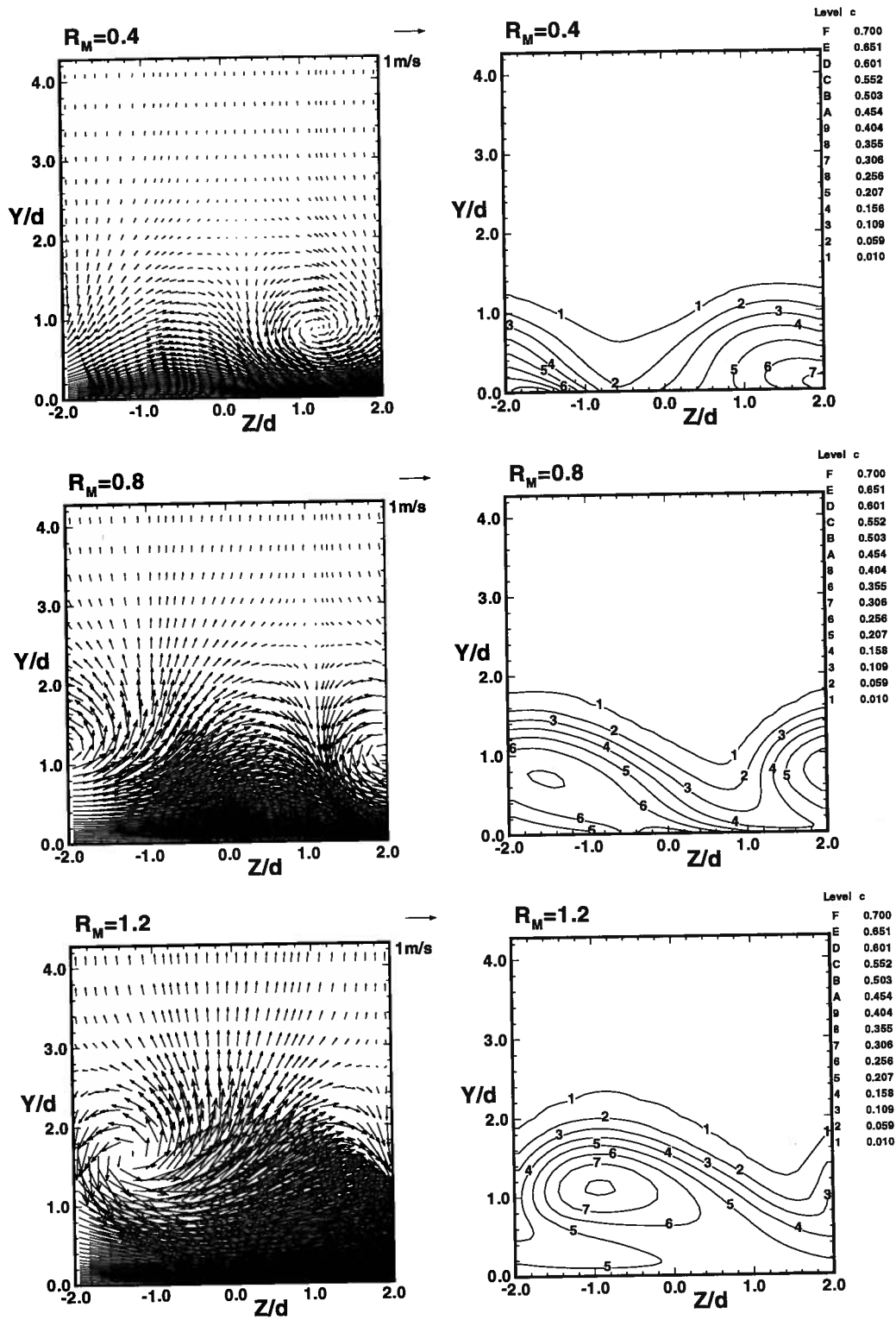
Figure C.3: Predicted vector fields and concentration distributions at $X/d = 3$ (1-Row injection, $S/d = 4$).
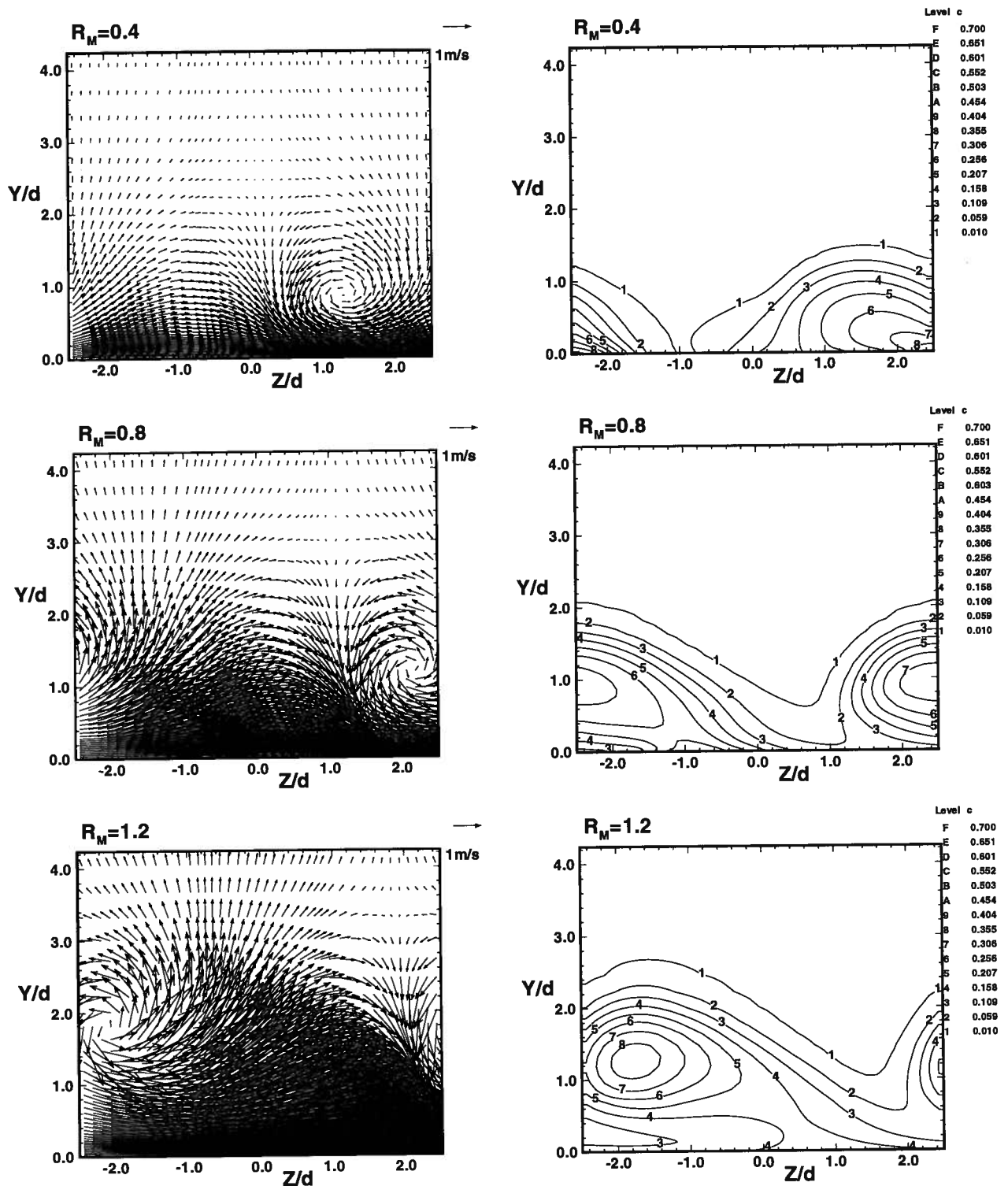
Figure C.4: Predicted vector fields and concentration distributions at $X/d = 3$ (1-Row injection, $S/d = 5$).
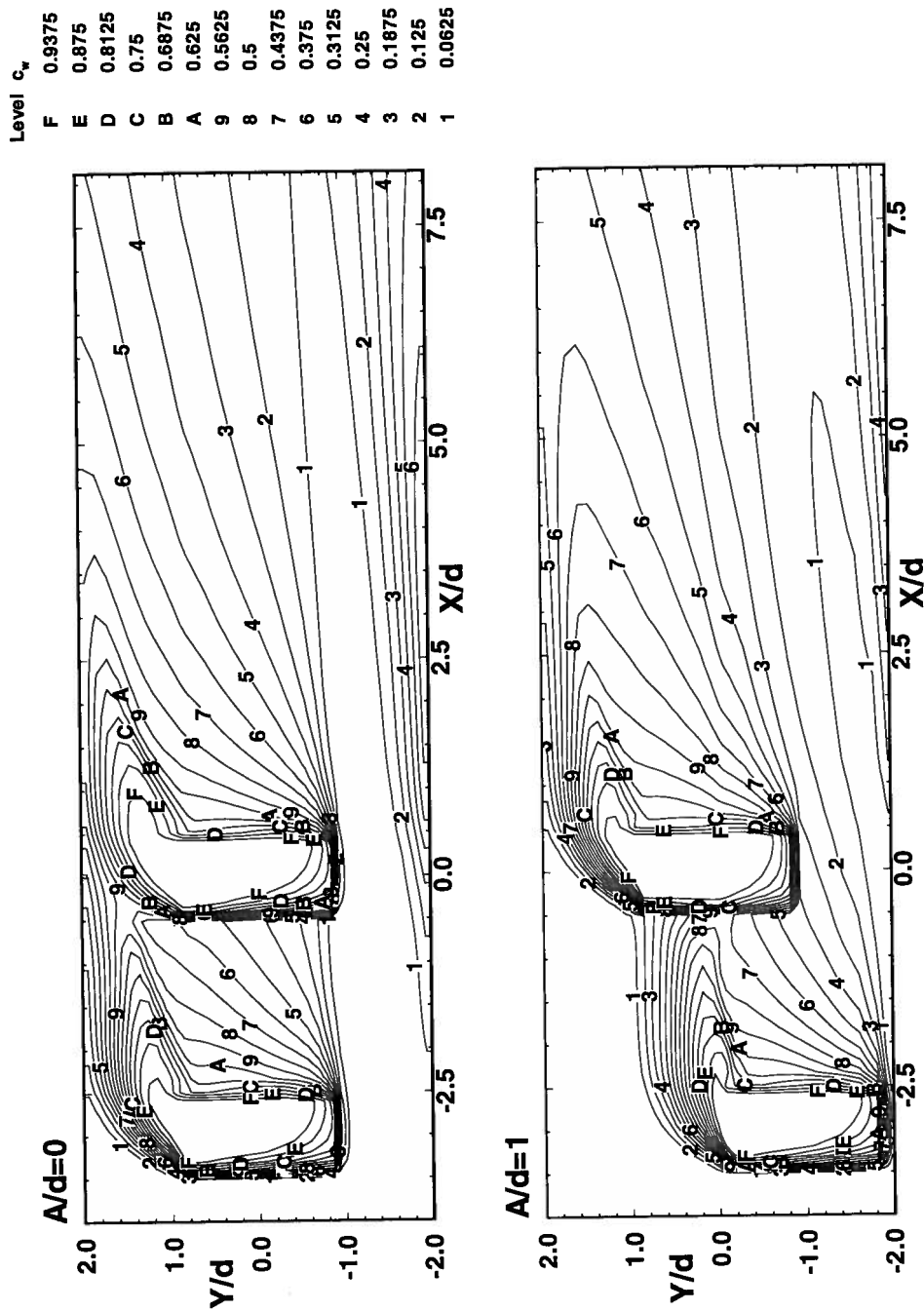
Figure C.5: Predicted surface film cooling effectiveness ($A/d = 0, 1$, $R_M = 0.4$).
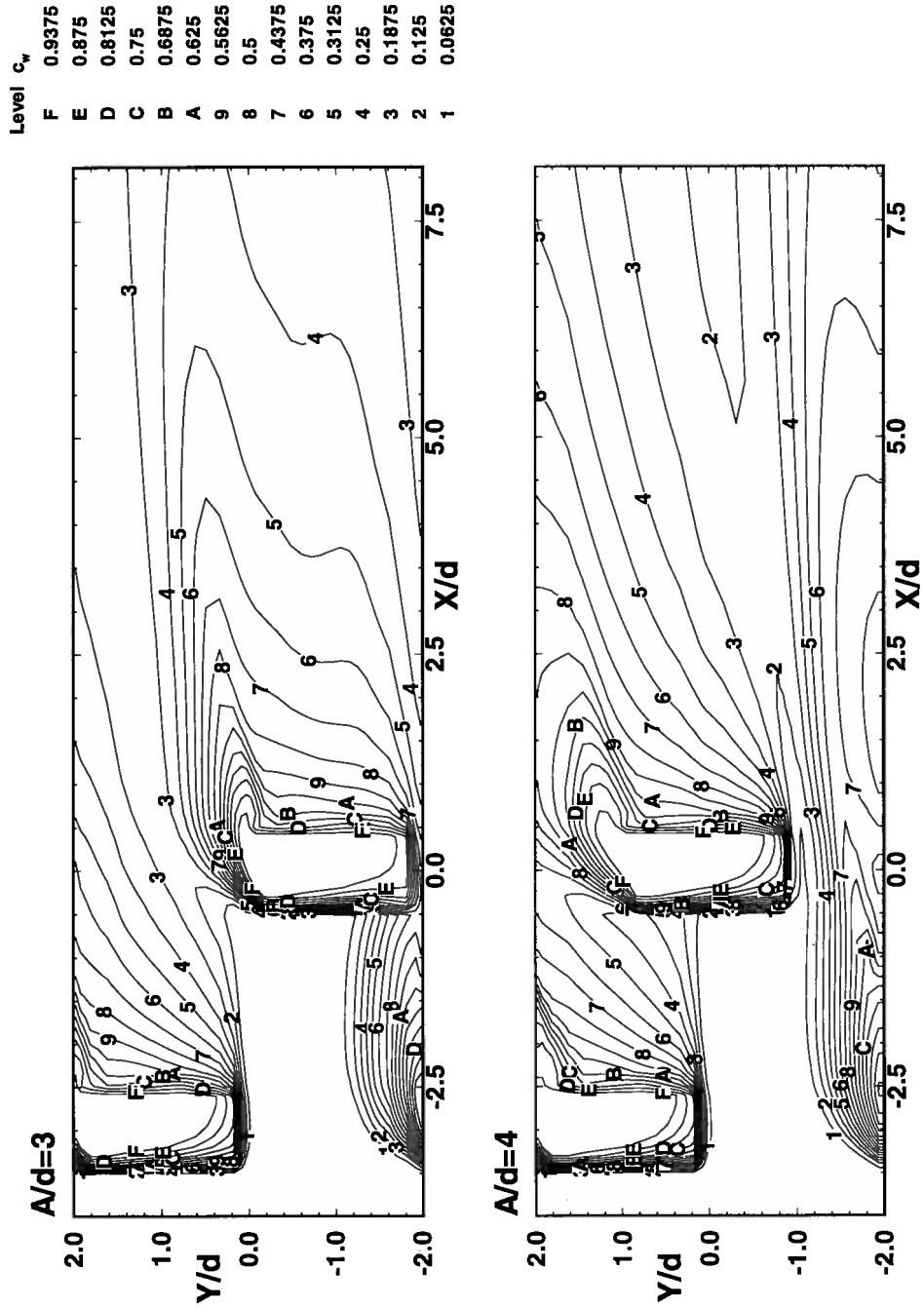
Figure C.6: Predicted surface film cooling effectiveness ($A/d = 2, 3$, $R_M = 0.4$).
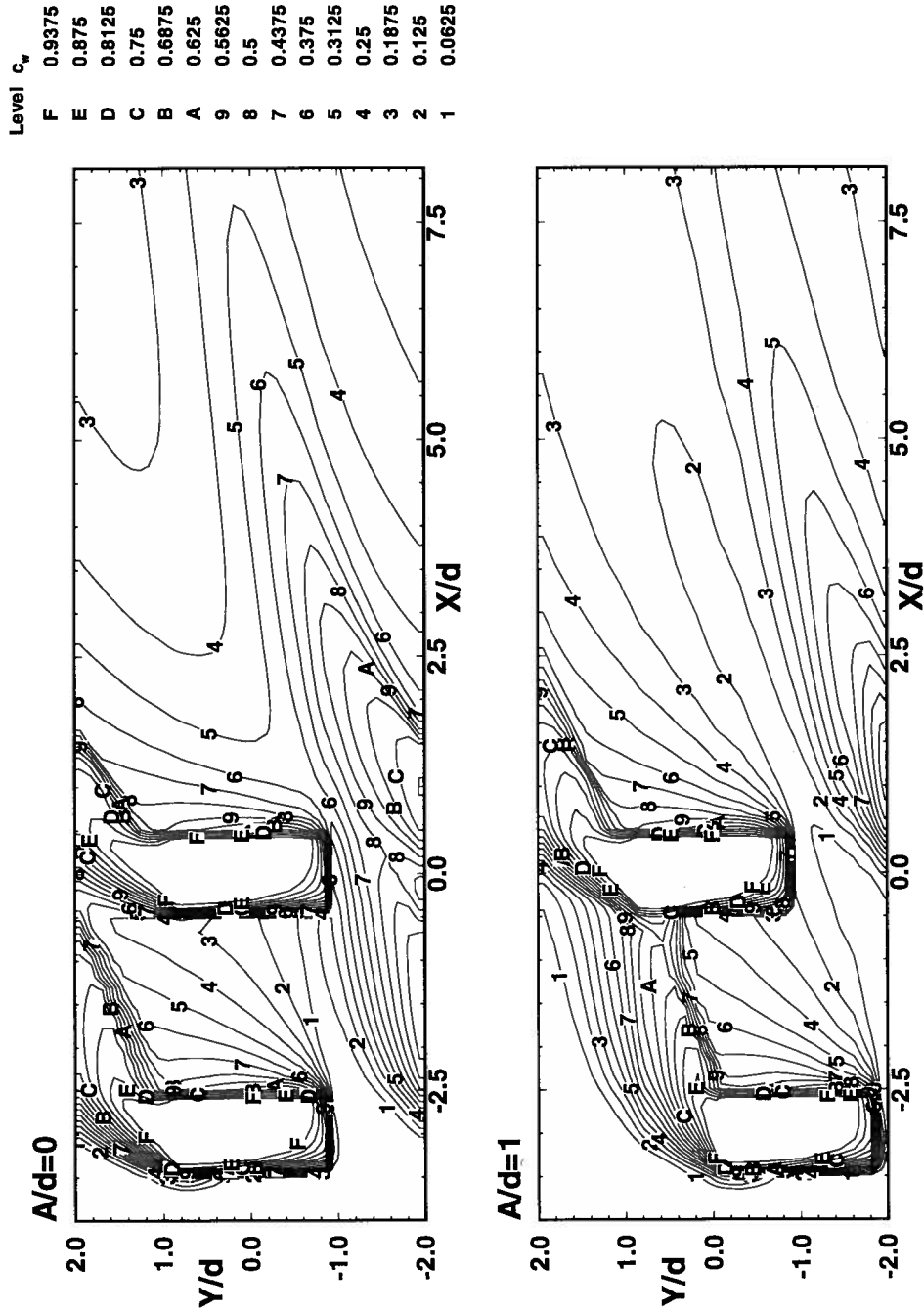
Figure C.7: Predicted surface film cooling effectiveness ($A/d = 0, 1$, $R_M = 0.8$).
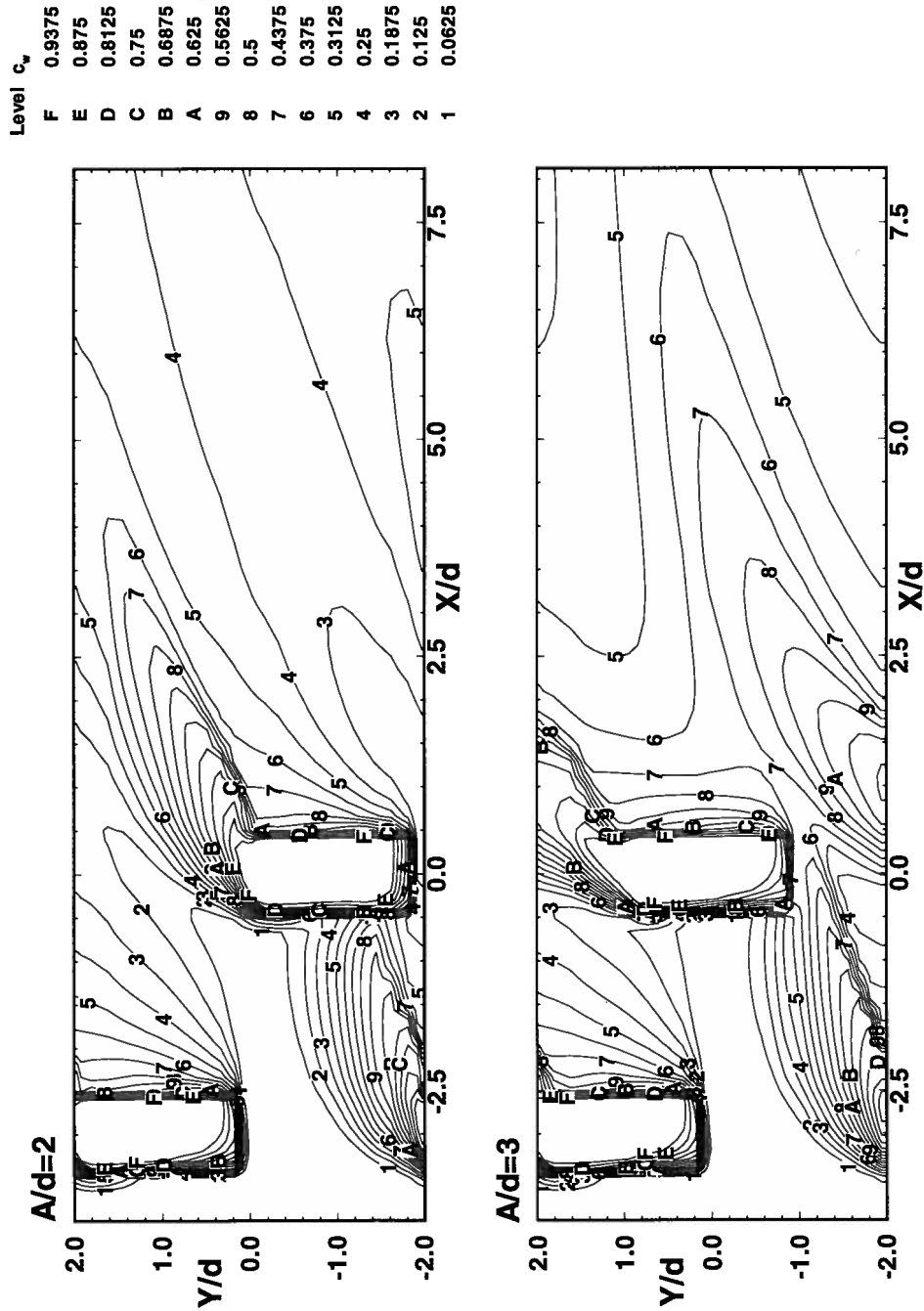
Figure C.8: Predicted surface film cooling effectiveness ($A/d = 2, 3$, $R_M = 0.8$).
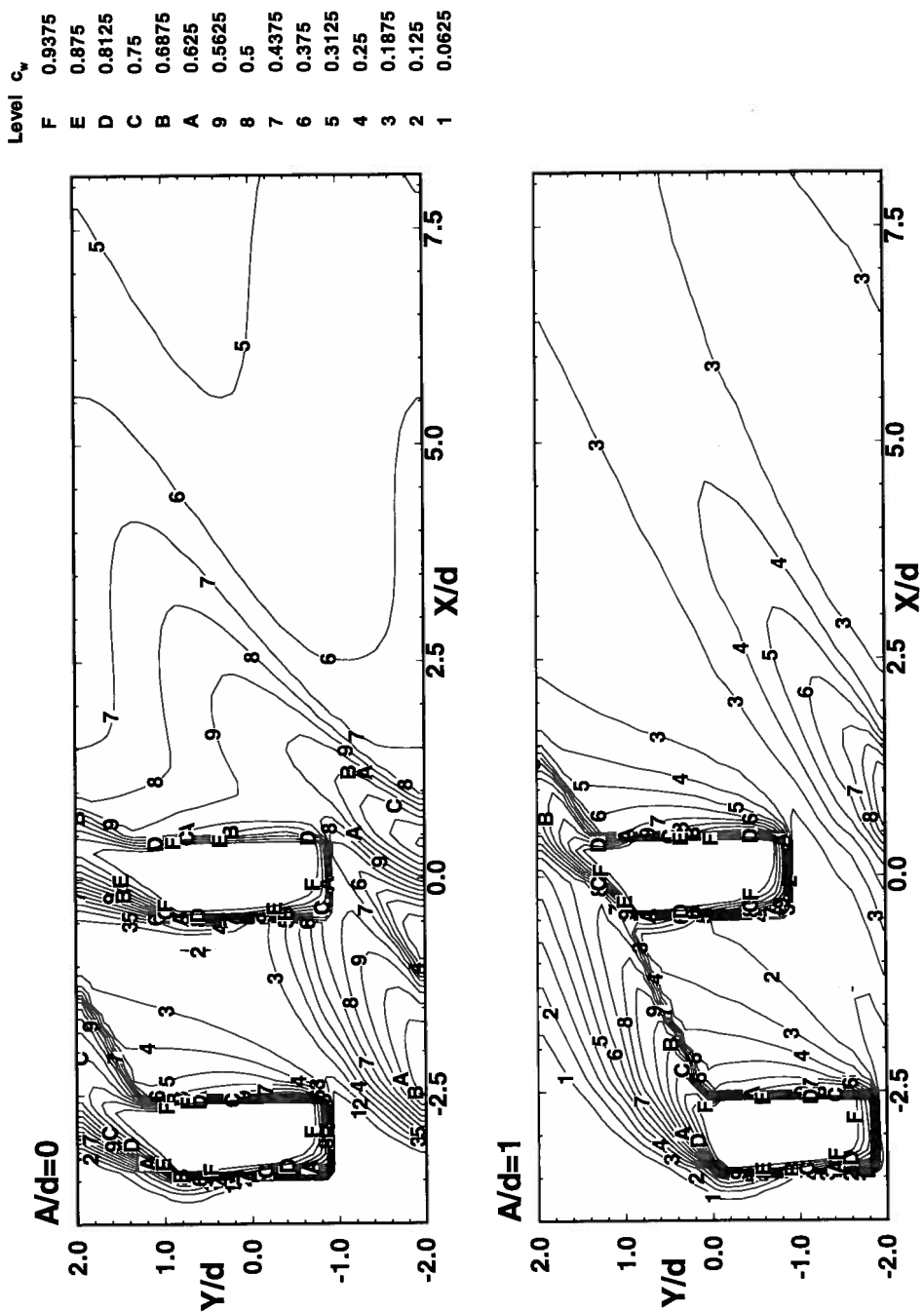
Figure C.9: Predicted surface film cooling effectiveness ($A/d = 0, 1$, $R_M = 1.2$).
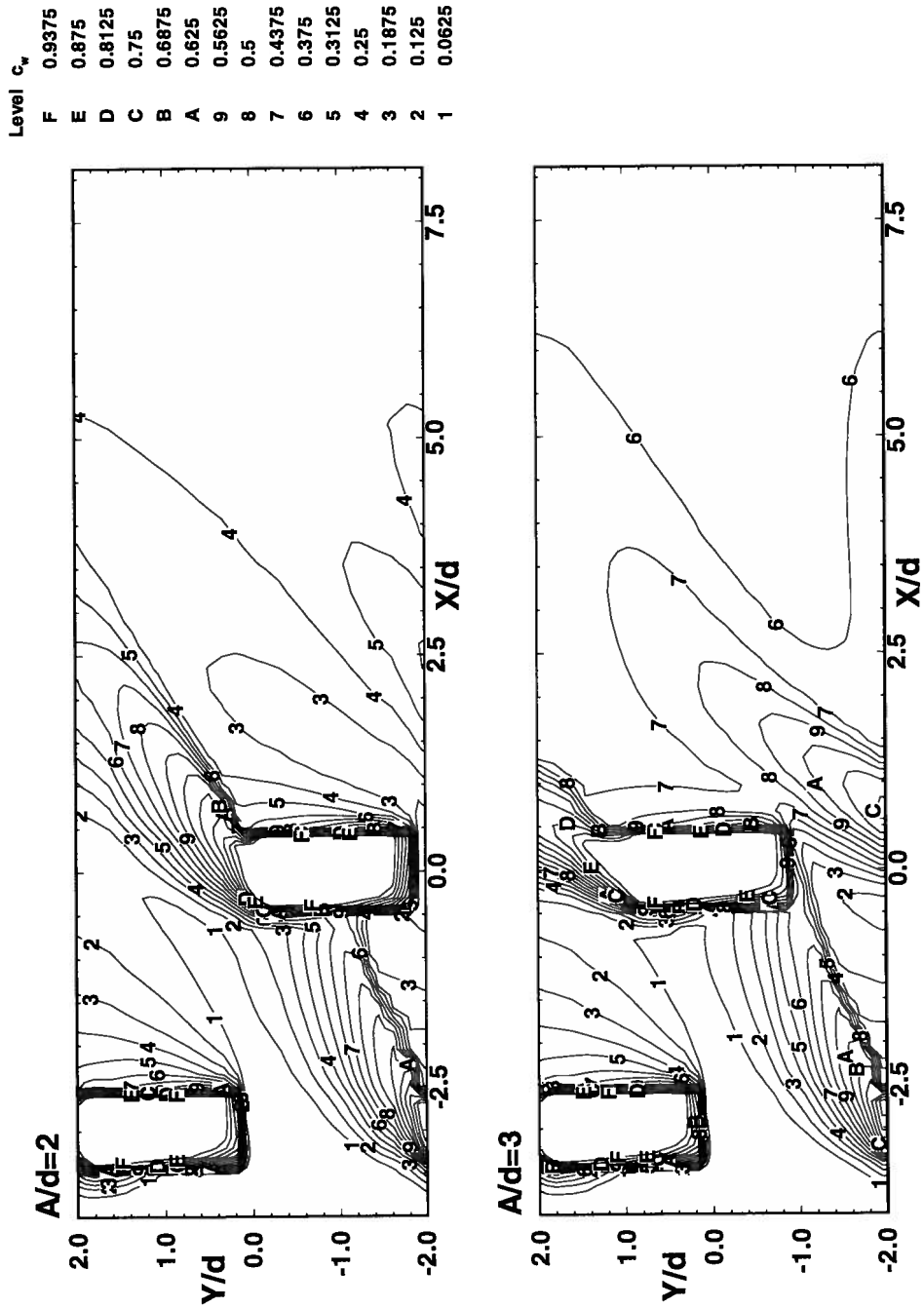
Figure C.10: Predicted surface film cooling effectiveness ($A/d = 2, 3$, $R_M = 1.2$).
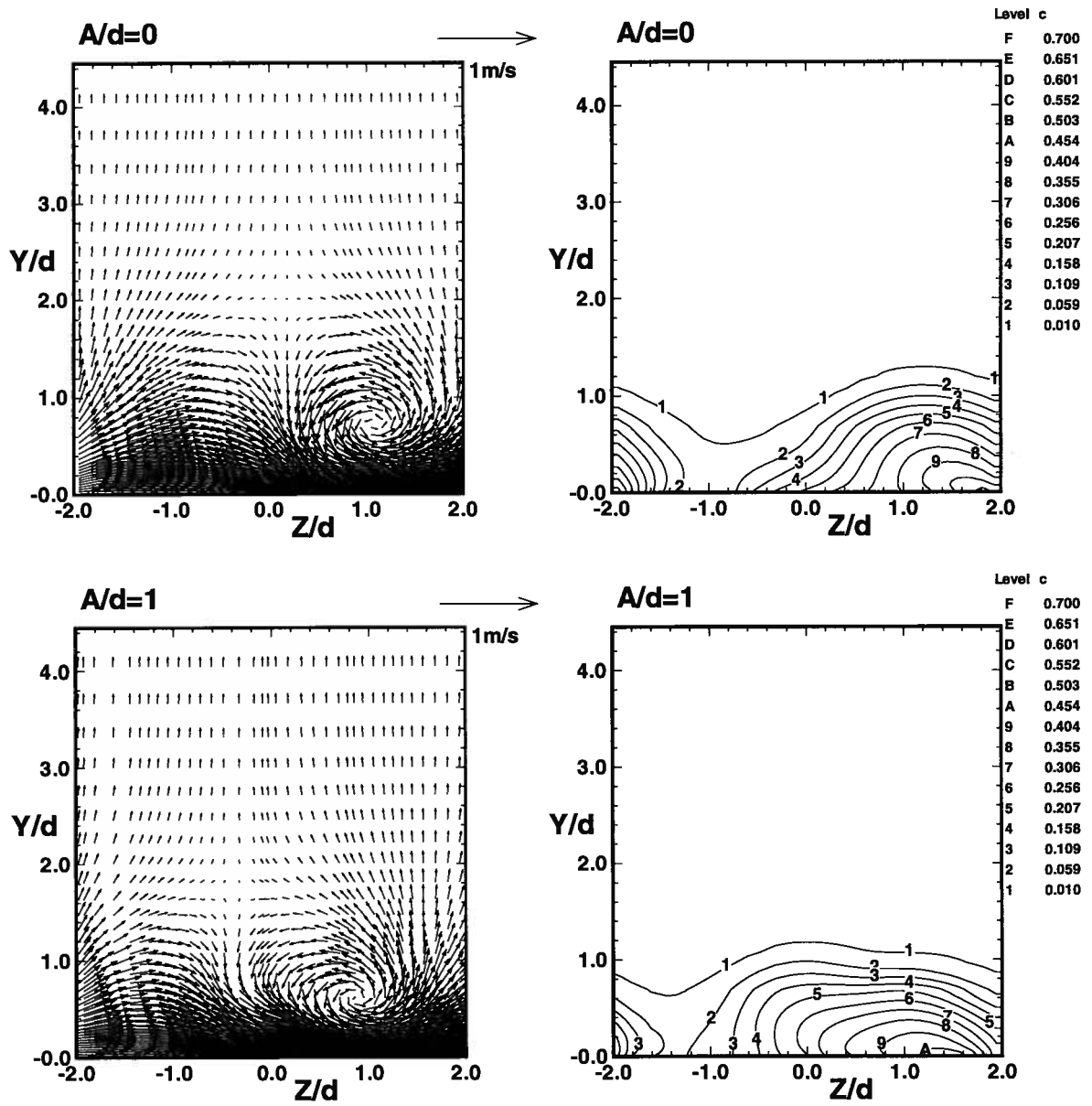
Figure C.11: Predicted vector field and concentration distribution at $X/d = 3$ ($A/d = 0, 1$, $R_M = 0.4$).
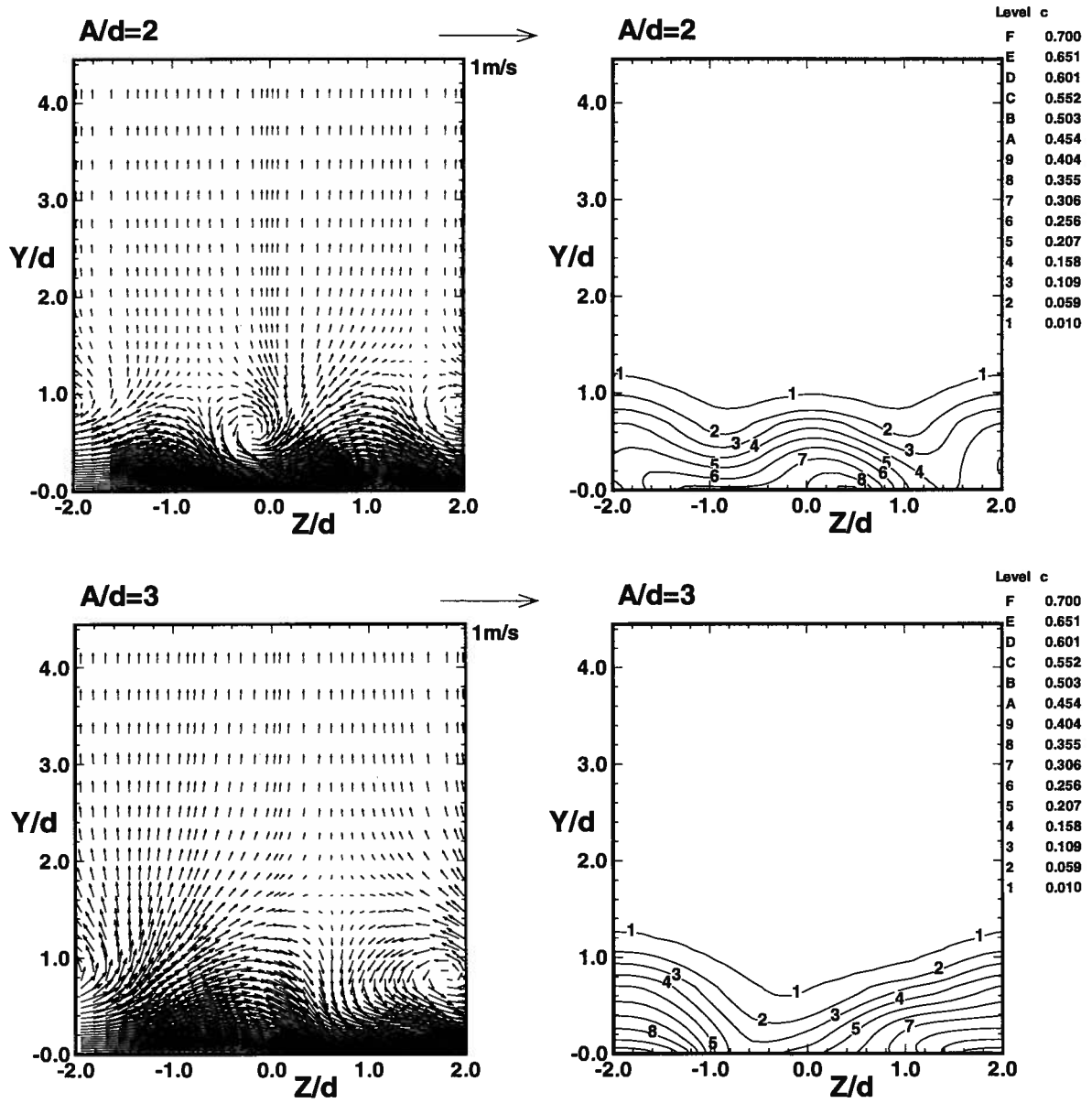
Figure C.12: Predicted vector field and concentration distribution at $X/d = 3$ $(A/d = 2, 3, R_M = 0.4)$.
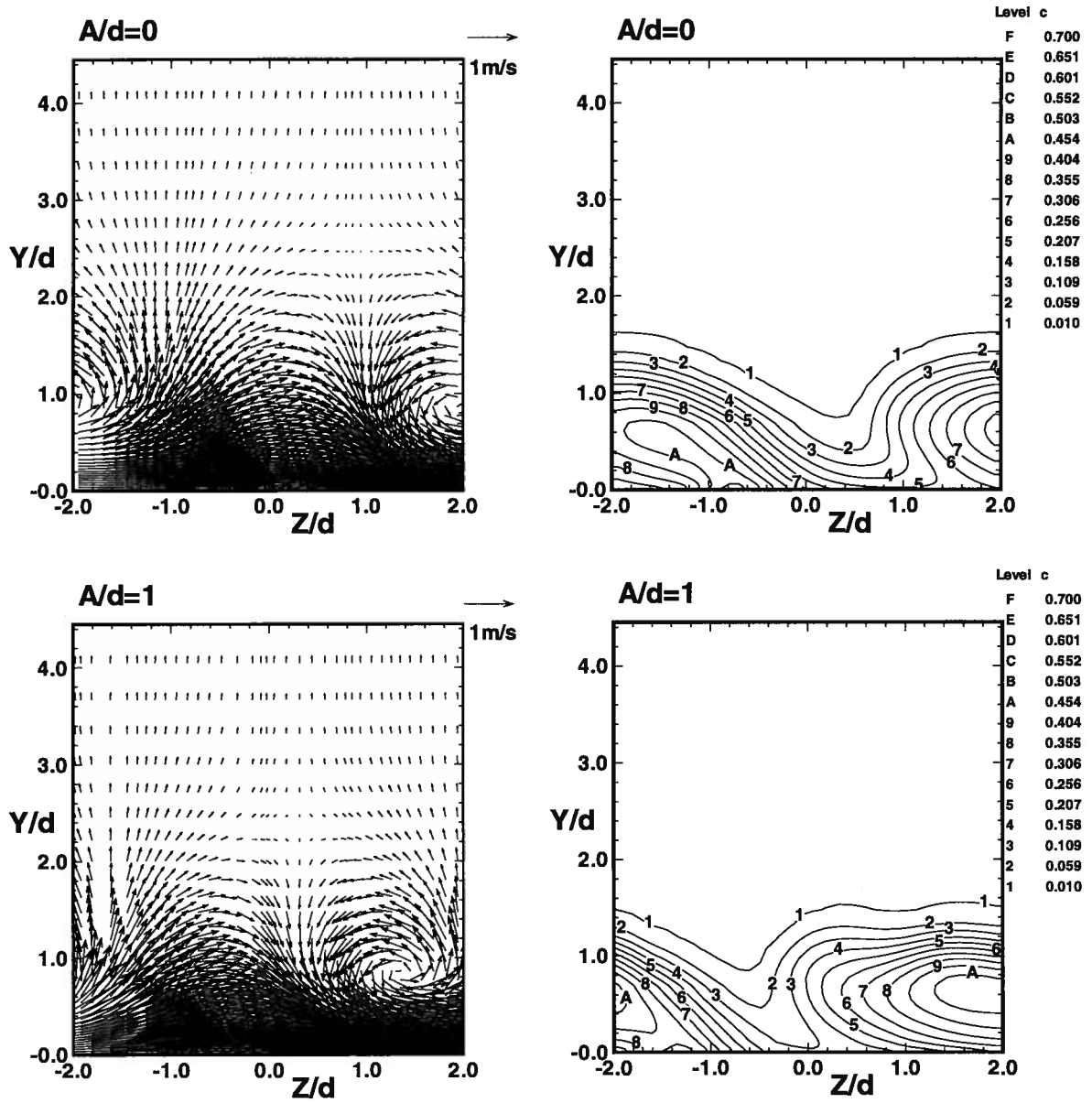
Figure C.13: Predicted vector field and concentration distribution at $X/d = 3$ ($A/d = 0, 1$, $R_M = 0.8$).
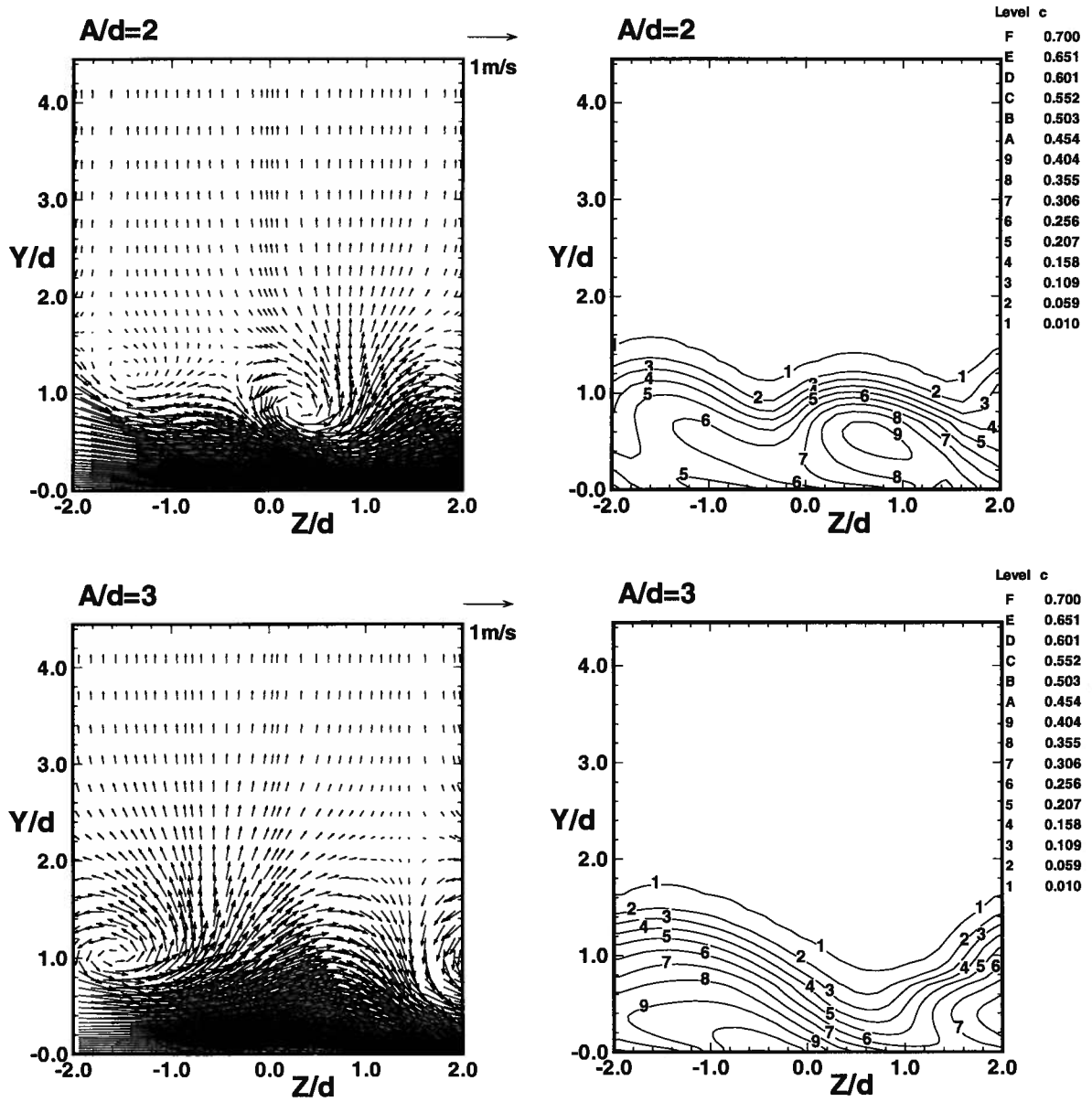
Figure C.14: Predicted vector field and concentration distribution at $X/d = 3$ ($A/d = 2, 3$, $R_M = 0.8$).
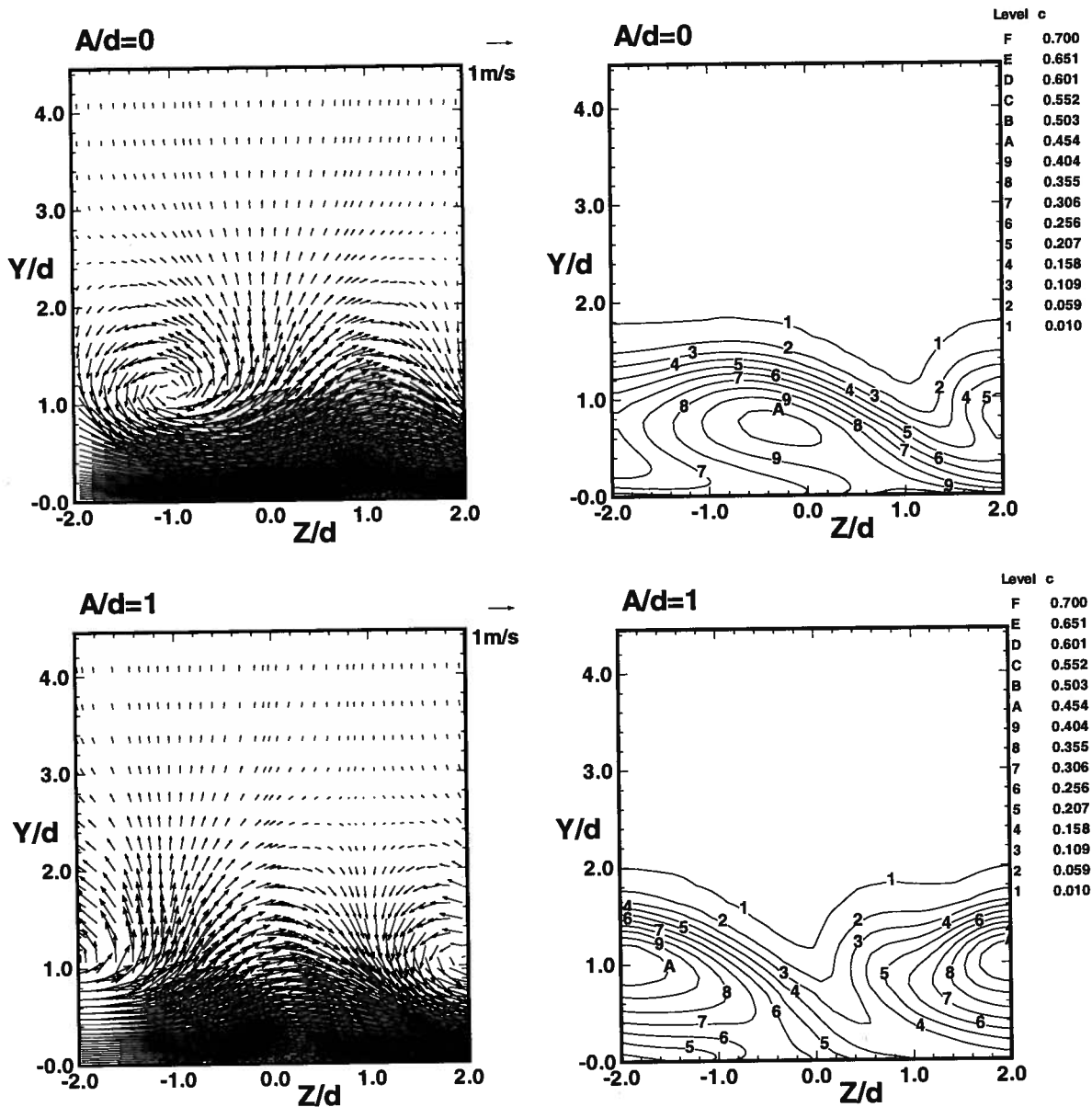
Figure C.15: Predicted vector field and concentration distribution at $X/d = 3$ ($A/d = 0, 1$, $R_M = 1.2$).
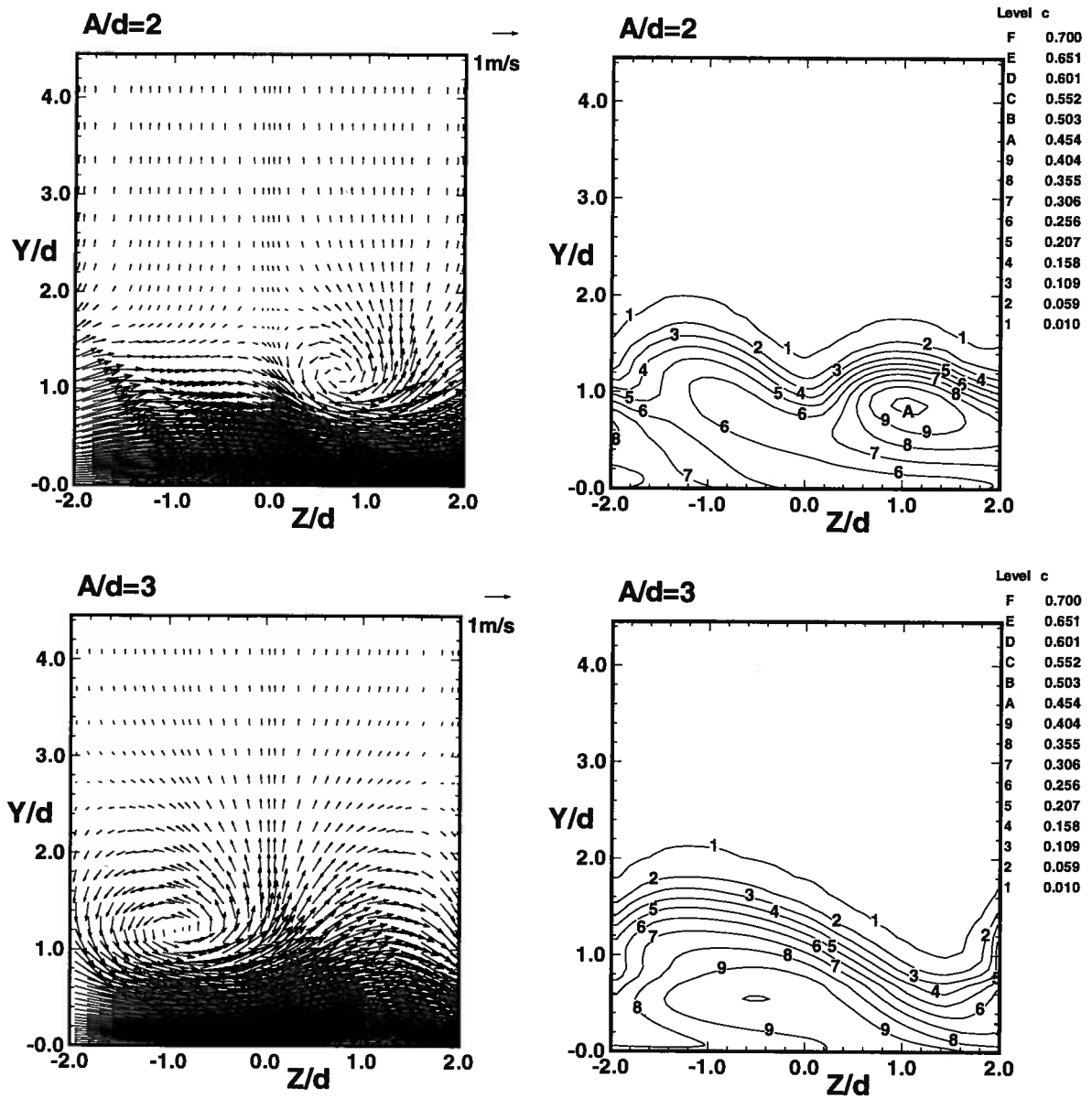
Figure C.16: Predicted vector field and concentration distribution at $X/d = 3$ ($A/d = 2,3$, $R_M = 1.2$).

C.   2-D Computations with the Algebraic Reynolds Stress Model

The algebraic Reynolds stress model of Launder et al. (1975) was investigated in the present 2-D computations. An attempt was made in the 2D-MGFD code to use the k-ε equations (Equations 4.11 and 4.13) together with the algebraic expression for the Reynolds stresses (Equation 4.14) to solve for $\overline{u_i'u_j'}$, k, and ε. During each smoothing cycle, each component of $\overline{u_i'u_j'}$ was calculated iteratively based on the mean flow field, k, and ε. However, no converged solution was obtained. This failure to converge is due to the fact that the algebraic equation of Equation 4.14 cannot be solved by the direct iterative method. Since the algebraic Reynolds stress model is derived empirically and all the stress components are strongly coupled through Equation 4.14, an adequate method to solve this system of equations needs to be devised.

D. 3-D Computations with the Multiple-Time Scale Model

The multiple-time scale model of Kim (1989) was explored within the present 3-D computations. The M-T-S model was implemented into the 3D-MGFD code but no converged solution was obtained even on a coarse grid. Based on the experience of 2-D computations as stated in Section 6.2, extra iterations for the M-T-S model equations are needed in order to obtain stable iterative convergence. However, in the 3D-MGFD code all the variables are solved simultaneously in a coupled nature. In order to stablize the turbulence equations, an attempt should be made to decouple the turbulence equations from the mean flow. Due to the limitation of time, further implementation of the 3D-MGFD code was not made.